Performance Improvement for Electrode Flooding with Novel Gas Diffusion Layer Less Polymer Electrolyte Membrane Fuel Cells

by

SHIRO TANAKA

A dissertation submission in partial fulfillment of the requirement for the degree of

Doctor of Philosophy in Engineering

Graduate School of Science and Engineering

Tokyo Metropolitan University

Supervised by

Professor TOSHIO SHUDO

TOKYO METROPOLITAN UNIVERSITY

2015

Author's Declaration

I hereby declare that I am the sole author of this thesis. This is a true copy of the thesis, including any required final revisions, as accepted by my examiners. I understand that my thesis may be made electronically available to the public.

Abstract

The gas diffusion layer (GDL)-less fuel cell that is composed of a corrugated-mesh shows less flooding performance even in the high current density region, because gases are supplied more uniformly to the catalyst layer in comparison with the conventional fuel cell utilizing GDL. On the other hand, its internal electrical resistance is higher than that of conventional fuel cell, because corrugate mesh and underneath microporous layer (MPL) makes less contact area with points-contact. This can increase the resistance at the interface between corrugated-mesh and MPL as well as MPL and catalyst layer (CL) greatly from the conventional fuel cell where GDL can make good contact with MPL. In this study the conductivities and contact resistances of each material are measured under various mechanical compression pressures, and coupled mechanical-electric-electrochemical simulation is developed to investigate the effect of these electrical resistance. As a result, it is found that our model can simulate well for the GDL-less fuel cell and the effect of the electric resistance in the GDL-less fuel cell has a big contribution on the polarization performance.

Acknowledgements

This thesis would not have been possible without the guidance and the help of several individuals who in one way or another contributed and extended their valuable assistance in the preparation and completion of this work. I extend my sincere gratitude to everyone who helped me throughout this process. In particular, I would like to thank my supervisor, Professor Toshio Shudo, for his expert guidance, constructive criticism, and extended efforts, all of which ensured the success of this project. I would like to thank Takaaki Arai and Satoshi Takaichi in EV system laboratory at Nissan Motor in Japan, and the rest of the team in Nissan as well as Hiroshi Tabata in Tokyo Institute of Technology and Shinsuke Ohyagi in KRI Inc. I would also like to extend my sincere gratitude to my family, whose support echoed across provinces.

Finally, I would like to thank all the staff in Chemical Engineering in University of Cape Town for their generous support, especially Heidi Conrad and Olaf Conrad spent lots of time for my stay in South Africa. Again, thank you all.

TABLE OF CONTENTS

Chapter 1 Introduction

Chapter 2 Literature Review

Chapter 3 Microcoil Fuel Cell without GDL

3.1 Preparation of Fuel Cell and Components

3.2 Characterization of Materials and Fuel Cell Performance

3.3 Results and Discussion

Chapter 4 Corrugated-mesh Fuel Cell without GDL

4.2 Preparation of Fuel Cell and Components

4.3 Characterization of Materials and Fuel Cell

4.4 Results and Discussion

Chapter 5 Modeling Study

5.2 Characterization of Materials

5.3 Measurement results and numerical model

5.4 Results and Discussion

Chapter 6 Summary and Future Work

LIST OF PUBLICATIONS

Publication in this thesis

1. **Significant performance improvement in terms of reduced cathode flooding in polymer electrolyte fuel cell using a stainless-steel microcoil gas flow field**

   Shiro Tanaka, Toshio Shudo

   Journal of Power Sources 248 (2014) 524–532.

2. **Corrugated mesh flow channel and novel microporous layers for reducing flooding and resistance in gas diffusion layer-less polymer electrolyte fuel cells**

   Shiro Tanaka, Toshio Shudo

   Journal of Power Sources 268 (2014) 183–193.

3. **Coupled electrical-mechanical-electrochemical simulation for performance of gas diffusion layer-less polymer electrolyte fuel cells**

   Shiro Tanaka, Toshio Shudo

   Journal of Power Sources 278 (2015) 382–395.

Relevant Publications NOT Included in the Thesis

4. **Production behavior of irradiation defects in lithium silicatesand silica under ion beam irradiation**

   K. Moritani, S. Tanaka, H Moriyama

   Journal of Nuclear Materials 281 (2000) 106–111.

5. **Thickness dependence of water permeation through proton exchange membranes**

   Makoto Adachia, Titichai Navessina, Zhong Xiea, Fei Hua Li, Shiro Tanaka, Steven Holdcroft

   Journal of Membrane Science 364 (2010) 183–193.

6. **Polymer elecrolyte membrane**

   Shiro Tanaka, Takashi Tarao, Toru Uda, Tomoo Inaba, Masaaki Kawabe, Takatosih Sato

   Nissan Motor Co.,Ltd. Japan Vilene Co.,Ltd. NOK CORPORATION

   JP Patent 5432033 (2013)

7. **Electrolyte membrane and membrane electrode assembly using the same**

   Shiro Tanaka, Takuya Hasegawa

   Nissan Motor Co.,Ltd.

   JP Patent 5369531 (2013).

8. **Microporous Layer and Gas Diffusion Layer**

   Shiro Tanaka, Norihiro Waki, Takuya Hasegawa

   Nissan Motor Co.,Ltd.

   JP Patent 5481820 (2014).

9. **Polymer electrolyte fuel cell with microcoils**

   Nissan Motor Co.,Ltd.

   Shiro Tanaka

   JP Patent 5504615 (2014).

10. **Polymer electrolyte fuel cell with Corrugated-meshs**

    Shiro Tanaka, Shigechika Miki

    Nissan Motor Co.,Ltd. Miki Seisakusho Co.,Ltd

    JP Patent 5500908 (2014).

11. **Electrolyte membrane and membrane electrode assembly using the same**

    Shiro Tanaka, Hiroshi Tabata, Shuguo Zhang

    Nissan Motor Co.,Ltd, KRI Ink.

    JP Patent, 5564755 (2014).

12. **FUEL CELL MEA WITH COMBINED METAL GAS DIFFUSION LAYER AND MICROPOROUS LAYER**

    Shiro Tanaka, Nabeel Hussain

    University of Cape Town

    United Kingdom Provisional Patent Application, No 1405659.2, (2014).

13. **A CLAMP ASSEMBLY FOR A FUEL CELL STACK AND A METHOD OF ASSEMBLING A FUEL CELL STACK**

    Shiro Tanala

    University of Cape Town

    United Kingdom Provisional Patent Application, No 1320838.4, (2014).

14. **FUEL CELL CATALYST LAYER AND COTALYST SUPPORT MATERIAL LAYER AND CATALYST SUPPORT MATERIAL**

    Shiro Tanala, Nabeel Hussain, Pieter Levecque, Collean Jackson, Cloe Legrand

    University of Cape Town

United Kingdom Provisional Patent Application, in Manuscript.

15. **ULTRASONIC WATER ATMIZER IN A POLYMER ELECTROLYTE FUEL CELL**

    Shiro Tanaka, Nabeel Hussain

    University of Cape Town

    United Kingdom Provisional Patent Application, in Manuscript.

16. **Catalysts and MEAs from South Africa: The world’s platinum nation moves up the value chain.**

    Olaf Conrad, Pieter Levecque, Shiro Tanaka, Sharon Blair

    4th European PEFC and H2 Forum 2013, 2–5 July 2013, Lucerne, Switzerland.

17. **Metal based gas diffusion layers to improve two phase flow in polymer electrolyte fuel cells.**

    Nabeel Hussain, Shiro Tanaka, Olaf Conrad

    The 20th World Hydrogen Energy Conference 2014, June 15–20, 2014, Gwangju Metropolitan City, Korea.

LIST OF FIGURES

Chapter 1

Chapter 2

Chapter 3

bipolar plate assembly.

Fig. 3-4. Schematic image of depicting the test setup for the thermal conductivity measurements.

Fig. 3-5. Images of (a) single fuel assembly and (b) fuel cell evaluation apparatus.

Fig. 3-6. Polarization curves for Design CNV (conventional fuel cell), Design MCC-1 (0.6 mm microcoil with a GDL), and Designs MCC-2 (0.2 mm microcoils without a GDL), and MCC-3 (0.2 mm microcoils without a GDL), obtained under RH_{anode} =100%, $RH_{cathode}$ = 100%, ambient pressure at the outlets, cell temperature = 70 °C, and hydrogen and air supplied in a stoichiometric ratio of 9.0 at 1.5 A cm^{-2}.

Fig. 3-7. High-frequency resistance (HFR) for Designs CNV, MCC-1–3.

Fig. 3-8. IR-corrected polarization curves for Designs CNV, MCC-1–3.

Fig. 3-9. Dependence of IR-corrected cell voltage on cathode stoichiometry α_{air} for for Designs CNV, MCC-1–3.

Fig. 3-10. Schematic of electrical conduction at the cathode in Designs; (a) CNV, (b), MCC-1, (c) MCC-2, and (d) MCC-3.

Fig. 3-11. Schematic images of the resistance through MPL in-plane direction.

Fig. 3-12. Contact area of microcoil|MPL represented with 3D CAD.

Fig. 3-13. Estimated average temperature increase for Designs CNV, MCC-2, and MCC-3. For the microcoil, thermal resistance data were used; for the GDL and MPL, thermal conductivity and thickness data were used to calculate the temperature increase.

Chapter 4

Chapter 5

(c) Design CRM-3c (corrugated-mesh fuel cell with SF-MPL), and (d) Design CRM-3d (corrugated-mesh fuel cell with SS-MPL).

Fig. 5-10. Electrical resistance analysis results under compression pressure of (a) Design CNV (conventional fuel cell), (b) Design CRM-3a (corrugated-mesh fuel cell with CB-MPL), (c) Design CRM-3c (corrugated-mesh fuel cell with SF-MPL), and (d) Design CRM-3d (corrugated-mesh fuel cell with SS-MPL).

Fig. 5-11. Experimental and simulated polarization curves (a) Design CNV (conventional fuel cell), (b) Design CRM-3a (corrugated-mesh fuel cell with CB-MPL), (c) Design CRM-3c (corrugated-mesh fuel cell with SF-MPL), and (d) Design CRM-3d (corrugated-mesh fuel cell with SS-MPL), obtained under RH_{anode} =100%, $RH_{cathode}$ = 100%, ambient pressure at the outlets, cell temperature = 70 °C, and hydrogen and air supplied in a stoichiometric ratio of 9.0 at 1.5 A cm^{-2}.

Fig. 5-12. Electron conduction pathway analysis and IR drop distribution for (a) Design CNV (conventional fuel cell), (b) Design CRM-3a (corrugated-mesh fuel cell with CB-MPL), (c) Design CRM-3c (corrugated-mesh fuel cell with SF-MPL), and (d) Design CRM-3d (corrugated-mesh fuel cell with SS-MPL).

LIST OF TABLES

NOMENCLATURE

B–V	Butler Volmer equation
BPP	bipolar plate
CB	carbon black
CCM	catalyst-coated membrane
CL	catalyst layer
DMFC	direct methanol fuel cell
EIS	electrical impedance spectroscopy
EPDM	Ethylene–propylene diene monomer rubber
FEM	finite-element model
FM	full morphology
GDL	gas-diffusion layer
GF	graphite flake
HFR	high-frequency resistance
IR	current I × resistance R (ohmic loss)
IV	current-voltage
MEA	membrane–electrode assembly
MPL	microporous layer
PEM	proton exchange membrane
PEM-FC	polymer electrolyte membrane fuel cell
PTFE	polytetrafluoroethylene

RH	relative humidity
SF	silver flake
SS	stainless steel

Symbles

F	Faraday constant, C mol^{-1}
R	universal gas constant, J mol^{-1} K^{-1}
R_{overall}	overall resistance, Ω cm^{2}
R_{C}	contact resistance, Ω cm^{2}
R_{M}	material resistance, Ω cm^{2}
T	temperature, K
V_{cell}	cell voltage, V
V_0	open circuit potential, V
h	thickness, m
i_0	exchange current density, A m^{-3}
j	current density, A m^{-3}

Greek

α	transfer coefficient, unit-less
σ	proton conductivity, S m^{-1}
η_{act}	activation overpotential, V
η_{ohm}	ohmic overpotential, V

Subscripts

a	anode

c	cathode
mem	membrane
solid	solid phase

Chapter 1. Introduction

1.1. Background

Polymer electrolyte membrane fuel cells (PEM-FC), which convert the chemical energy of hydrogen directly into electrical energy, are regarded as promising, alternative, and clean power sources for automotive, stationary, and portable applications [1–5]. The utilization of fuel cells for powering automotive requires a reduction in cost and size, as current automotive fuel cells are not profitable and are still too large, limiting the layout of the fuel cell system [6].

Generally, if the required power for a single cell can be produced with a smaller active area while keeping the voltage around 0.6 V [7], the multi-cell fuel cell stack can be made smaller and cheaper as shown in Fig. 1-1 and Fig. 1-2. Currently, most automotive fuel cells operate with a maximum current density of around 1.0–1.5 A cm^{-2}, which consequently increases the number of catalyst coated membrane (CCM) composed of polymer electrolyte membranes (PEM) and catalyst layers (CL) with precious metals, and gas diffusion layers (GDLs) as shown in Fig. 1-3. The expense of these materials means that larger active areas significantly increase the cost of fuel cell stack. In addition, a GDL thickness of 90-200 μm for each electrode increases the length of the stacking direction, and the total volume of the GDL occupies about half of the fuel cell stack. These considerations create limitations for conventional fuel cell structures with regard to cost and size.

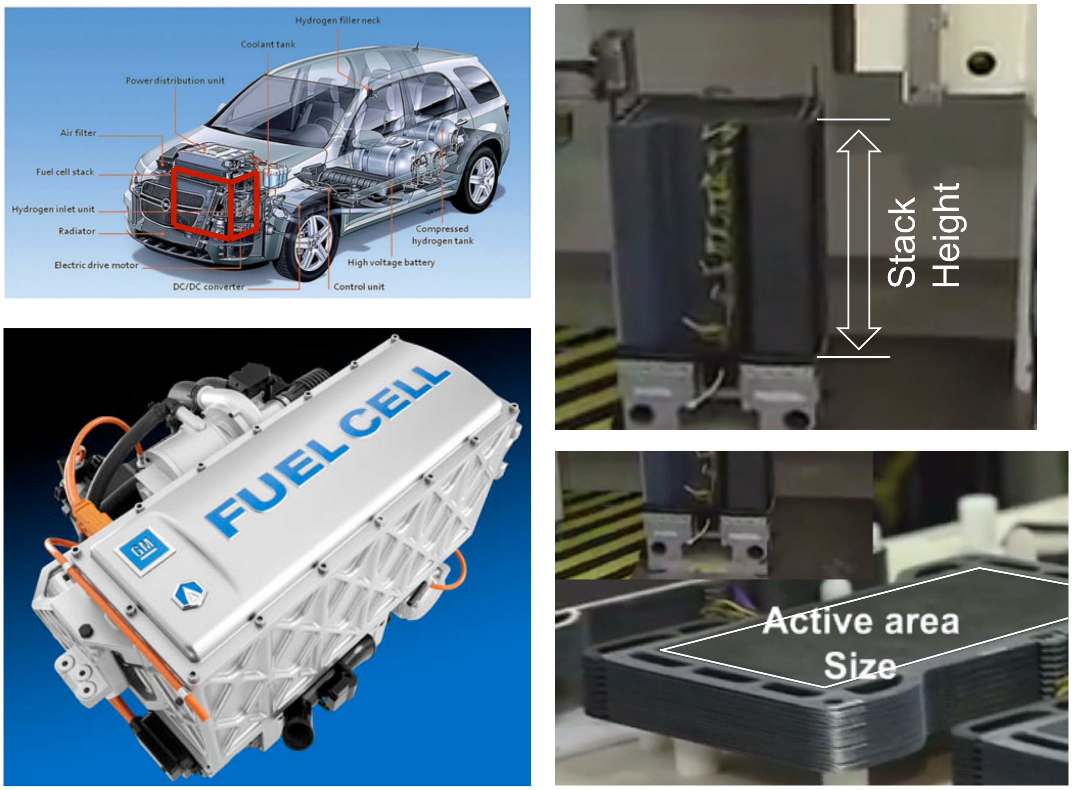

Fig. 1-1. Fuel cell stack layout in a vehicle, and fuel cell height and active area size [7].

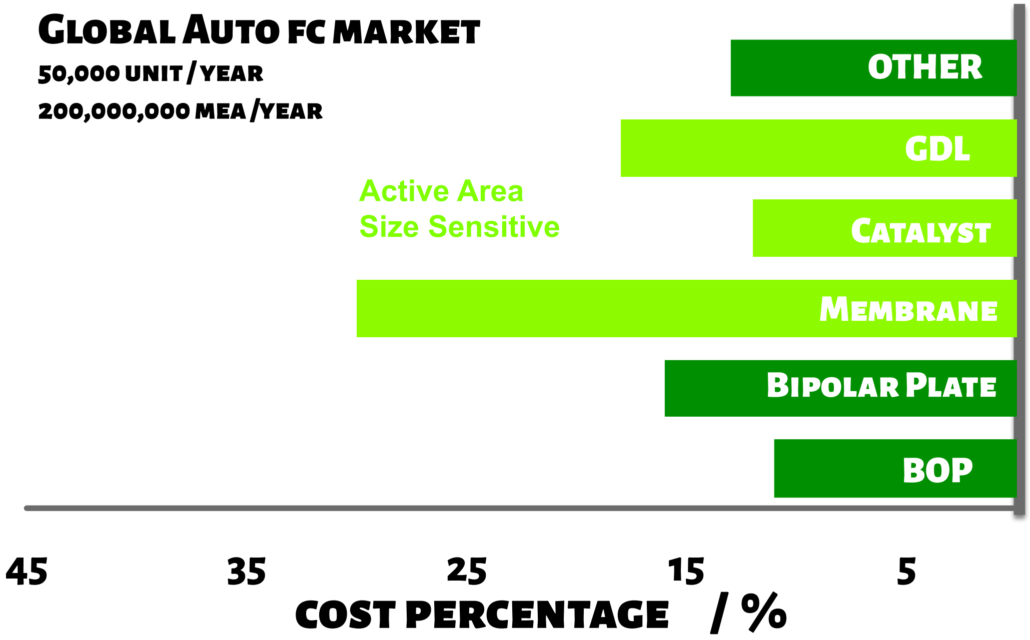

Fig.1-2. Cost structure of fuel cell stack with its components [9].

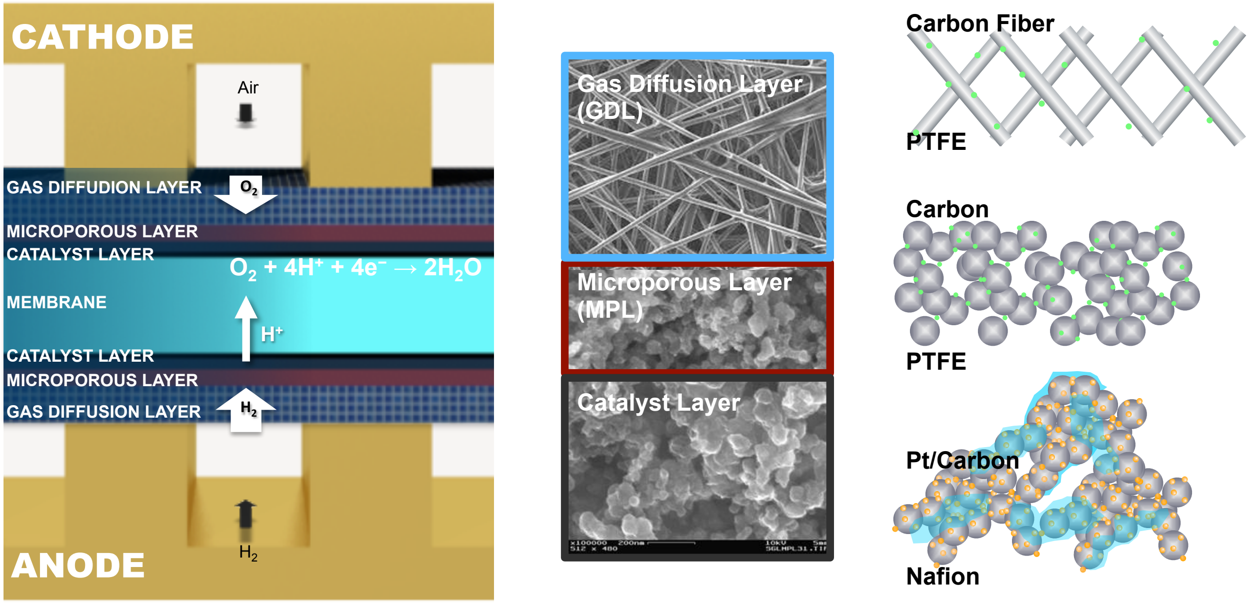

Fig. 1-3. Schematic image of fuel cell and its components.

Increasing the current density of conventional fuel cells causes a sudden decrease in performance, known as cathode flooding. When current density increases, more water is generated in the electrochemical reaction ($O_2 + 4H^+ + 4e^- \rightarrow 2H_2O$) at the cathode, and more water is transported from the anode to the cathode through the membrane via electro-osmotic drag [10–12]. The water at the cathode condenses and accumulates, blocking oxygen diffusion and causing a sudden decrease in the cell voltage.

Simultaneously increasing the current density causes the membrane to dry out at the anode. The membrane is dehydrated by electro-osmotic drag from the anode to the cathode [13], in addition to the increased temperature from the electrochemical reaction and the ohmic heat. The proton conductivity of the membrane heavily depends on its water content, meaning that dehydration of the membrane decreases proton conductivity and thus cell performance.

Furthermore, at the cathode side, air is provided from channel on bipolar-plate (BPP) and the air diffuses in the GDL to the surface of CL. Especially under-land region, the air diffuses in-plane direction of the GDL and that makes the distribution of oxygen concentration along with the in-plane direction of the GDL. That is known as air management issue inside the fuel cell [14]. On the other hand, the electron at the cathode side is provided from land on BPP and the electron transports in the GDL to the surface of CL. The voltage decreases by IR drop along with in-plane direction of GDL from under-land region to under-channel region. The both effects of the air management and electron conduction are well investigated and it has been founded that the air management issues are more influential on the fuel cell performance than the electron transport issues are.

Fig. 1-4 and Fig. 1-5 shows a schematic image of typical issues in PEM fuel cell, and typical polarization curve under these issues, respectively. There also are other issues; channel flooding [15], in which the water accumulates in the airflow channel, un-uniform gas distribution on each gas channel at the inlet, and un-uniform gas diffusion in the MPL and catalyst layer [15]. In this study, however, we focus mainly on the electrode flooding, and moreover on membrane dry-out, air management and electrical resistance. In the best knowledge, there is no successful fuel cell design to solve these issues meeting the requirement for the commercialization in the industry.

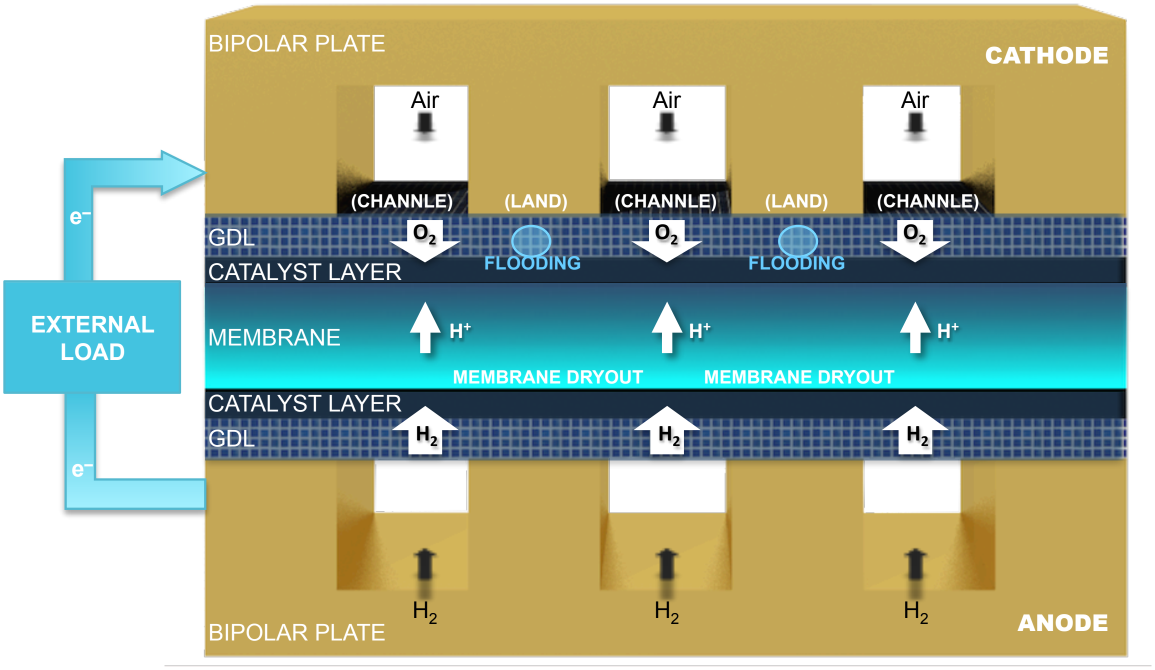

Fig. 1-4. Schematic image of a typical PEM fuel cell and its general issues.

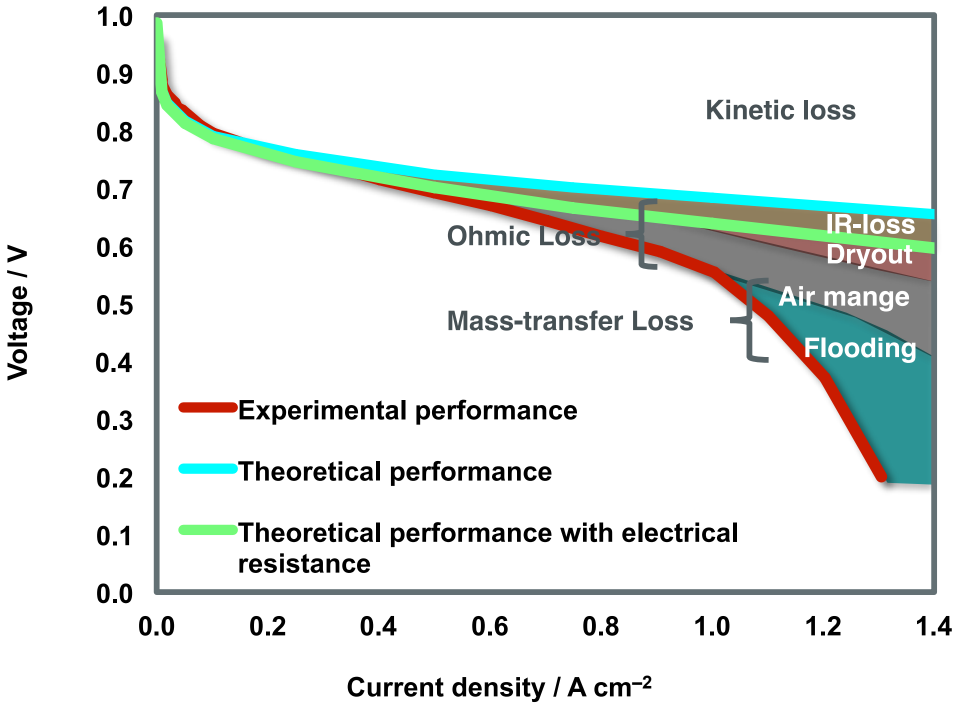

Fig. 1-5. Polarization curves for a typical PEM fuel cell under general issues.

1.2. Thesis Objectives

Solving these commercialization issues for automotive fuel cells requires a novel fuel cell structure that enables high current density operation without a GDL. In this thesis a unique GDL-less fuel cell design is described, which utilizes stainless steel microcoils and corrugated-mesh to generate the flow field namely microcoil fuel cell and corrugated-mesh fuel cell, respectively as shown in Fig. 2-1. These fuel cell designs are compared to the conventional fuel cell design with a GDL under various conditions. Furthermore, how these novel designs can reduce the performance degrease is discussed mainly for flooding, dry-out, air management, and electrical resistance experimentally. In addition, these new structures and materials are expected to perform differently compared with conventional structures and materials, and the electrical and thermal properties of several elements of the fuel cells are subsequently characterized. Finally, a three-dimensional numerical model is conducted with mechanical-electrical-electrochemical coupling for investigating especially the internal electrical resistance in the fuel cells, and the direction for further development is shown on their components in the GDL-less fuel cell.

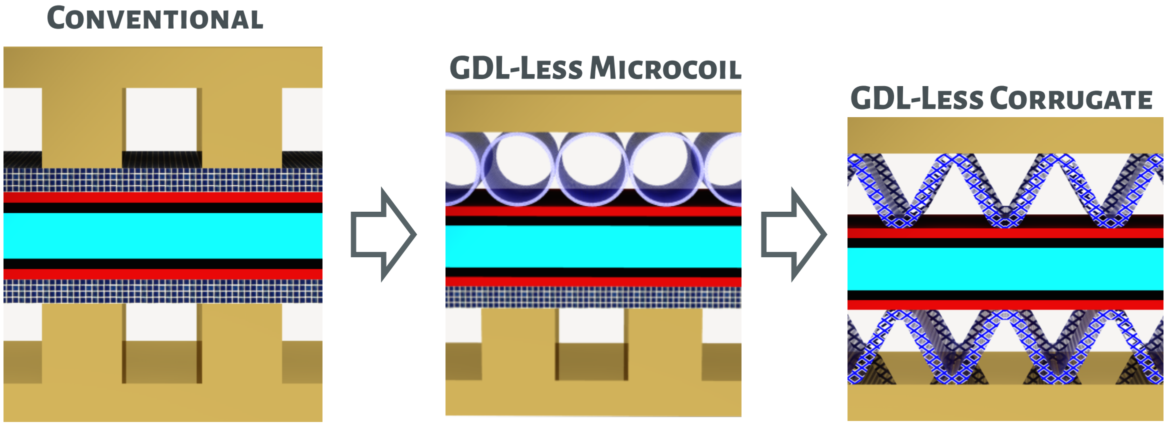

Fig. 2-1. New fuel cell structures in this thesis.

1.3 Scopes and Outline of Thesis

This work is organized as follows: in Chapter 1, introduction for fuel cell and its current issues, in Chapter 2, performance degreases in PEM fuel cell by flooding, dry-out, air management, and electrical resistance, in Chapter 3, proof of the concept of GDL-less fuel cell with microcoil, Chapter 4, proof of the concept of GDL-less fuel cell with corrugated-mesh and the effect of MPL conductivity in the GDL-less fuel cell, , in Chapter 5, 3-dimentional numerical modeling study for GDL-less fuel cell on mechanical-electrical-electrochemical coupling, in Chapter 6, study conclusion and future work recommendations.

Bibliography for Chapter 1

[1] P.L. Hentall, J.B. Lakeman, G.O. Mepsted, P.L. Adcock, J.M. Moore, J. Power Sources 80 (1999) 235–241.

[2] K. Jiao, B. Zhou, J. Power Sources 169 (2007) 296–314.

[3] C. Bao, M. Ouyang, B. Yi, Int. J. Hydrogen Energy 31 (2006) 1879–1896.

[4] T.V. Nguyen, ECS Trans. 3 (2006) 1171–1180.

[5] Committee on Assessment of Resource Needs for Fuel Cell and Hydrogen Technologies, National Research Council, Transitions to Alternative Transportation Technologies – A Focus on Hydrogen. The National Academies Press, Washington, D.C., 2008.

[6] C.C. Chan, Proc. IEEE 90 (2002) 247–275.

[7] U. Eberle, B. Müller, R. von Helmolt, Energy Environ. Sci., 5 (2012) 8780–8798.

[8] M.K. Dabe, Nature, 486 (2012), 43–51.

[9] D. Papageorgopoulos, 2013 Annual Merit Review and Peer Evaluation Meeting, US Department of Energy, 2013.

[10] N.Y. Steiner, P. Moçotéguy, D. Candusso, D. Hissel, A. Hernandez, A. Aslanides, J. Power Sources 183 (2008) 260–274.

[11] W. Dai, H. Wang, X.Z. Yuan, J.J. Martin, D. Yang, J. Qiao, J. Ma, Int. J. Hydrogen Energy 34 (2009) 9461–9478.

[12] H. Li, Y. Tang, Z. Wang, Z. Shi, S. Wu, D. Song, J. Zhang, K. Fatih, J. Zhang, H.

Wang, Z. Liu, R. Abouatallah, A. Mazza, J. Power Sources 178 (2008) 103–117.

[13] T.A. Zawodzinski Jr., C. Derouin, S. Radzinski, R.J. Sherman, V.T. Smith, T.E. Springer, S. Gottesfeld, J. Electrochem. Soc. 140 (1993) 1041–1047.

[14] Q. Yan, H. Toghiani, H. Causey, J. Power Sources 161 (2006) 492–502.

[15] H. Li, Y. Tang, Z. Wang, Z Shi, S. Wu, D. Song, J Zhang, K. Fatih, J. Zhang, H. Wang, Z. Liu, R. Abouatallah, A. Mazza, J. Power Sources 178 (2008) 103–117.

Chapter 2. Literature Review

2.1. Challenges to Overcome the Flooding in PEM Fuel Cell

There are a few reports on efforts to overcome membrane flooding/dry-out. T. Shudo et al. replaced the conventional land/ channel flow field structure with a porous stainless steel in direct methanol fuel cell (DMFC) operations [1]. Using electrochemical impedance spectroscopy (EIS), they found that their fuel cell with a porous flow field allowed for uniform distribution of the reactant gas onto the catalyst layer, thus enabling higher performance than that of conventional cells even at a high current density of 0.5 A cm^{-2}. D.G. Strickland et al. developed a unique flow field with in-situ polymerized wicks coated onto the cathode channel in a hydrogen fuel cell [2]. The performance of their cell design was flood-free even at 1.5 A cm^{-2}. They concluded that the cathode channel wick provided a hydraulic pathway from the reaction sites to the outside of the fuel cell that removed the product water and diffused oxygen to the catalyst layers. A. Turhan et al. explored the effect of changing the width ratio of the land and channel (L/C) on water accumulation using an in-situ neutron imaging technique [3]. They concluded that liquid water tended to accumulate under the lands rather than under the channels, and that accumulation depended strongly on the flow-field geometry. As L/C decreased, less liquid water accumulated in the cell, permitting higher cell performance with less flooding. While there are a few published studies on flow-field alterations for extending current densities, there is little in the literature suggesting novel structures or materials to overcome flooding and dry-out with smaller cells and lower pressure drop designs.

2.2. Air Management in PEM Fuel Cell

I. Taymaz et al. [4] developed a three-dimensional model with mechanical deformation effect on the porosity and contact resistance of GDL|bipolar plate (BPP), and they found the more compression pressure shows less fuel cell performance because of less the diffusivity in the GDL under the compression in spite of lower contact resistance.

They consider the balance of gas diffusion and electron transport in the in-plain direction of the GDL. At the cathode side air is provided from channel on BPP and the air diffuses in the GDL to the surface of CL. Especially under-land region, the air diffuses in-plane direction of the GDL and that makes oxygen concentration distributes along with the in-plane direction of the GDL. That is known as air management inside the fuel cell [14]. On the other hand, the electron at the cathode side is provided from land on BPP and the electron transports in the GDL to the surface of CL. The voltage decreases by IR drop along with in-plane direction of GDL from under-land region to under-channel region. Although the both effects of the air and electron are well investigated, however, all the their efforts are for only conventional fuel cell and they conclude the air management issues are more influential on the fuel cell performance than the electron transport issues are.

T. Berning et al. found that a higher stoichiometric flow ratio results in a more uniform distribution of the air in the GDL especially under the land area in conventional fuel cell comparing stoichiometry of 1.5 to 4.0 [5] and they found that the limiting current density at stoichiometry 4.0 is estimated as 1.5 A cm^{-2} when the oxygen concentration at the CL becomes zero without any liquid water management consideration. D. Natarajan et al. simulate airflow rate effect for liquid water removal from GDL, and the liquid water cannot be removed from GDL sufficiently even with infinite stoichiometry [6]. They found that the liquid water transfer in the GDL by capillary pressure is very slow and cannot catch up with liquid water removal from the surface of the GDL by airflow. These two study suggest that in the conventional fuel cell the stoichiometry should affect the distribution of oxygen concentration in the catalyst layer but only stoichiometry cannot resolve the air management issue because of the flow field structure and diffusion transport in the GDL as well as liquid water management. This can be a nature issue of the conventional fuel cell.

2.3. Internal Electrical Resistance in PEM Fuel Cell

There is little information published in the literature pertaining to electron resistance in GDL-less PEM-FC stacks. B.C. Seyfang et al. reported the performance of GDL-less stacks utilizing micro-patterned glassy carbon flow fields and a catalyst-coated membrane (CCM) [7]. They found that the GDL-less stack had a higher ohmic loss than the GDL-containing stack due to the reduction of electron travel pathways through the thin catalyst layer in the GDL-less case. They also evaluated the ohmic loss for several channel geometries to verify the electron path through the catalyst layer, obtaining a linear correlation between the channel width and HFR of the fuel cell. They used the catalyst layer as the electron conductor and collector; however, problems with high ohmic loss and low gas diffusion were experienced directly under the land of the bipolar plate, especially at the cathode.

2.4 Numerical Modeling for PEM Fuel Cell

H. Meng et al. [8] developed a three-dimensional, single-phase, isothermal numerical model of PEM-FC with electron transport in the CL, GDL, and BPP and they found that the current density distribution and cell performance are determined with both of the oxygen concentration distribution by the diffusion through GDL and voltage distribution by the electron conduction through GDL. In addition they also found that at lower current density operation the electron transport is more dominant, and at higher current density operation the gas diffusion is more dominant. T. Zhou et al. [9] developed a similar model to investigate the effect of anisotropic conductivity in the GDL, and they concluded that the effect of GDL electrical resistance is negligible in the realistic values of GDL conductivity because gas transports in the GDL and CL are dominant. W. Sun et al. [10] did similar investigation incorporating with a two-dimensional model verifying channel-land geometric ratio, and they found that narrow land can supply the gases more sufficiently and uniformly but can increase the electrical resistance for longer electron pathway in the GDL. I. Taymaz et al. [4] developed a three-dimensional model with mechanical deformation effect on the porosity and contact resistance of GDL|bipolar plate (BPP), and they found the more compression pressure shows less fuel cell performance because of less the diffusivity in the GDL under the compression in spite of lower contact resistance.

They consider the balance of gas diffusion and electron transport in the in-plain direction of the GDL. At the cathode side air is provided from channel on BPP and the air diffuses in the GDL to the surface of CL. Especially under-land region, the air diffuses in-plane direction of the GDL and that makes oxygen concentration distributes along with the in-plane direction of the GDL. That is known as air management inside the fuel cell [11]. On the other hand, the electron at the cathode side is provided from land on BPP and the electron transports in the GDL to the surface of CL. The voltage decreases by IR drop along with in-plane direction of GDL from under-land region to under-channel region. Although the both effects of the air and electron are well investigated, however, all the their efforts are for only conventional fuel cell and they conclude the air management issues are more influential on the fuel cell performance than the electron transport issues are. On the other hand, in the GDL-less fuel cell, air seems to be provided more uniformly and the electron transport seems to be poor through MPL, which has less thickness and less conductivity than that of GDL.

Bibliography for Chapter 2

[1] T. Shudo, K. Suzuki, Int. J. Hydrogen Energy 33 (2008) 2850–2856.

[2] D.G. Strickland, J.G. Santiago, J. Power Sources 195 (2010) 1667–1675.

[3] A. Turhan, K. Heller, J.S. Brenizer, M.M. Mench, J. Power Sources 180 (2008) 773–783.

[4] I. Taymaz, M. Benli, Energy 35 (2010) 2134–2140.

[5] T. Berning, N. Djilali, J. Power Sources 124 (2003) 440–452.

[6] D. Natarajan, T. Van Nguyen. J. Power Sources 115 (2003) 66–80.

[7] B.C. Seyfang, Simplification and Investigation of Polymer Electrolyte Fuel Cells using Micro-Patterned Glassy Carbon Flow Fields, dissertation No. 18508, ETH Zürich, 2009.

[8] H. Meng, C.Y. Wang, J. Electrochem. Soc. 151 (2004) A358–A367.

[9] T. Zhou, H. Liu, J. Power Sources 161 (2006) 444–453.

[10] W. Sun, B.A. Peppley, K. Karan, J. Power Sources 144 (2005) 42–53.

[11] Q. Yan, H. Toghiani, H. Causey, J. Power Sources 161 (2006) 492–502.

Chapter 3. Microcoil Fuel Cell without GDL

3.1. Preparation of Fuel Cell and Components

3.1.1. Conventional Fuel Cell

The bipolar plates for our fuel cell had 5 cm2 active areas (1 cm x 5 cm) made of graphite (Mechanical Carbon Industry, Kanagawa, Japan). The end-plates for these bipolar plates were made with stainless steel, with eight holes for fastening the fuel cell with a compression pressure of 1 MPa. The end-plates had sheet heaters on the outside of both the anode and cathode to control the cell temperature. A stainless steel current-collector with 1-µm-thick gold plaiting was inserted between the bipolar plate and the end-plate on both sides. 0.6 µm-thick Ethylene propylene diene monomer rubber (EPDM) gaskets (NOK Corp, Tokyo, Japan) were used to surround the active area and seal the reactant gases. Bolt torques of 0.3 N•m were used to achieve the compression pressure of 1.0 MPa for the fuel cell assembly.

25-µm-thick Nafion (NRE211, du Pont de Nemours, Delaware, USA) was chosen as a polymer electrolyte membrane (PEM), and carbon supported platinum (Pt/C, 50 wt% Pt, TEC10E50E, Tanaka K.K., Tokyo, Japan) was selected as a catalyst. The catalyst-coated membrane (CCM) was prepared as follows: Pt/C powder was mixed with a Nafion dispersion (DE2020 du Pont de Nemours, Delaware, USA) using a zirconia bead mill for 8 h on a rotation table. The diameter of the beads was 1 mm, and the speed of rotation of the table was 400 rpm. The solid contents of the catalyst were prepared using a 1:1 mixture of carbon support : Nafion-ionomer. The catalyst was coated on both sides of the membrane with a spray coater (Mic Lab, Kanagawa, Japan) several times until the coating thickness was about 30 μm. The platinum loadings were 0.4 mg cm^{-2} for both the anode and the cathode. The coated membrane was dried at 80 ºC for 60 min and annealed at 130 ºC for 10 min to obtain the CCM.

Microporous layers (MPLs) were used in the anode and cathode catalyst layers to control the water management of the fuel cell [1]. MPL was prepared as follows: powdered carbon black (CB; Denka Black, Denki Kagaku Kogyo K.K., Tokyo, Japan), polytetrafluoroethylene (PTFE) aqueous dispersions (D-1, Daikin Industries Ltd., Osaka, Japan), nonionic surfactant (Triton X-100, SigmaeAldrich), and DI water were mixed with 1 mm zirconia beads in a bead mill for 3 h at 400 rpm using 5:1:20:20 CB:PTFE:surfactant:water. This coating was cast onto an expanded PTFE porous sheet (30 μm thick, Poreflon Membrane, Sumitomo Electric Industries Ltd., Osaka, Japan) and dried at 350 ºC for 60 min to obtain CB-MPLs with 40 μm and 60 μm thick.

The CCM was hot-pressed with MPLs on both sides for the anode and cathode at 130 ºC and 3 MPa g for 10 min, using 200 μm-thick Teflon backing sheets on both sides to avoid MPL attachment to the plates of the hand-press.

The flow field utilized the grooved graphite plate with a cathode land 50 mm long and 1 mm wide, and cathode channels 50 mm long, 1 mm wide, and 1 mm deep. The GDL and CB-MPL were laid between the flow fields.

3.1.2. Microcoil Fuel Cell

The cathode was chosen for these experiments because the cathode reaction has been found to be the limiting step in PEM-FCs, in contrast to the fast kinetics of the anode reaction as demonstrated by T.E. Springer et al. in their EIS study [2]. Four designs of cathode flow fields were investigated in this study utilizing a microcoil as shown in Fig. 3-1 and Fig. 3-2, Design MCC-1; utilized a 0.6 mm outer diameter as a flow field, a GDL (280 mm thick, 5 wt% PTFE, TGP-H-090, Toray, Tokyo, Japan) and a CB-MPL on the cathode side, where the microcoils were tightly arranged parallel to the cathode air flow on pool-shaped graphite bipolar plates, CB-MPL was laid on catalyst layer, and GDL was laid between microcoils and CB-MPL. Design MCC-2; utilized a 0.6 mm outer diameter microcoil flow fields and CB-MPL, where the microcoils were tightly arranged in the bipolar plate and laid directly on the CB-MPL, Design MCC-3; utilized a 0.2 mm outer diameter microcoil with similar configuration for Design MCC-2. All the microcoils were purchased from Micro Spring K.K. (Nagano, Japan) made of 50-µm stainless steel fiber with 0.1-µm-thick gold plating. The pitch of the coil was 90 µm, and the width of the opening was 40 µm; this configuration prevented the fibers from getting entangled with one other and facilitated the tight arrangement of the microcoils as shown in Fig. 3-3. The coil diameter of 0.6 mm and 0.2 mm were chosen for this study, because they utilize same fiber diameter of 50 µm in the supplier's product line. In addition these diameters are thought to be reasonable for their smaller height than conventional flow channel for the reduction of fuel cell stack volume, as descried in Chapter 1.

A conventional flow field was utilized for the anode in all the designs in order to focus on the effects on the cathode. The anode land was 50 mm long and 1 mm wide, and the anode channels were 50 mm long, 1 mm wide, and 1 mm deep. The GDL was laid between the anode bipolar plate and the MPL. Fig. 3-1 and Fig. 3-2 shows a schematic of the flow fields evaluated, and Table 3-1 shows the configuration of the corresponding fuel cells.

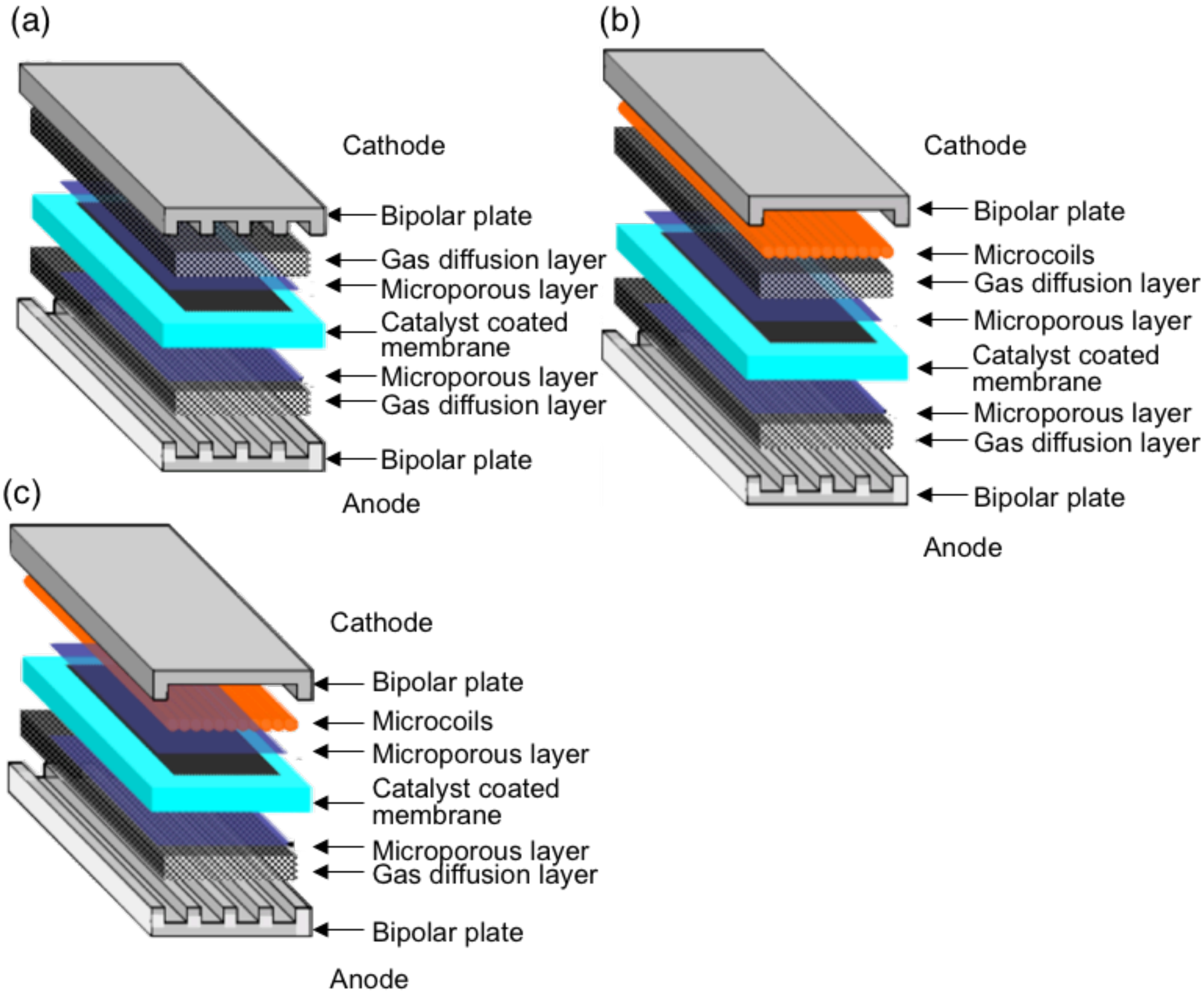

Fig. 3-1. Schematic image of (a) Design CNV (conventional fuel cell), (b) Design MCC-1 (0.6 mm microcoil with a GDL), and (c) Designs MCC-2 and MCC-3 (0.2 mm or 0.6 mm microcoils without a GDL). In all the designs, the anode was a conventional flow field.

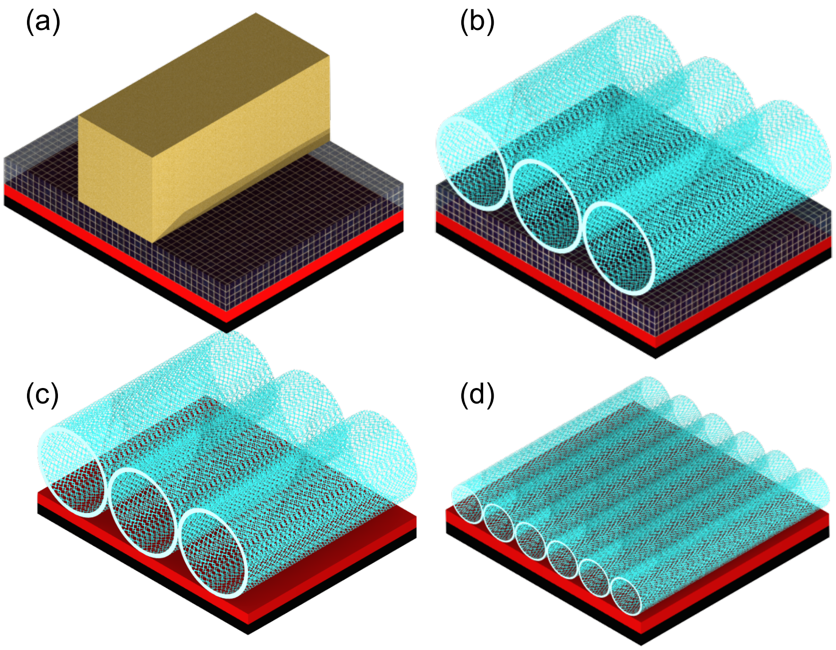

Fig. 3-2. Detailed image of (a) Design CNV (conventional fuel cell), (b) Design MCC-1 (0.6 mm microcoil with a GDL), and (c) Design MCC-2 (0.6 mm microcoils without a GDL), and (d) Design MCC-3 (0.2 mm microcoils without a GDL).

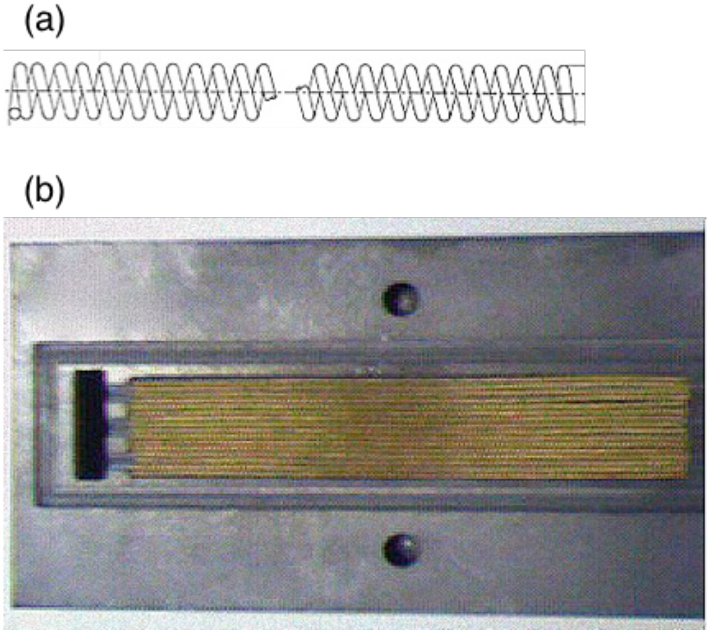

Fig. 3-3. Schematic image and actual picture of (a) microcoil and (b) microcoils and bipolar plate assembly.

Table 3-1. MEA and flow field configuration of conventional and microcoil fuel cells.

	Flow Field		GDL		MPL	
	Anode	Cathode	Anode	Cathode	Anode	Cathode
Design CNV	Conventional	Conventional	TGP-H-090	TGP-H-090	40 µm	40 µm
Design MCC-1	Conventional	0.6 mm Microcoil	TGP-H-090	TGP-H-090	40 µm	40 µm
Design MCC-2	Conventional	0.6 mm Microcoil	TGP-H-090	None	40 µm	40 µm
Design MCC-3	Conventional	0.2 mm Microcoil	TGP-H-090	None	40 µm	40 µm

3.2. Characterization of Materials and Fuel Cell Performance

3.2.1. Experimental Test Set-up for Fuel Cell Performance

The single cell was mounted on a fuel-cell test stand (Chino Co., Tokyo, Japan) equipped with mass flow controllers, an electronic loading device (Kikusui Electronics Co., Yokohama, Japan) for controlling the electric current, an AC milliohm tester (Model 3566, Tsuruga Electric Co., Osaka, Japan) with a constant HFR of 1 kHz, and a computer for equipment monitoring and data collection as shown in Fig. 3-4.

Gas flows for the anode and cathode were held constant to measure the polarization curves; 0.47 L min^{-1} of pure hydrogen was supplied to the anode (stoichiometry ratio α_{H2}: 9.0 at 1.5 A cm^{-2}), and 1.1 L min^{-1} of air was supplied to the cathode (stoichiometry ratio α_{air}: 9.0 at 1.5 A cm^{-2}). The reactants were supplied with a counter flow as well. All reaction gases were humidified to 100% relative humidity (RH) with temperature-controlled water bubbling tanks. The fuel-cell temperature was maintained at 80 ºC with a heater, and thermocouples were inserted into the cathode bipolar plate. As for the orientation of those fuel cells, the membrane-electrode assemblies (MEAs) were located vertically and the flow channels were set horizontally; consequently, gravity did not assist in the removal of liquid water from the channel.

For stoichiometry-dependent measurements, the gas flow to the anode was maintained at 0.21 L min^{-1} and the cathode gas stoichiometry was varied from 30.0 to 1.05 at 1.0 A cm^{-2} with 100% humidified air at 80 ºC generated using the water bubbling tanks.

All power-generation processes were conducted under atmospheric conditions. All fuel-cell evaluations were conducted after 10 h of aging at a current density of 1.0 A cm^{-2}, temperature of 80 ºC, anode feed gas flow of 0.5 L min^{-1} with 100% humidified hydrogen, and cathode feed gas flow of 0.5 L min^{-1} with 100% humidified air.

The small-area cell and high stoichiometry employed for the polarization curves was to obtain uniform distributions of the reactants, as the high stoichiometry conditions can help extrude accumulated water in the channel and reduce channel flooding such that the voltage loss caused by flow non-uniformity and oxygen depletion in the channel can be minimized. N.S. Siefert et al. investigated the voltage loss and voltage fluctuations for parallel straight flow channels having different stoichiometry and different aspect ratios of the same active area, where the water accumulates mainly in the flow channel, causing channel flooding [3]. They obtained a relatively low current density of 0.4 A cm^{-2}, which is well within the linear ohmic region of the polarization curve and is far from the non-linear mass transport-limited electrode region, where channel flooding is not present. Finally, they generalized the effects of channel plurality and stoichiometry on the normalized voltage loss as 32 $N \bullet A_c/A/\zeta$ and the standard deviation of voltage fluctuations as 34 $N \bullet A_c/A/\zeta^2$, where A_c is the cross-sectional area of each channel, A is the active area, N is the number of channels, ζ is the stoichiometry and $N \bullet A_c/A$ is the ratio of the total channel crosssectional area to the active area. These equations were applied to the present conventional system with a stoichiometry of 9.0 for the flow channel dimensions and MEA materials described here, which are quite similar to Siefert's system. The present system exhibited a voltage loss of 3.6% and voltage fluctuation of 0.42%; thus, the conventional design described can minimize channel flooding.

Even at such a high stoichiometry, the electrode can be flooded as reported by Yamada et al. from their results of experimental and simulation studies [4]. They showed that electrode flooding starts at a current density of 0.5 A cm^{-2}, and that voltage drops significantly around 1.2 A cm^{-2}. Their simulations also showed that liquid-water saturation in the GDL reaches a value greater than 0.8, especially the region under the flow-field land.

The present work focuses on electrode flooding; thus, a high air flow rate of 1.1 L min^{-1} and equivalent stoichiometry of 9.0 at 1.5 A cm^{-2} was used for the cathode to minimize the channel flooding effects on voltage loss. A stoichiometry of 9.0 for a conventional parallel flow channel is generally sufficient to avoid substantial effects attributed to channel flooding. However, for the microcoil flow channel, the effects of channel flooding and electrode flooding were not separated because of differences in the wettability of the carbon flow field and gold-plated stainless-steel microcoil, the air average velocity of each flow field, and the electrode interface and gas flow in the conventional flow field with the GDL and in the microcoil with the MPL. Thus, the equations described above could not be applied in this regard to estimate the effects of channel flooding owing to their limitations in describing geometry and materials. Nonetheless, the same operation condition was used for the microcoil flow field as for the conventional channel to compare these polarization curves to assess its advantages and disadvantages.

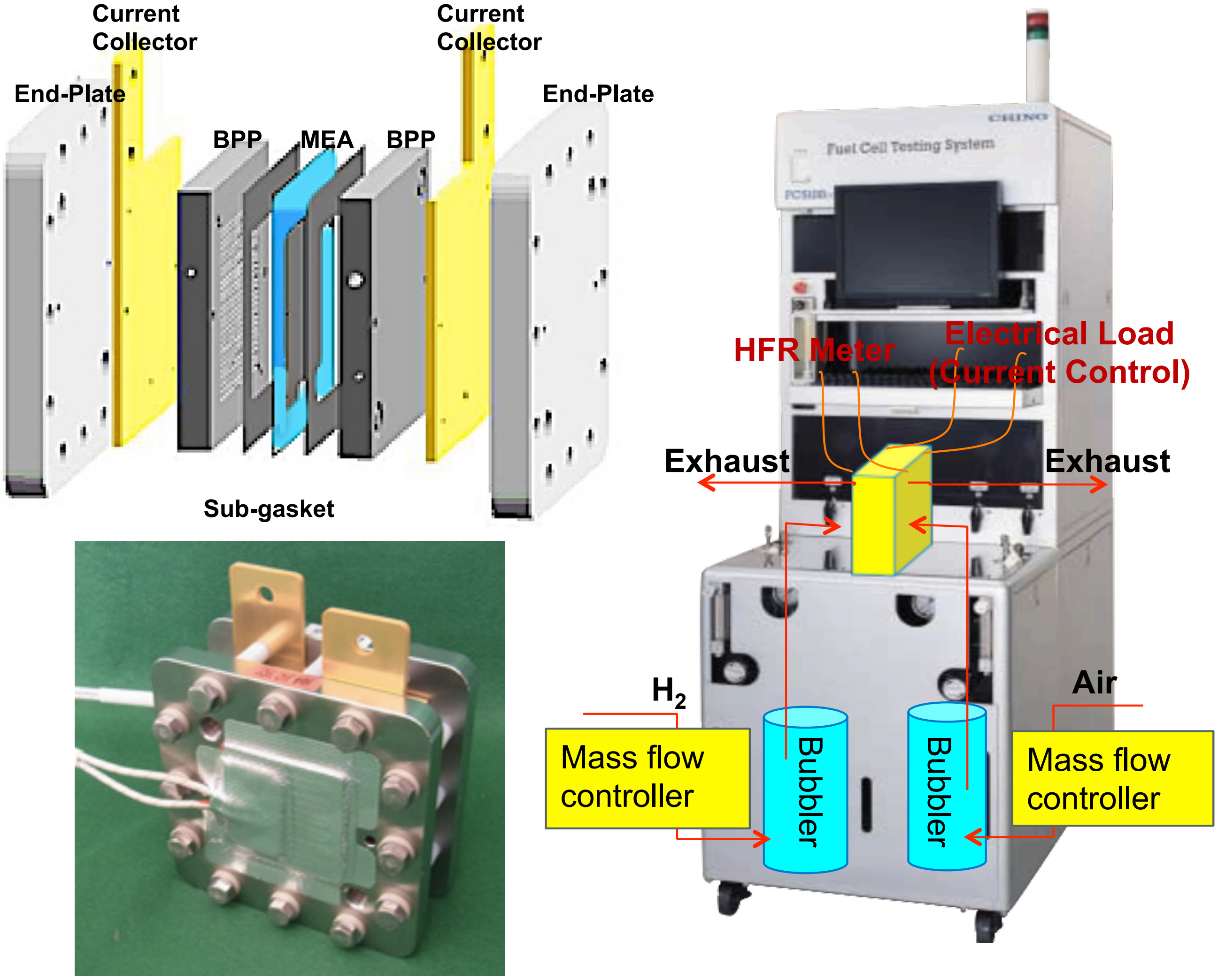

Fig. 3-4. Images of (a) single fuel assembly and (b) fuel cell evaluation apparatus.

3.2.2. Measurement of Electrical Conductivities in Microcoil Fuel Cell

For the microcoil fuel cells, the electron-conducting pathway from the cathode catalyst to the bipolar plate was thought to be different from conventional fuel cells and thus was expected to lead to different performances because of the different conductivity of materials. To characterize this, the electronic resistivity of the GDL and MPL were measured in the in-plane and through-plane directions.

The measurement of the in-plane resistivity was conducted at 25 C following ASTM standard C611, using four-point detectors in a direct current. 0.5 cm 4.0 cm sample strips of the MPL and GDL were used. Resistances obtained with a resistance meter (1750 LCR Dig-Bridge with Kelvin clip leads, Quad Tech Inc., Maynard, USA) were converted to resistivity using the sample geometries.

The measurement of the through-plane resistivity was conducted at 25 C in accordance with the method described in Ref. [5]. A 20 mm round sample was placed on a load cell (ElectroPuls^{TM} E1000, Instron, Massachusetts, USA) between two gold-plated pedestals, and the sample was subjected to a compression pressure of 1 MPa. The same resistance meter as above was used to obtain the resistance of the sample. After the compression stress stabilized (30-60 min), the resistance was measured and converted to resistivity using the sample geometry.

3.2.3. Thermal Conductivities in Microcoil Fuel Cell

The microcoil fuel cell were thought to have thermal resistances different from the conventional fuel cells, causing different degrees of temperature increases at a high current density, which could affect membrane dry-out. To characterize this, the thermal resistance and resistivity of the GDL and the microcoil were measured. Fig. 3-5 shows a schematic outlining the apparatus used for characterizing the thermal resistance of the GDL and microcoil. In this configuration, similar to that used by G. Karimi et al. [6] and G. Unsworth [7], four copper plates were used as material with known thermal conductivity (401 W m^{-1} K^{-1}), and the temperatures at the top and bottom of the copper plates were kept constant with water cooling condensers. A ceramic heater (MS-5, Sakaguchi EH VOC Corp., Tokyo, Japan) was placed between the upper and lower pairs of copper plates. The samples were placed in the middle of each pair of copper plates. Thermocouples were inserted in all the plates 1 mm from the samples. The compression pressure was precisely controlled and measured with a load cell (Kyowa, Tokyo, Japan); the uniformity of the pressure distribution on the surfaces of the plates was verified using Prescale film (for 0.5–2.5 MPa, Fujifilm Corporation, Tokyo, Japan) which indicated pressure intensity and distribution via color. The heater was controlled and monitored with an ampere meter to generate constant heat flux.

After 3 h, a steady state heat flux from the heater was equally transferred to the upper and lower pairs of copper plates, validated using the thermocouples in the copper plates without samples inserted. It was found that the copper plates located at equal distances from the heater were nearly the same temperature at compression pressures greater than 0.3 MPa. Above this compression pressure, the contact thermal resistance between the heater/ copper plate and copper plate/copper plate boundaries were the same, as was the heat flux for the upper and lower pairs of plates. Therefore, all evaluations were conducted with a compression pressure of 1.0 MPa.

Square samples (25 mm × 25 mm) with unknown thermal conductivities were placed in the middle of each pair of plates (upper and lower). The heat flux for each sample was half of the total heat generated (50 W) from the heater. The temperatures of the bottom and top surfaces of the samples were calculated using the heat flux from the heater, the temperature of the copper plates, and the distance between the two thermocouples. The through-plane thermal resistance across the samples was determined via Fourier's law using the sample surface temperatures [8]. This measurement included the thermal resistance generated by the samples as well as the thermal contact resistance between the sample and the copper plates. By performing the experiment with samples of two different thicknesses, the intrinsic thermal conductivity and thermal contact resistance were determined.

Two different thicknesses of commercially-available GDL were chosen to validate this measurement, that is TGP-H-60 (190 μm thick, Toray, Tokyo, Japan) and TGP-H-90 (280 μm thick, Toray) and the thermal conductivity values were compared with product data released by Toray, as well as an evaluation for the 0.2 and 0.6 mm microcoils used in our fuel cells.

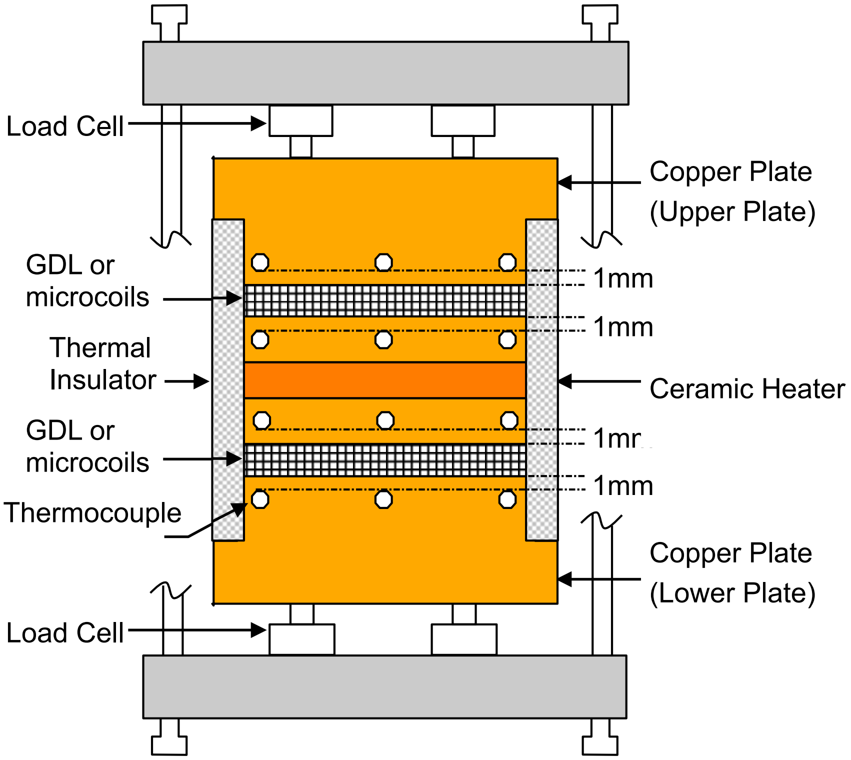

Fig. 3-5. Schematic image of depicting the test setup for the thermal conductivity measurements.

3.3. Results and Discussion

3.3.1. Polarization Curve

Fig. 3-6 shows the polarization curves for Design CNV (conventional Fuel Cell), Design MCC-1 (0.6 mm microcoil with GDL), Design MCC-2 (0.6 mm microcoil), and Design MCC-3 (0.2 mm microcoil). Fig. 3-7 shows the 1 kHz HFR, and Fig. 3-8 shows IR-corrected polarization curves for all four designs. IR correction is performed to compensate for the ohmic loss for each design using HFR and Fig. 3-8 shows the activation loss and the mass transfer loss (flooding) [9].

As seen in Fig. 3-8, all four IR-corrected polarization curves are nearly the same for the lowest current density tested, 0.3 A cm^{-2}. This indicates that the activation loss for each design is the same, that the gas is equally supplied to the catalyst in each design, and that the CCMs and MPLs have similar properties.

For Design CNV, the cell voltage gradually decreases due to flooding as the current density exceeds 0.3 A cm^{-2} (Fig. 3-8), with a rapid voltage drop to 0.3 V at 1.7 A cm^{-2}. In contrast, the designs utilizing microcoils (Designs MCC-1, MCC-2, and MCC-3) exhibit less flood performance even at a current density of 1.8 A cm^{-2}.

More significantly, the IR-corrected polarization curves for Designs MCC-1 and MCC-2 are identical (Fig. 3-8). This indicates that the GDL does not participate in the flooding mechanism, because Design MCC-1 utilizes a GDL under the microcoils but its performance is less-flooding. This suggests that if gas is uniformly supplied to the active area with microcoils, a sufficient amount of gas reaches the catalyst layer without being blocked by water.

A.Higier and H. Liu have directly measured the location where flooding occurred in a conventional land/channel structure. They made two different membrane-electrode assemblies (MEAs) with Teflon sheets; one had an active area under just the lands, and the other had the active area under just the channel [10] using a Teflon sheet as a cover. They have found that the land-covered MEA exhibits flood-free performance, while the channel-covered MEA shows flooding, based on their polarization curve. Thus, the product water is not removed easily from under the land, preventing the cathode gas from diffusing into the catalyst layer. From a wider perspective of flow field structure, Design

MCC-1 is similar to the land-covered active area in Ref. [10], and therefore, the observed flood-free performance is reasonable.

V.P. Schulz et al. have demonstrated in their modeling work with a full morphology (FM) model that the liquid water in the GDL is transported along the gradient of capillary pressures [11]. They visualized a 3D liquid water network in a GDL using computational simulations. I.S. Hussaini and C.Y. Wang have recently characterized the water and air permeability for the GDL [12] for the through-plane and in-plane directions. They have shown that the air relative permeability decreases rapidly with increasing water saturation, while water relative permeability increases.

It is not certain that the water saturation occurred during the operation of Design MCC-1, and therefore, it is not clear why the less-flooding performance was seen in this case. According to the rough assumption of the temperature in the GDL described in Section 3.3.4, the temperatures of the GDL for Designs CNV and Design MCC-1 at 1 A cm^{-2} were estimated as 82.6 ºC and 83.6 ºC, respectively. These temperatures indicated that the condensation and evaporation rates for both designs were not very different and that liquid water might be present in the GDL for both designs. Although the studies noted above mention that low air permeability at high saturation could affect fuel cell performance, Design MCC-1 exhibits flood-free performance. Presumably, the gas can travel through the GDL through the capillary fingering liquid water network [13]. It is unlikely that all the pores in the GDL are saturated, allowing diffusion of air. In addition, especially in Design MCC-1, the gas could be supplied more uniformly to the top surface of GDL with microcoils, and almost all the surface was exposed to the gas flow without being plugged by the bipolar-plate; further, liquid water was thought to be removed more easily from the top surface of the GDL under dynamic gas flow along with the microcoils [14]. Therefore, in Design MCC-1, the amount of liquid water in the GDL is probably kept lower, and the distribution of liquid water is kept more uniform, retaining the water saturation at a low level to allow for sufficient gas diffusion. This can be strongly influenced by the temperature and gas velocity, but further study is required for complete characterization.

In Design CNV, the accumulating water under the land cannot be removed because no gas flows over the water, as noted in Ref. [14]. Therefore, the pores under the land most probably suffer high water saturation that prevents gas penetration. In Designs MCC-2 and MCC-3, the microcoils are laid directly on the MPL without a GDL (Fig. 3-1 and Fig. 3-2). These designs exhibit nearly identical, less-flooding performance. There is less space for water accumulation, and the forced convection causes movement of air in the coil directly against the water in the active area. The gas seems to be distributed uniformly onto the catalyst layer.

Further, the water in the MPL does not block airflow. It is thought that the water does not fill all the pores or create a liquid film in the MPL, because the pores are highly hydrophobic, being small and made of PTFE. Consequently, it can be concluded that flooding generation results from a combination of land/channel structure and the GDL.

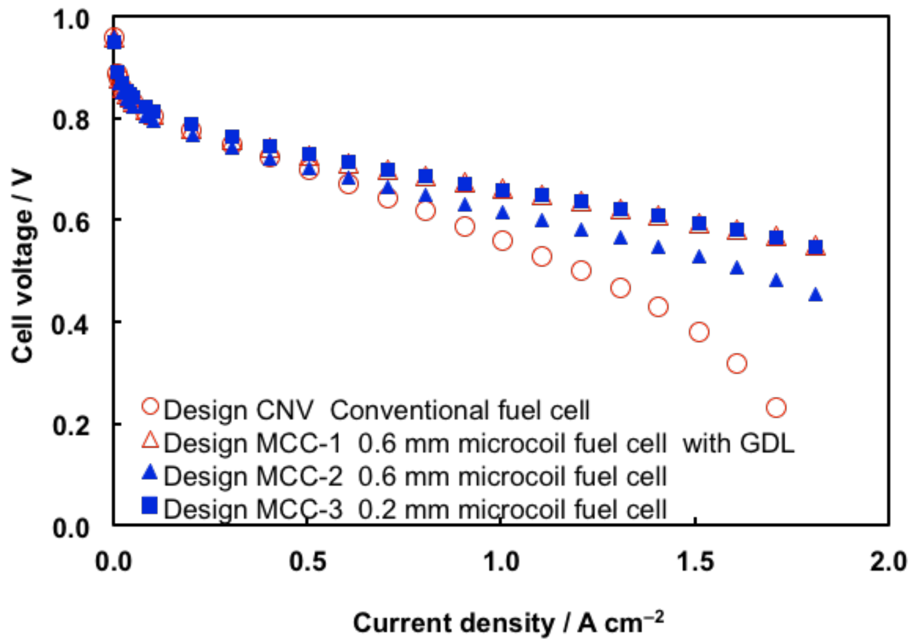

Fig. 3-6. Polarization curves for Design CNV (conventional fuel cell), Design MCC-1 (0.6 mm microcoil with a GDL), and Designs MCC-2 (0.2 mm microcoils without a GDL), and MCC-3 (0.2 mm microcoils without a GDL), obtained under RH_{anode} =100%, $RH_{cathode}$ = 100%, ambient pressure at the outlets, cell temperature = 70 °C, and hydrogen and air supplied in a stoichiometric ratio of 9.0 at 1.5 A cm^{-2}.

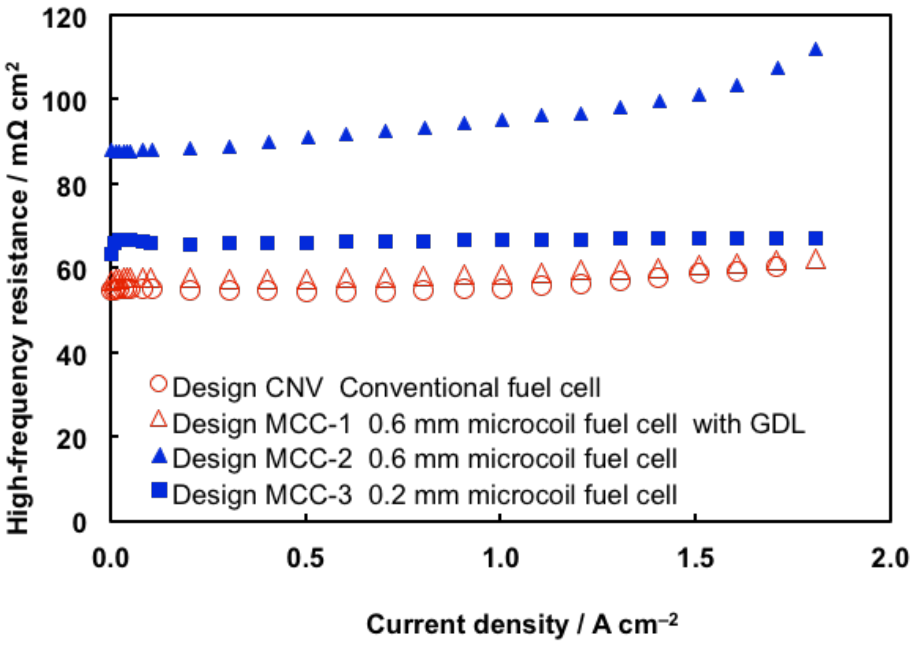

Fig. 3-7. High-frequency resistance (HFR) for Designs CNV, MCC-1–3.

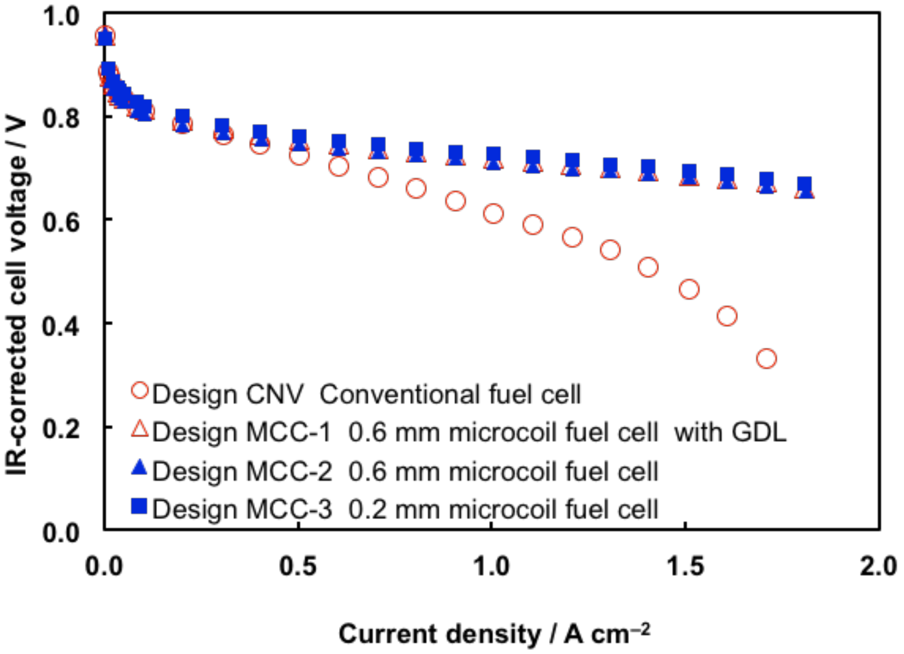

Fig. 3-8. IR-corrected polarization curves for Designs CNV, MCC-1–3.

3.3.2. Stoichiometry Dependence

High cathode stoichiometry α_{air} is generally used to remove product water and reduce flooding [15], but this operation condition results in a significant reduction in system efficiency with higher air flow rate [16]. Designs MCC-1, MCC-2, and MCC-3 showed less-flooding performance using $\alpha_{\mathrm{air}} = 9$ for 1.5 A cm^{-2}. In this section, the performance dependence on stoichiometry is discussed for all four designs.

Fig. 3-9 shows the dependence of cell voltage on cathode stoichiometry α_{air} for all Designs with a current density of 1 A cm^{-2} and 100% RH at 80 ºC. Here, α_{air} is varied from 30 to 1.05 using an air mass flow controller. Design CNV, with a conventional flow field, produces lower voltage than do Designs MMC-1, MCC-2 and MCC-3, which utilize microcoils, in the α_{air} range tested. Even with the higher stoichiometry at $\alpha_{\mathrm{air}} > 10$, Design

CNV suffers from flooding, and the performance begins to degrade at $\alpha_{\text{air}} = 3.0$, with more severe flooding [17]. This straight and parallel design leads to non-uniformity in air streams and catastrophic flooding at low airflow rates [18].

In contrast, the performances of Designs MCC-1, MCC-2 and MCC-3 show less-flooding performance at $\alpha_{\text{air}} = 9.0$, as described in Section 3.3.1 and by the polarization curve in Fig. 3-6. Moreover, the performance does not degrade even at $\alpha_{\text{air}} = 1.2$.

The result for Design CNV indicate that the amount and distribution of liquid water in the GDL seems to be large or non-uniform to block gas diffusion in the GDL even under high stoichiometry at $\alpha_{\text{air}} > 10$; this water could not be removed and the distribution could not be made uniform just by the stoichiometry under these conditions. A straight and parallel flow field is used with a channel width of 1 mm and a land width of 1 mm in Design CNV for the conventional flow field, which is thought to be the structure least amenable to the removal of water [19], but the land/channel structure might have a crucial defect.

In Designs MCC-2 and MCC-3 utilizing microcoils without a GDL, the results obtained are reasonable according to the same logic explaining the less-flooding performance described in Section 3.3.1: direct flow for the entire active area without any liquid water transportation delay in the GDL, and ready air access to the catalyst without any gas diffusion delay in the GDL. Therefore, the cell voltage remains high even at a low stoichiometry value of $\alpha_{\text{air}} = 1.2$.

Design MCC-1 exhibits high voltage at $\alpha_{\text{air}} = 1.2$, similar to CC-2 and MCC-3, even though it has a GDL. This indicates that the GDL does not affect the stoichiometry under these conditions. Since the voltage drop from flooding is larger under wetter conditions, such as 50 ºC and 100% RH [20], the performance of Design MCC-1 may decrease at higher stoichiometry.

As α_{air} is the higher, the cell voltage for all designs increases slightly. This is thought that higher airflow can increase pressure drop and, when the operation pressure is controlled at the outlet of the fuel cell, the higher pressure-drop increase air pressure along with the channel stream. In this case oxygen concentration increases and this can increase cell voltage [21]. Indeed, the pressure drop for Design 3 is thought to be highest with smallest coil diameter, and the cell voltage increase along with the stoichiometry is largest. The pressure drop effect of the stoichiometry, however, seems to be little of negligible in this stoichiometry range compared to the flooding effect. In this study, small and same active area is used for all the designs and this causes the different pressure drop. In the actual industrial design, the pressure drop should be totally considered also with active area size and aspect ratio and system efficiency as well.

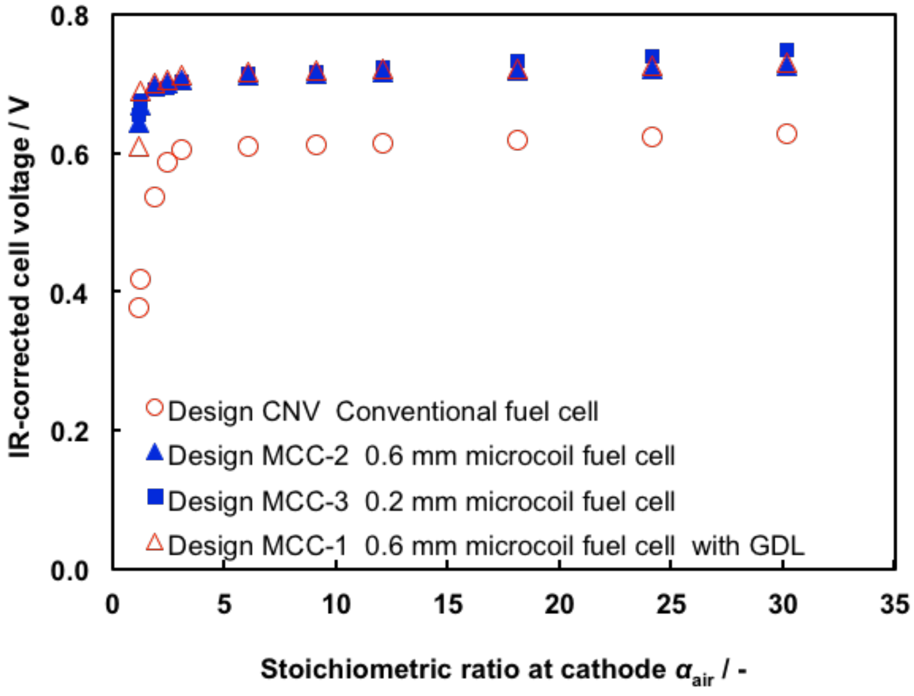

Fig. 3-9. Dependence of IR-corrected cell voltage on cathode stoichiometry αair for Designs CNV, MCC-1–3.

3.3.3. HFR and Electron Conducting Pathway

Fig. 3-7 shows the HFR for all the Designs. Designs CNV and MCC-1 utilizing a GDL exhibit an HFR of 60–70 mΩ cm^2, in agreement with the values published in the literature [22–24]. Designs MCC-2 and MCC-3, which use microcoils directly on the MPL at the cathode, exhibit a relatively higher HFR. These results indicate that electrons can move from the MPL/catalyst-layer to the GDL because the GDL makes surface-to-surface contact with the entire active area, but the microcoils do not cover the entire active area and can make only point-to-surface contact. The microcoils are placed only on the MPL/catalyst layer in the interval of the coil diameter, meaning that the set of microcoils has fewer contact points with the MPL/catalyst layer.

Fig. 3-10 shows a schematic depicting the electron transfer from the catalyst layer to the bipolar plate. Table 3-2 shows the resistivity of the catalyst layer, MPL, and GDL in the in-plane and through-plane directions. The assumptions shown in Fig. 3-10 indicate that each design has a different electron transfer pathway from the catalyst to the bipolar plate. In Designs CNV and MCC-1, electrons in the land of the bipolar plate coming from an external load first travel horizontally in the GDL, then move vertically to the MPL, and move vertically to the catalyst layer under the channel. In contrast, in Designs MCC-2 and MCC-3, the electrons in the microcoil travel horizontally in the MPL and then move vertically to the catalyst layer between the microcoils. The resistivity of the MPL is 10^4 times larger than that of the GDL (Table 3-2), meaning that Designs MCC-2 and MCC-3 probably suffers larger ohmic losses due to in-plane MPL resistance, resulting in a higher HFR than that in Designs CNV and Design MCC-1.

Even though Designs MCC-2 and MCC-3 are both essentially microcoils without a GDL, the HFR of Design MCC-2 is higher than that of Design MCC-3. This result can be explained by the distance of the in-plane MPL electron-conducting pathway. Design MCC-2 uses 0.6 mm microcoils and Design MCC-3 uses 0.2 mm microcoils, introducing a difference in the diameter that affects the distance traveled by electrons transferred through the MPL in the in-plane direction, thus incurring ohmic loss along the MPL. The in-plane MPL distance in Design MCC-2 is three times that in Design MCC-3, and if the current is supplied uniformly from catalyst layer to MPL, the resistance through MPL for Design MCC-2 is 9 times that for Design MCC-3 with the equation

$$R_{\mathrm{MPL}} = \int_{contact\ point}^{half\ pitch} \rho_{\mathrm{MPL}} \times D_{\mathrm{MPL}} \tag{3-1}$$

where R_{MPL} is electric resistance through the MPL, ρ_{MPL} is the electric resistivity of MPL, and D_{MPL} is the distance from the contact point of microcoil|MPL, as shown in Fig. 3-11. In the experimental HFR in Fig. 3-7, however, because the resistance of the membrane and the resistance of the two catalyst layers are 25 mΩ cm^2 and 20 mΩ cm^2 respectively [1], then the resistances through MPL for Design MCC-2 (0.6 mm coil) and MCC-3 (0.2 mm coil) are approximately estimated as 42.9 mΩ cm^2 and 21.3 mΩ cm^2 respectively. In this estimation, this MPL's resistance of Design MCC-2 is only 1.4 times larger than that of Design MCC-3.

This discrepancy arises because the electron resistance between the MPL and the microcoil were formed by point-contact. In such a case, the contact resistance could not be explained by the length of the electron-conducting pathway but by the number of contact points and the spot area of a single contact point. R. Holm investigated the point-contact resistance between a flat pate and the contact points equally dispersed in a specific area A [25]. They found that the resistance R_C can be expressed as

$$Rc = \frac{\rho \sqrt{\pi}}{4 \sqrt{S} \sqrt{N}} \tag{3-2}$$

where ρ is the electric resistivity of a flat plate, S is the total contact area of the actual contact point, and N is the number of contact points. In Designs MCC-2 and MCC-

3, the contact points between the MPL and the microcoils were dispersed in the same active area A_{Active} and the conductivities of the MPL ρ_{MPL} were the same for each design. The area of the single contact point formed between the MPL and the lower end of the microcoil is not accurately known, but it can be assumed that the compression pressure of the fuel cell could press the microcoil down on the MPL and that the microcoil fiber would sink into the MPL to a depth of 1 μm. The MPL should be flexible enough to make the contact with the entire 1 μm depth of the microcoil fiber. To calculate the contact area, 3D CAD (Google Sketch-UP, Google Inc. USA) was used, as shown in Fig. 3-12. Incidentally, the Prescale film (mechanical pressure sensitive film, Fujifilm) could not detect each single point, and this can be due to too low resolution for the small contact point. The area of the single point contact for Designs MCC-2 and MCC-3 was 764 μm^2 and 443 μm^2, respectively. The number of contact points N for Designs MCC-2 and MCC-3 was 9435 and 27750, respectively. Therefore, the total contact area of the actual contact points in Designs MCC-2 and MCC-3 was 7.2 mm^2 and 12.3 mm^2, respectively. According to equation (1), the contact resistance of Design MCC-2 is 2.2 times larger than that of Design MCC-3. The value does not agree with the actual HFR values.

The discrepancy may be due to the area of the single contact point because it is unknown in the current study, and then, the 1 μm-depth contact of the microcoil with the MPL was assumed. Therefore, this did not represent the actual contact area. For further studies, the mechanical properties of the MPL should be obtained to determine the actual contact area by performing experiments or computational calculations, for example, using a finite element model (FEM). However, consideration of the point contact between the microcoil and the MPL is thought to be significant even with the aforesaid discrepancy.

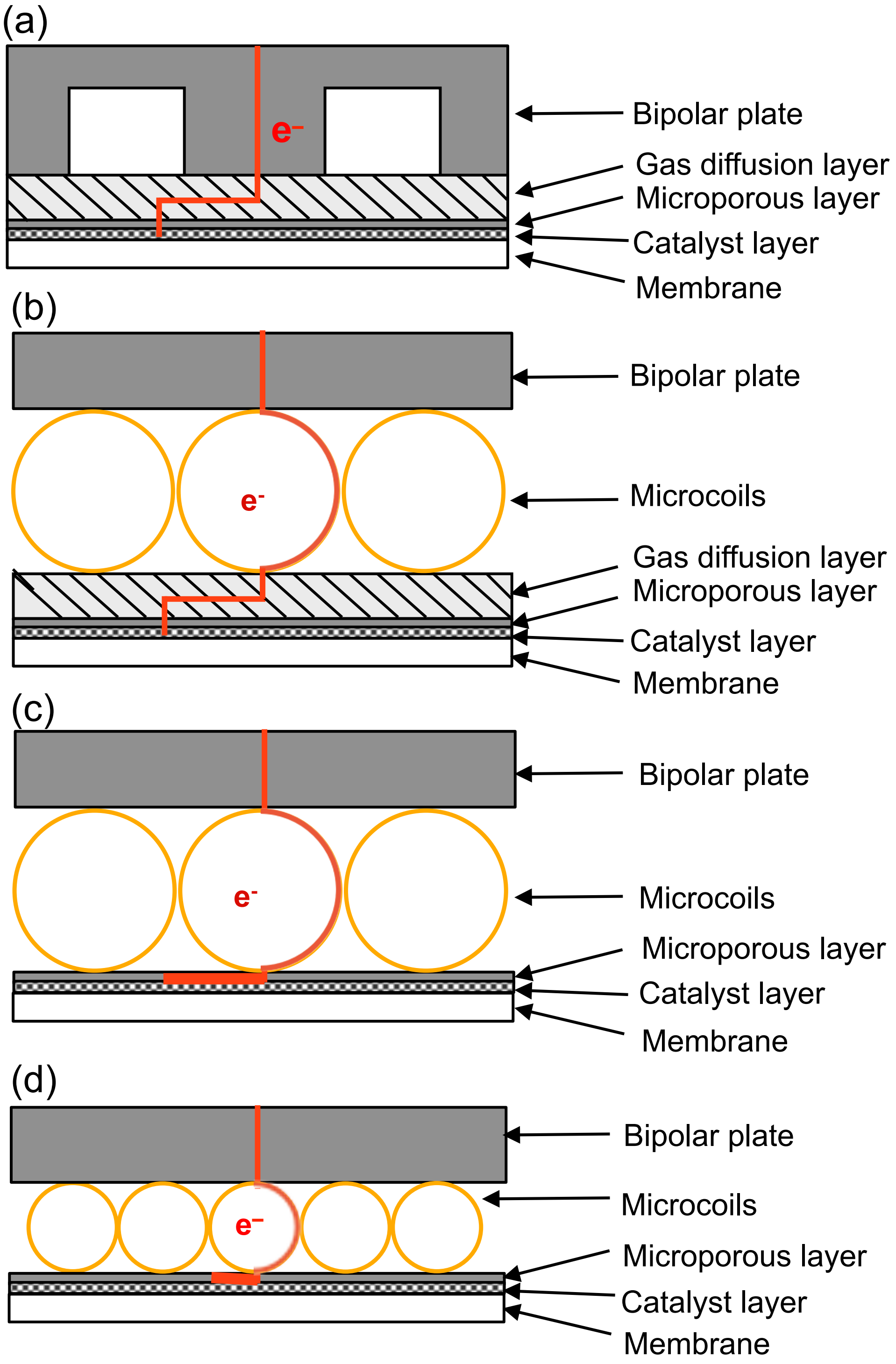

Fig. 3-10. Schematic images of electrical conduction at the cathode in Designs; (a) CNV, (b) MCC-1, (c) MCC-2, (d) MCC-3.

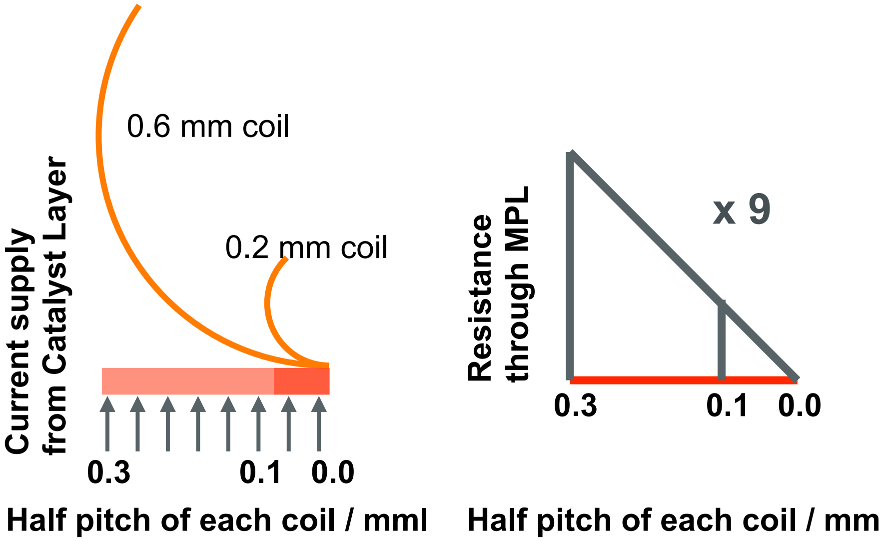

Fig. 3-11. Schematic images of the resistance through MPL in-plane direction.

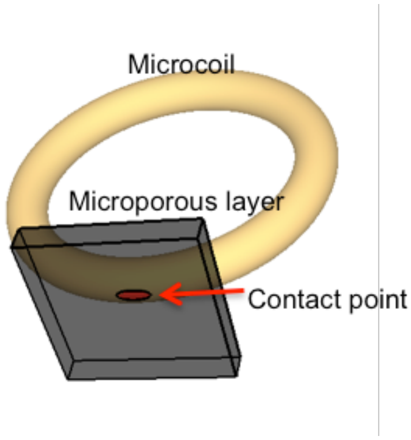

Fig. 3-12. Contact area of microcoil|MPL represented with 3D CAD.

Table 3-2. In-plane and through-plane electron resistivity at 1 MPa compression pressure.

	In-plane	Through-plane
	Ω cm	Ω cm
Catalyst layer	9.9	2.9
MPL	2.5	9.8×10^{-1}
GDL	2.5×10^{-4}	7.3×10^{-4}

3.3.4. HFR and membrane dry-out

During PEM-FC operation, water is produced by the oxygen reduction reaction at the cathode, leading to a higher water concentration at the cathode than that at the anode. Water thus diffuses from the cathode to the anode so as to equilibrate the concentrations between the two compartments. This phenomenon is widely known as back diffusion [26]. At the same time, the water at the anode moves to the cathode along with proton transfer through the membrane because the protons are encapsulated by solvation shells, meaning that proton transfer results in net water transfer as well. This phenomenon is known as electro-osmotic drag [27]. At low current densities, back diffusion prevails over electro-osmosis, while the opposite is true at high current densities, meaning that the anode tends to dry out even if the cathode is well hydrated [28]. The membrane resistivity strongly depends on the water content of the membrane, and thus, membrane dehydration can cause increased HFR.

Fig. 3-7 reveals that the HFR for all the designs increases with increasing current density. However, the nature of the increased HFR is different for each design. The HFR for Designs CNV and MCC-1, utilizing a GDL, is similar and starts to increase slightly at a current density of 1.2 A cm^{-2}, from 55 to 60 mΩ cm^2. The HFR for Design MCC-2, however, starts to increase earlier, at 0.3 A cm^{-2}, from 90 to 120 mΩ cm^2. Finally, the HFR for Design MCC-3 increases only slightly, from 66 to 67 mΩ cm^2.

M.M. Mench et al. [29] and S. He et al. [30] have mentioned that the increase in the electrolyte membrane temperature from the initial temperature at the open circuit is

12–15 °C at a current density of 1 A cm^{-2}, which can cause membrane dehydration. In this study, the membrane temperature is not certain, and only the bipolar temperature was monitored for all the designs through the current density range. Hence, it is difficult to estimate the HFR increase based on the membrane temperature increase. Instead, we have evaluated the thermal resistance for the GDL, the microcoil and the MPL, as described in Section 3.2.1, to evaluate whether these thermal resistances affect the membrane temperature through heat transfer from the membrane to the bipolar plate, the temperature of which is maintained at 80 °C using a sheet-heater and thermocouples.

Table 3-3 shows the thermal resistance of the 190 μm TGP-H-060 GDL and the 280 μm TGP-H-090 GDL, as well as the 0.6 and 0.2 mm microcoils. The thermal conductivity of the GDL is also calculated using the thermal resistances for the different thicknesses in order to confirm the reasonableness of the measurement, comparing the data obtained with that from manufacturer's data sheet.

The thermal conductivity of the GDL is 1.7 W m^{-1}K^{-1}, agreeing well with the value listed in the literature, 1.80 ± 0.27 W m^{-1}K^{-1} (Table 3-3) [31], giving us confidence in the accuracy of our results. It is difficult to measure and calculate the thermal conductivity of the microcoils due to the two different diameters used. Unavoidably, the thermal resistance also reflects the contact resistance of copper plate (Fig. 3-5). However, we use the thermal resistance data to estimate the temperature rise in the membrane.

Using the thermal conductivity data for the GDL and the MPL as well as based on the two different thicknesses tested, in addition to the thermal resistance data of the microcoils (Table 3-3), the temperature increase in the membrane is estimated under the following assumptions:

(1) uniform heat generation in the active area

(2) uniform heat transfer to the next layer only in the through-plane direction

(3) heat generation calculated with $I \cdot (E_{th} - E_{cell})$. I : cell current, E_{th} is thermonutral voltage (HHV), E_{cell} is cell voltage

(4) the heat divided equally to the cathode and anode

(5) generated water removed as liquid

(6) no heat generation in the MPL, GDL, or microcoil

(7) no contact heat resistance

(8) no secondary heat transfer or conduction

(9) constant bipolar temperature

(10) constant thermal conductivity in the temperature range used in this estimation

For the assumption (3), there are basically four sources of heat generation in a PEMFC, namely the entropic heat of reactions, the irreversible heat of electrochemical reactions, heat from the ohmic resistances and heat from the condensation of water vapor [32]. E_{tn} is known as the thermoneutral voltage [33], which represents the imaginary maximum voltage of a fuel cell assuming all the 4 energies is converted to the electric energy. E_{cell} and I are the cell operating voltage and the current. Here E_{tn} includes the released energy of the product water to be the liquid phase, based on the higher heating value (HHV) because the product water assumed to be removed at this time as the assumption (5), and the corresponding values for the HHV is 1.48 V [34].

Fig. 3-13 shows the temperature increase in the CCM. Design CNV, featuring a conventional flow field, produces results similar to those obtained by M.M. Mench [29]; however, the results also reveal that the temperature increases of Designs CNV and MCC-1 utilizing the GDL are twice those of Designs MCC-2 and MCC-3, and in addition, the range of temperature increase in Designs MCC-2 and MCC-3 is similar. This result provides discrepant explanations for the differences in the HFR increase in Fig. 3-7. The HFR increase in the case of Designs CNV and MCC-1 was small and that in Design MCC-2 was the highest, but the temperature increases were not similar to the HFR increases. This result is not unreasonable because the thermal resistances for Designs CNV, MCC-1, MCC-2 and MCC-3 under assumptions (1)–(10) are 1.57, 2.22, 1.09, and 0.97 °C W^{-1}, respectively, and these are on the similar order as the temperature increase estimated in Fig. 3-13.

According to the HFR increase in Fig. 3-7, the temperature increase should be in the order Design MCC-2 > MCC-1 $\simeq$ CNV > MCC-3, but the estimated temperature increase is in the order Design MCC-1 > CNV > MCC-2 > MCC-3. This indicates that the thermal resistance of Design MCC-2 with the 0.6-mm microcoil should be underestimated under the assumptions, especially assumption (2), which is uniform heat transfer only in the through-plane direction. In the actual fuel cells with 0.6-mm microcoils, heat is transferred in-plane in the MPL between the two coils, and these contacts are formed by point-contact, similar to the electron conduction path described in Section 3.3.1. Unfortunately, the experiment depicted in Fig. 3-5 should underestimate the effect of horizontal conduction because the thermal conductivity of copper is three times greater in magnitude than the MPL, implying that the copper-plate/microcoil system should have a much lower thermal resistance than the MPL/microcoil system. In future studies, we will estimate the thermal resistance of the MPL/microcoil system. In addition, we will calculate the temperature rise in the fuel cell via 3D FEM with non-isotropic thermal conductivity of the MPL, contact thermal resistance against the load pressure of the end plates, and coupling of electron conduction with ohmic heat generation in the MPL and other elements of the fuel cell.

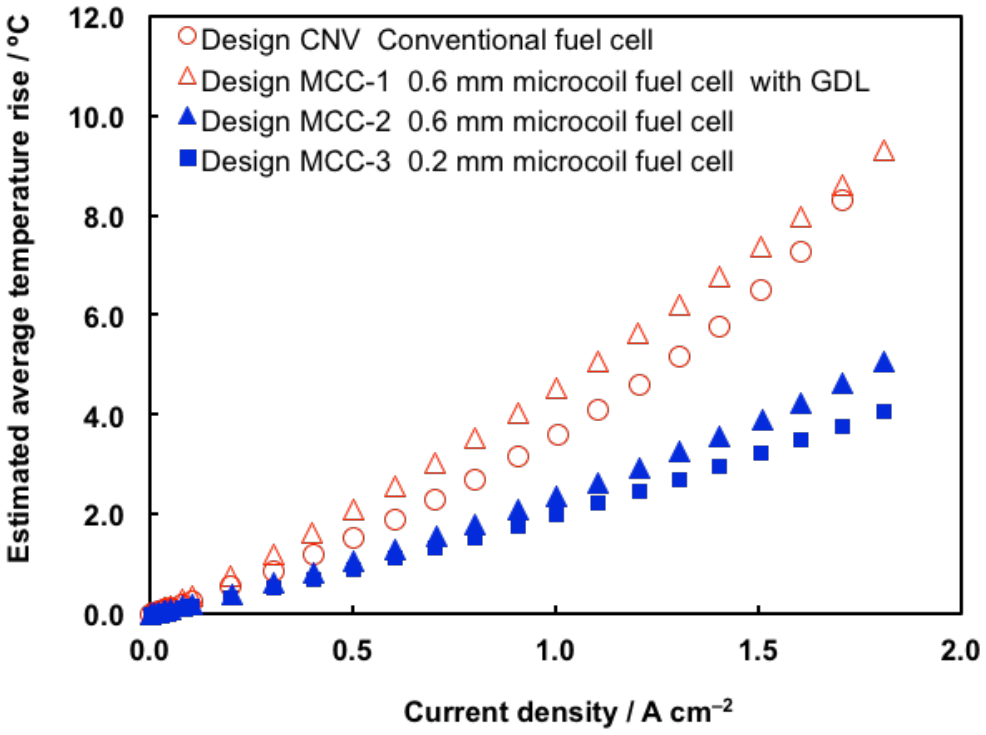

Fig. 3-13. Estimated average temperature increase for Designs CNV, MCC-2, and MCC-3. For the microcoil, thermal resistance data were used; for the GDL and MPL, thermal conductivity and thickness data were used to calculate the temperature increase.

Table 3-3. Through-plane thermal resistance and thermal conductivity of the GDL, the microcoil, and the MPL at 1 MPa compression pressure.

	Measured Thermal Resistance	Measured Thermal Conductivity	Reported Thermal Conductivity
	$\mathrm{m^2\,K\,W^{-1}}$	$\mathrm{W\,m^{-1}\,K^{-1}}$	$\mathrm{W\,m^{-1}\,K^{-1}}$
GDL (TGP-H-060, 190 μm)	5.1×10^{-4}	1.7	1.80 ± 0.27 [31]
GDL (TGP-H-090, 280 μm)	5.6×10^{-4}		
Microcoils (200 μm)	2.6×10^{-4}	-	-
Microcoils (600 μm)	3.3×10^{-4}		
Stainless Steel (SUS316)	-	-	16.7
MPL (40 μm)	2.2×10^{-4}	0.4	0.3 [7]
MPL (60 μm)	6.7×10^{-4}		

3.4. Conclusion for Microcoil Fuel Cell

In this study, the IV performance, stoichiometry performance, and HFR for microcoil fuel cells were characterized. Electrical conductivities for each element were measured to explain the HFR difference between the microcoil fuel cells and the conventional fuel cell, and thermal conductivities were also measured to elucidate the behavior of HFR against current density with a simple estimation. The main conclusions drawn from this study are as follows:

1. Microcoil fuel cell can achieve less-flooding performance, less-dryout performance with lower HFR rise, and better air-management performance with uniform air supply.
2. The GDL itself had little or no observable effect on either the IV or stoichiometry performance with flooding. Only the combination of Land/Channel structure and GDL promoted non-uniform gas distribution and large flooding.
3. The HFR of the microcoils without a GDL was higher than that of the conventional

fuel cell, due to differences in the electron conduction pathway. Electrons were conducted horizontally in the in-plane direction in the MPL, and in-plane electron conductivity is key to enhancing microcoil fuel cell performance.

4. The temperature increase with uniform heat transfer only in the through-plane direction could not represent the actual microcoil fuel cell, with underestimation of the thermal resistance between the MPL and the microcoil, similar to electron conductivity.

In future studies, it should be clarified that the voltage drop through the electron conductivities of the fuel cell components and the contact resistances between these components under a certain compression pressure of the end plates, via 3D FEM. Several conductive MPL samples will be prepared and tested them in the fuel cell to validate the effect. In addition, the temperature rise in the fuel cell should be calculated via 3D FEM with non-isotropic thermal conductivity of the MPL, contact thermal resistance against the load pressure of the end-plates, and coupling of electron conduction with ohmic heat generation in the MPL and other elements of the fuel cell.

Other than the larger electrical resistance issues for microcoil fuel cell, the high cost of microcoils must also be considered, especially if being mass-produced. Furthermore, tightly setting a number of microcoils onto the bipolar plate is quite time consuming. Therefore, we have to reconsider another method to reduce the cost and increase the productivity. We will report corrugated-mesh fuel cell utilizing corrugated-mesh as a same roll as microcoils in the next chapter 4.

Bibliography for Chapter 3

[1] M. Mathias, J. Roth, J. Fleming, W. Lehnert, W. Vielstich, H. Gasteiger, A. Lamm (Eds.), Handbook of Fuel Cells: Fundamentals, Technology and Applications, John Wiley & Sons, New York, 2003, vol. 3.

[2] T.E. Springer, T.A. Zawodzinski, M.S. Wilson, S. Gottesfeld, J. Electrochem. Soc. 143 (1996) 587-599.

[3] N.S. Siefert, S. Litster, J. Power Sources 196 (2011) 1948–1954.

[4] H. Yamada, T. Hatanaka, H. Murata, Y. Morimoto, J. Electrochem. Soc. 153 (2006) A1748–A1754.

[5] N. Cunningham, M. Lefèvre, G. Lebrun, J.P. Dodelet, J. Power Sources 143 (2005) 93–102.

[6] G. Karimi1, X. Li, P. Teertstra, Electrochim. Acta 55 (2010) 1619–1625.

[7] G. Unsworth, N. Zamel, X. Li, Int. J. Hydrogen Energy 37 (2012) 5161-5169.

[8] F.P. Incropera, D.P. DeWitt, Fundamentals of Heat and Mass Transfer, fourth ed., John Wiley & Sons, New York, 1996.

[9] M.V. Williams, H.R. Kunz, J.M. Fenton, J. Electrochem. Soc. 152 (2005) A635–A644.

[10] A. Higier, H. Liu, J. Power Sources 193 (2009) 639–648.

[11] V.P. Schulz, J. Becker, A. Wiegmann, P.P. Mukherjee, C.Y. Wang, J. Electrochem. Soc. 154 (2007) B419-B426.

[12] I.S. Hussaini, C.Y. Wang, J. Power Sources 195 (2010) 3830–3840.

[13] E. Aker, K.J Måløy, A. Hansen, G.G. Batrouni, Transp. Porous Media 32 (1998) 163–186.

[14] B.A. McCain, A.G. Stefanopoulou, I.V. Kolmanovsky, Chem. Eng. Sci. 63 (2008) 4418–4432.

[15] W.R. Mérida, G. McLean, N. Djilali, J. Power Sources 102 (2001) 178–185.

[16] R.S. Gemmen, C.D. Johnson, J. Power Sources 159 (2006) 646–655.

[17] N. Pekula, K. Heller, P.A. Chuang, A. Turhan, M.M. Mench, J.S. Brenizer, K. Ünlü, Nuclear Instruments and Methods in Physics Research A 542 (2005) 134–141.

[18] T.V. Nguyen, J. Electrochem. Soc. 143 (5) (1996) L103–L105.

[19] X. Li, I. Sabir, J. Park, J. Power Sources 163 (2007) 933–942.

[20] A. Hakenjos, H. Muenter, U. Wittstadt, C. Hebling, J. Power Sources 131 (2004) 213–216.

[21] S. Gottesfeld, T.F. Fuller, Proton Conducting Membrane Fuel Cells II: Proceedings of the Second International Symposium on Proton Conducting Membrane Fuel Cells II, The Electrochemical Society, New Jersey, 1999

[22] J.P. Owejan, T.A. Trabold, D.L. Jacobson, D.R. Baker, D.S. Hussey, M. Arif, Int. J. Heat Mass Transfer 49 (2006) 4721–4731.

[23] S.J.C. Cleghorn, D.K. Mayfield, D.A. Moore, J.C. Moore, G. Rusch, T.W. Sherman, N.T. Sisofo, U. Beuscher, J. Power Sources 158 (2006) 446–454.

[24] J.P. Owejan, J.J. Gagliardo, J.M. Sergi, S.G. Kandlikar, T.A. Trabold, Int. J. Hydrogen Energy 34 (2009) 3436–3444.

[25] R. Holm, Electric Contacts, 4th ed., Springer, New York, 1967.

[26] N. Yousfi-Steiner, P. Moçotéguy, D. Candusso, D. Hissel, A. Hernandez, A. Aslanides, J. Power Sources 183 (2008) 260–274.

[27] J. Larminie, A. Dicks, Fuel Cell System Explained, first ed., John Wiley & Sons, New York, 2000.

[28] P. Sridhar, R. Perumal, N. Rajalakshmi, M. Raja, K.S. Dhathathreyan, J. Power Sources 101 (2001) 72–78.

[29] M.M. Mench, D.J. Burford, T.W. Davis, “In situ temperature distribution measurement in an operating polymer electrolyte fuel cell,” Proceedings of IMECE ‘03 International Mechanical Engineering Congress and Exposition, Washington, D.C., Nov. 16–21, 2003.

[30] S. He, M.M. Mench, S. Tadigadapa, Sensor. Actuat. A-Phys. 125 (2006) 170–177.

[31] M. Khandelwal, M.M. Mench, J. Power Sources 161 (2006) 1106–1115.

[32] H. Ju, H. Meng, C.Y. Wang, Int. J. Heat and Mass Transfer, 48 (2005), 1303–1315.

[33] X. Li, Principles of fuel cells, Taylor & Francis, New York, 2006.

[34] R. O’Hayre, S.W. Cha, W. Colella, F.B. Prinz, Fuel cell fundamentals, 2nd ed., John Wiley & Sons, New York, 2009.

Chapter 4. Corrugated-mesh Fuel Cell without GDL

4.1. Introduction for Corrugated-mesh Fuel Cell

In a previous chapter 3, a performance of 0.55 V at 1.8 A cm^2 was achieved without a significant voltage drop, even at a relatively high current density of over 1 A cm^2, utilizing tightly aligned microcoils in the flow channel without a GDL. The performance of conventional flow fields with GDLs have also measured; the performance showed a severe voltage drop starting at a relatively low current density of 0.6 A cm^2. In general, GDLs work by distributing the gas from the flow channel to the land underneath in a conventional flow field [1]; however, when the GDLs and channel/land structure are combined, the water cannot be removed from underneath; this water accumulation results in a non-uniform blockage of gas supply to the catalyst layer, the well-known phenomenon of electrode flooding, which significantly decreases fuel-cell performance along with an accompanying increase in current density [2]. It is concluded that the microcoil flow channel can supply the reactant gas uniformly to the catalyst layer. Nonetheless, the GDL-less microcoil flow channel shows a larger high-frequency resistance (HFR) than conventional flow fields with GDLs. Due to fewer contact points between the microcoils and microporous layer (MPL), electron conduction occurs in the in-plane direction of the MPL, which causes a larger HFR in the microcoils with higher contact and concentration resistance from the point-to-surface contact on the MPL.

By the way, tightly setting a number of microcoils onto the bipolar plate is quite time consuming. To improve these practical production issues, we did idea creation as follows, ellipse-shape microcoil, which can reduce the number and keep the height of the microcoils with wider width and same height, rectangle-shape microcoil, which can be easily set tightly on the bipolar-plate keeping the same height and reducing the number of the microcoils with wider width, all-in-one coil unit with welding, which can be easily handled in the production. These ideas, however, are thought to take still high cost, and corrugated-mesh may have similar structure and also may have similar roll for the flow field as microcoils.

4.2. Preparation of Fuel Cell and Components

4.2.1. Preparation of Corrugated-mesh

The corrugated mesh flow channel was prepared with a stainless-steel mesh and corrugating roll. The stainless-steel mesh (nets101 Co., Ltd, Shimizu, Japan) was a twill weave-type SS316L material of 300-mesh with a fiber diameter of 50 μm. The cross-section shape of the corrugated mesh was triangular with a height of 0.3 mm and length of 0.3 mm. To corrugate the mesh, a customized corrugating roll was fabricated (MIKI SEISAKUSYO CO. LTD., Osaka, Japan) as shown in Fig. 4-1. The template grooves were first machined on the surface of the roll along the direction of the circumference, the plain mesh was inserted between the two rolls, and the fluted shape was finally transferred to the mesh under a certain compression pressure. Fig. 4-2 shows an optical microscope image of top-view of the corrugated-mesh and Fig. 4-3 shows an optical microscope image of a cross-section of the corrugated-mesh. Two different flow-channel patterns were formed in the gas-flow direction, namely a straight pattern (straight corrugated mesh) and wavy pattern (wavy corrugated mesh) as shown in Fig. 4-4. The straight pattern and wavy pattern were grooved on the template roll in the same triangular cross-section for both patterns. The wavy pattern adopted the shape of a sine curve with a length of 0.6 mm and amplitude of 0.2 mm also grooved on the roll.

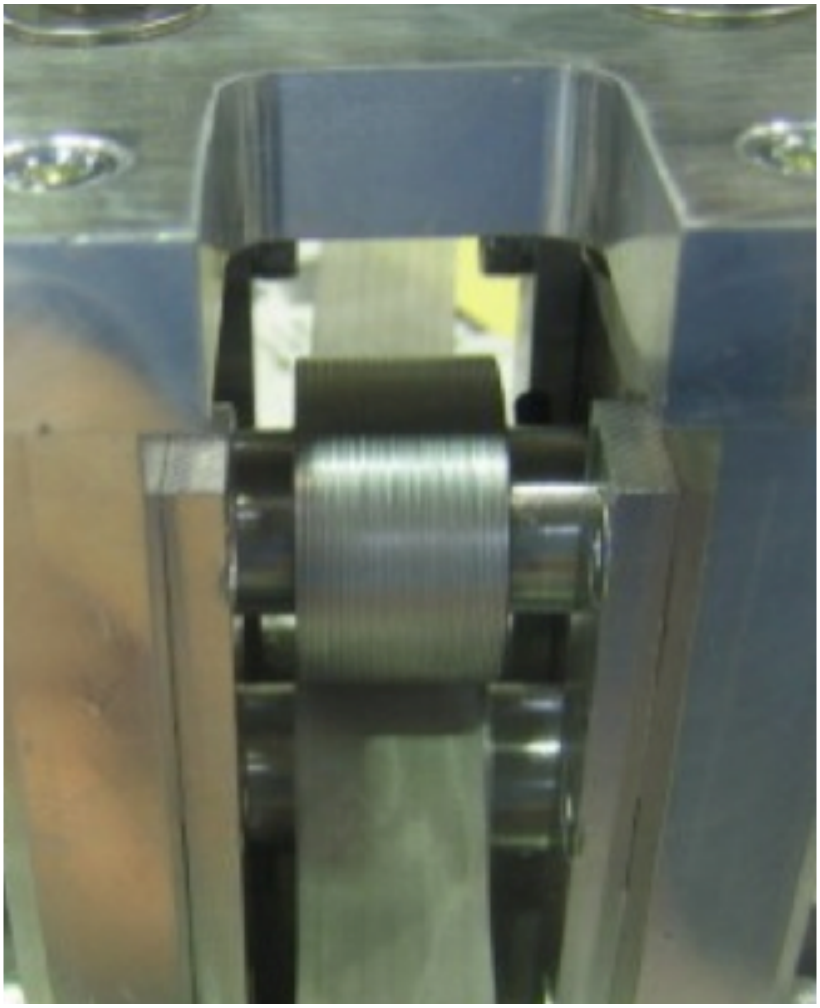

Fig. 4-1. Image of the roll corrugator used for production of corrugated mesh.

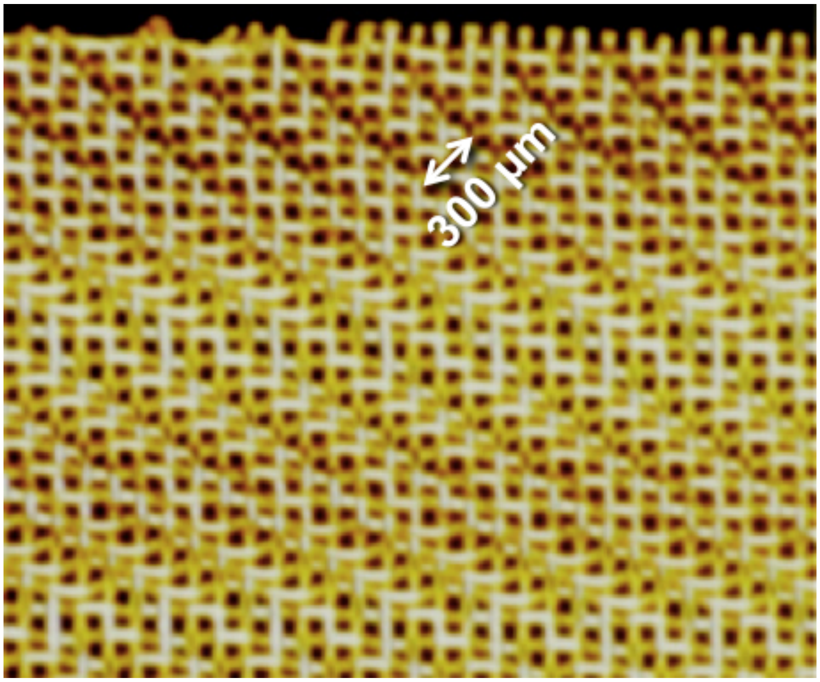

Fig. 4-2. Image of the corrugator with gold-plating.

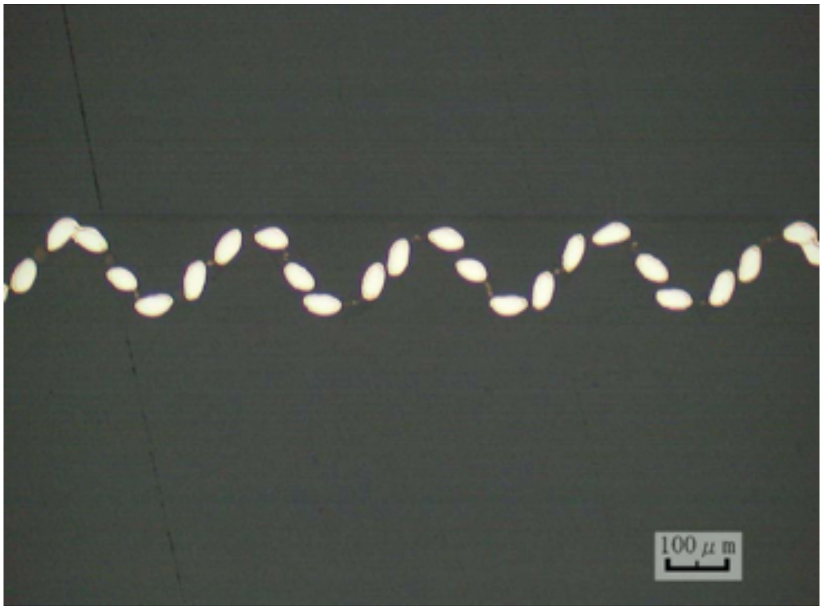

Fig. 4-3. Optical microscopic image of a cross section of the corrugated-mesh.

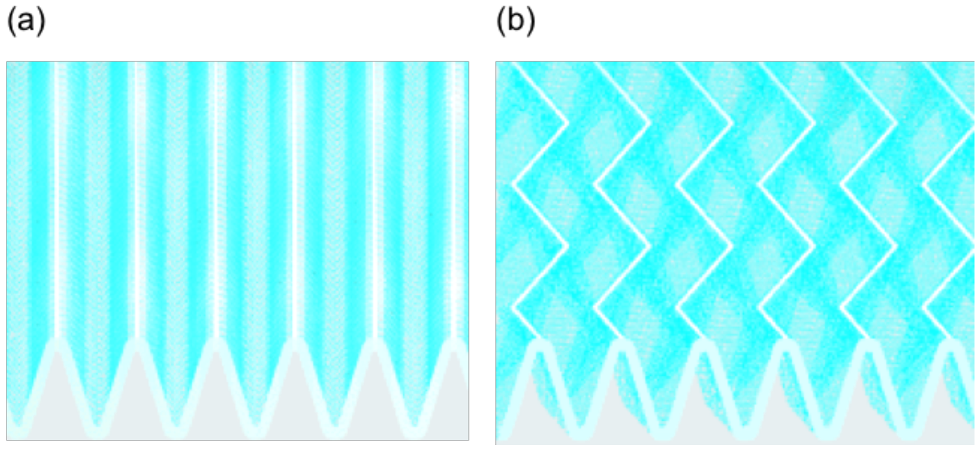

Fig. 4-4. Schematic CAD images of (a) straight corrugated-mesh and (b) wavy corrugated-mesh.

4.2.2. Preparation of MPLs

MPLs were used in the anode and cathode catalyst layers to control fuel-cell water management [3]. Generally, the MPL is coated on the GDL; however, in the present study of GDL-less fuel cells, a free-standing MPL was required for use between the catalyst layers and corrugated mesh flow channels. CB-MPL was used, which was made with the same method in the previous section 3.1.1 for microcoil fuel cell. The electron-conducting pathway from the catalyst to the bipolar plate in the present fuel cells is thought to be different from conventional fuel cells that utilize GDLs. The electron is first transferred vertically to the MPL and then moved horizontally within the MPL to the corrugated mesh contact point. To observe this effect, four different MPLs were fabricated having different conductivities using four different materials, and the in-plane and through-plane conductivities of these MPLs were measured.

The four different MPLs prepared with varying conductivities used the following materials: powdered carbon black (CB; Denka Black, Denki Kagaku Kogyo K.K., Tokyo, Japan); powdered graphite flake (GF; BF-1AT; diameter: 9 µm; thickness: 1 µm; Chuetsu Graphite Works, Osaka, Japan); powdered silver flake (SF; Ag-XF301; diameter: 7 µm; thickness: 1 µm; Fukuda Metal, Kyoto, Japan), and; through-hole stainless-steel foil with gold plating (SS; Hirai Seimitsu Kogyo Co., Gifu, Japan). The four MPLs were prepared to make each MPL sheet as shown in Fig. 4-5, as follows: (1) CB-MPL: CB, a polytetrafluoroethylene (PTFE) aqueous dispersion (D-1, Daikin Industries Ltd., Osaka, Japan), nonionic surfactant (Triton X-100, SigmaeAldrich), and DI water were mixed with zirconia beads (1 mm) in a bead mill for 3 h at 400 rpm with a weight ratio of CB:PTFE:surfactant:water = 5:1:20:20. This solution was used to impregnate an expanded PTFE porous sheet (30 µm thickness, Poreflon Membrane, Sumitomo Electric Industries Ltd., Osaka, Japan), which was then dried at 350 ºC for 60 min. (2) GF-MPL: GF, a PTFE aqueous dispersion, and ethanol with a weight ratio of GF:PTFE:ethanol = 5:1:5 were mixed, and the resulting paste was hot-pressed at 350 ºC and 3 MPa for 10 min with a 40 µm-thick stainless-steel shim to control the compression thickness. (3) SF-MPL: SF, a PTFE aqueous dispersion, and ethanol with a weight ratio of SF:PTFE:ethanol = 5:1:5 were mixed, and the resulting paste was hot-pressed at 350 ºC and 3 MPa for 10 min with a 40 µm-thick stainless-steel shim to control the compression thickness, (4) SS-MPL: a stainless-steel foil of 40 µm thickness was chemically etched to make through-holes having 30 µm diameters, where the minimum gap to the next hole is 30 µm for the gas supply to reach the catalyst layer, and finally was electroplated with 1 µm-thick gold, as shown by F.Y. Zhang [4]. Here, an expanded PTFE membrane was used for the CB-MPL to maintain sufficient strength for handling; because CB is nano-sized with a spherical shape, the CB-MPL without the expanded PTFE was too brittle to handle during fuel-cell assembly. In contrast, GF and SF materials were micron-sized and plate-shaped such that the flakes were well aligned after hot-pressing, and were not too brittle to use in the subsequent evaluations.

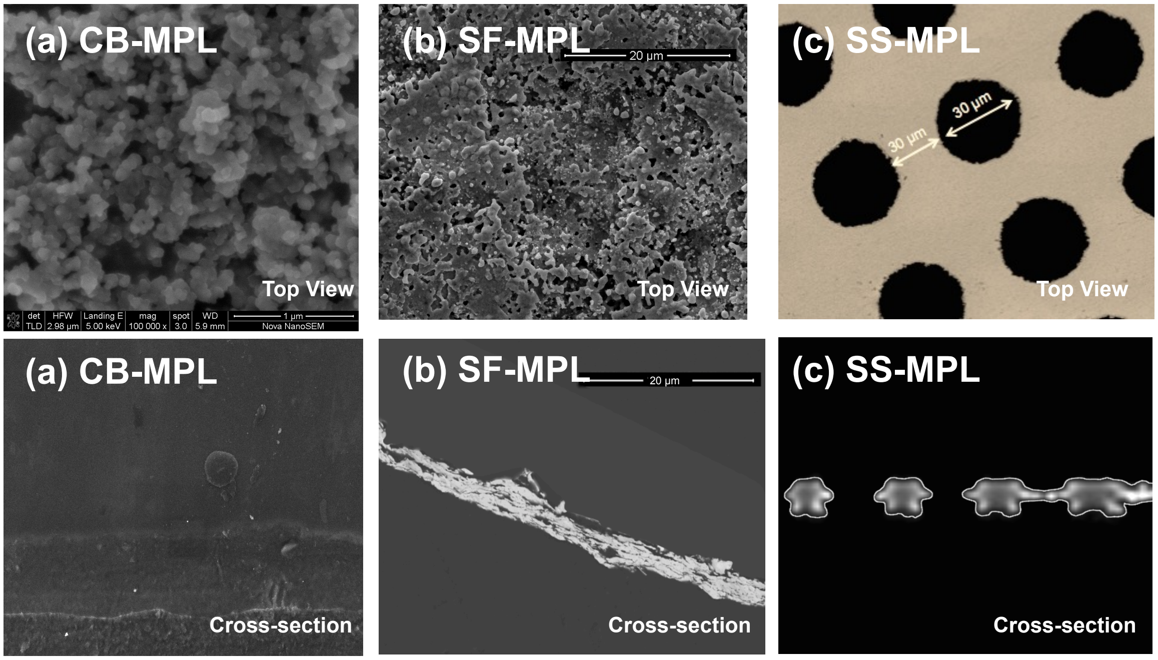

Fig. 4-5 Images of (a) CB-MPL, (b) SF-MPL, and (c) SS-MPL. Upper images are for top view and lower images are cross-section.

4.2.3. Preparation of Fuel Cell

The bipolar plates for the fuel cell used in this study had 5 cm^2 active areas (1 cm 5 cm) made of graphite (Mechanical Carbon Industry, Kanagawa, Japan). The end plates for these bipolar plates were made with stainless steel with eight holes for fastening; the fabricated plates were made to withstand a compression pressure of 1 MPa for fuel-cell assembly. The end plates had sheet heaters on the outside of the anode and cathode to control the cell temperature. A stainless-steel current collector with a 1 mm-thick gold plating was inserted between the bipolar plate and end plate on both sides. Ethyleneepropylene diene monomer (EPDM) rubber gaskets (0.6 mm thick, NOK Co., Tokyo, Japan) were used to surround the active area and seal the reactant gases. Bolt torques of 0.3 N m were used to achieve a compression pressure of 1.0 MPa for fuel cell assembly.

Nafion (25 mm thick, NRE211, du Pont de Nemours, Delaware, USA) was chosen as the polymer electrolyte membrane, and carbon-supported platinum (Pt/C, 50 wt% Pt, TEC10E50E, Tanaka K.K., Tokyo, Japan) was selected as the catalyst. The catalyst-coated membrane (CCM) was prepared as follows: Pt/C powder was mixed with a Nafion dispersion (DE2020, du Pont de Nemours, Delaware, USA) using a zirconia bead mill (1 mm diameter beads) for 8 h on a rotation table (400 rpm speed). The catalyst solid contents were prepared using a 1:1 mixture of carbon support and Nafion ionomer. The catalyst was coated on both sides of the membrane with a spray coater (Mic Lab, Kanagawa, Japan) several times until achieving a coating thickness of about 30 mm. The platinum loadings were 0.4 mg cm"2 for both the anode and cathode. The coated membrane was dried at 80 C for 60 min and annealed at 130 C for 10 min to obtain the CCM. The CCM was hot-pressed with MPLs on both sides of the anode and cathode at 130 C and 3 MPa g for 10 min using 200 mm-thick Teflon backing sheets on both sides to avoid MPL attachment to the hand-press plates.

Four flow-channel designs were assessed in this study as shown in Table 4-1 and

Fig. 4-6(a)–(d), (a) Design CNV with conventional grooved flow channel with GDL and CB-MPL, (b) Design CRM-1 with utilizing a straight corrugated mesh on just the cathode which was laid on a pool-shaped graphite bipolar plate that directly covered the CCM with CB-MPL and the anode was the conventional flow field with a GDL, (c) Design CRM-2; with utilizing a straight corrugated mesh for both the anode and cathode with CB-MPL, (d) Design CRM-3; with utilizing a waved corrugated mesh for the anode and straight corrugated mesh for the cathode with CB-MPL.

Furthermore, for Design CRM-3, the effect of MPL conductivity against fuel-cell performance and HFR was evaluated with four different MPLs, namely Design CRM-3a (CB-MPL), Design CRM-3b (GF-MPL), Design CRM-3c (SF-MPL) and Design CRM-3d (SS-MPL). Table 4-2 and Fig. 4-7 shows the configurations of the corresponding fuel cells.

Table 4-1. MEA and flow field configuration of corrugated-mesh fuel cells.

	Flow Field		GDL		MPL	
	Anode	Cathode	Anode	Cathode	Anode	Cathode
Design CNV	Conventional	Conventional	TGP-H-090	TGP-H-090	CB	CB
Design CRM-1	Conventional	Straight corrgated-mesh	TGP-H-090	None	CB	CB
Design CRM-2	Straight corrgated-mesh	Straight corrgated-mesh	None	None	CB	CB
Design CRM-3	Wavy corrgated-mesh	Straight corrgated-mesh	None	None	CB	CB

CB: Carbon black

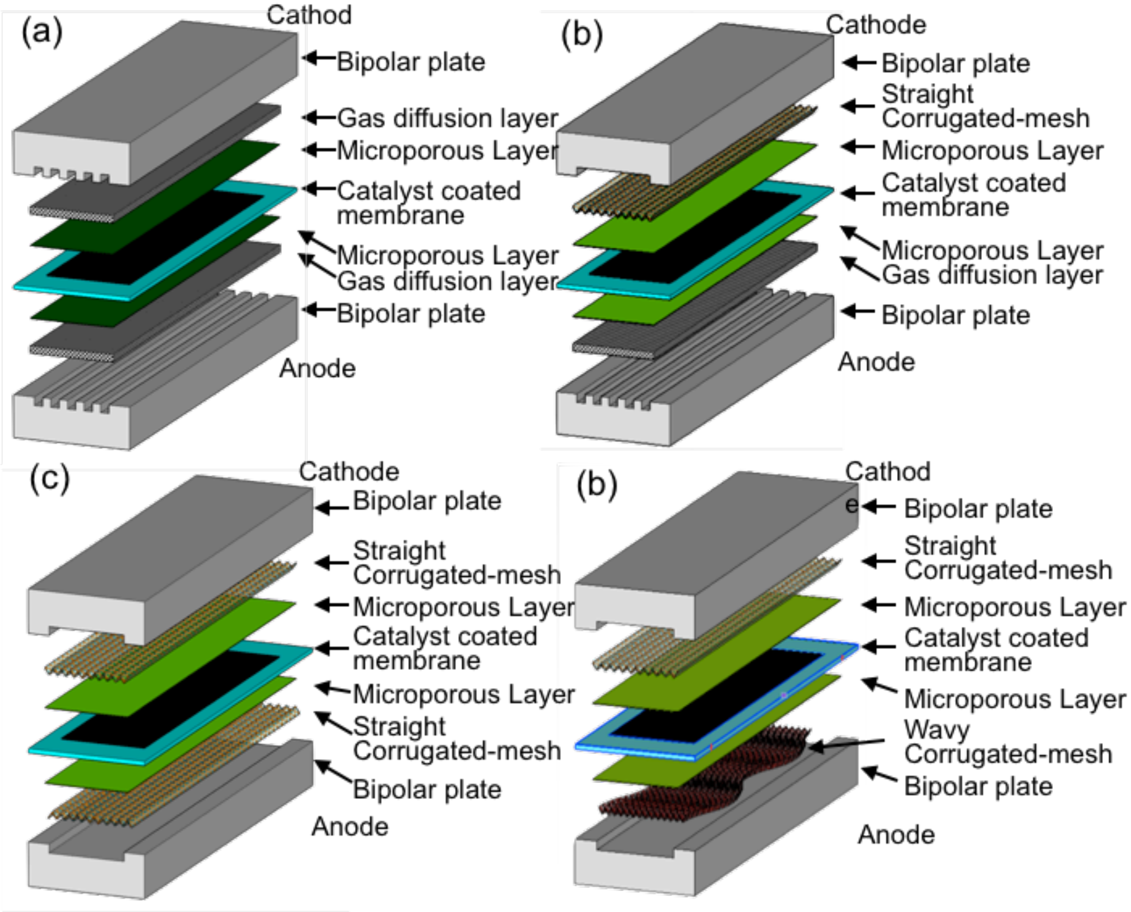

Fig. 4-6. Schematic image of (a) Design CNV: conventional flow field with GDL, (b) Design CRM-1: straight corrugated-mesh flow field for cathode, (c) Design CRM-2: straight corrugated mesh flow field for anode and cathode, and (d) Design CRM-3: wavy corrugated mesh flow field for anode and straight corrugated mesh for cathode.

Table 4-2. MPL materials and MPL's electron conductivities in Designs CRM-3 series.

	MPL material		MPL volume resistivity	
	Anode	Cathode	In-plane	Through-plane
			Ω cm	Ω cm
Design CRM-3a[*1]	CB	CB	2.5×10	1.3×10
Design CRM-3b	GF	GF	4.8	3.9
Design CRM-3c	SF	SF	6.4×10^{-4}	1.9×10^{-4}
Design CRM-3d	SS	SS	1.1×10^{-4}	7.3×10^{-5}

[*1] Design CRM-3a is same as Design CRM-3 in Table 4-1.
CB: carbon black, GF: graphite flake, SF: silver flake, SS: stainless steel

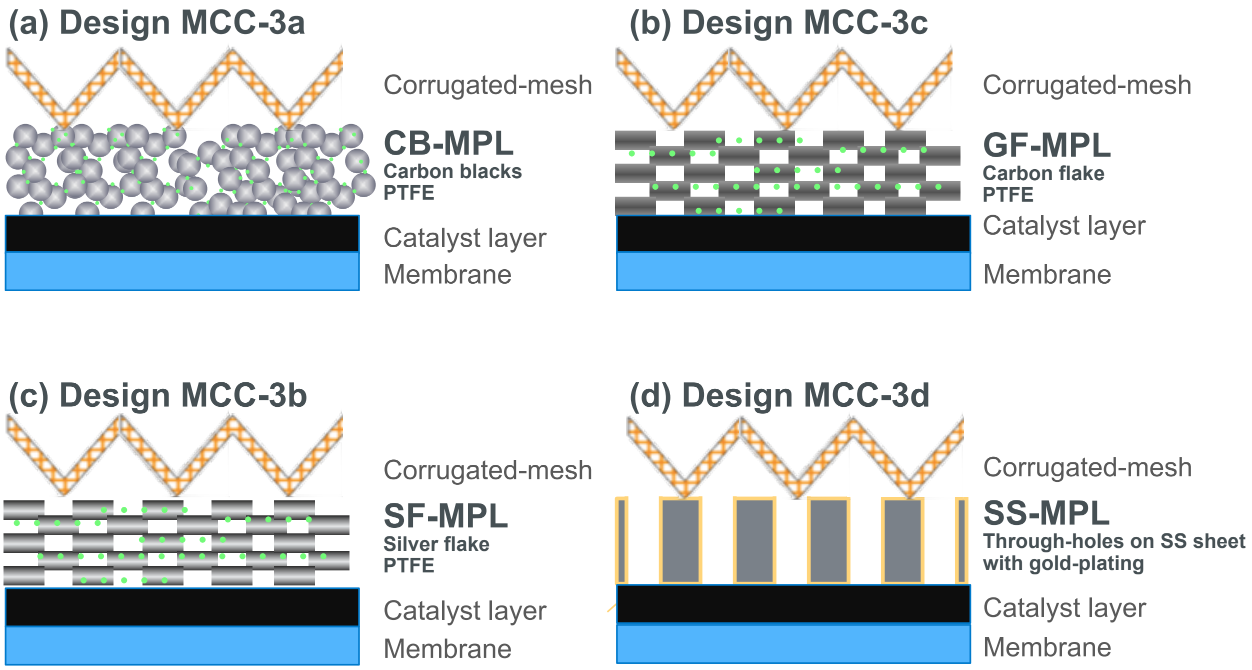

Fig. 4-7. Schematic images of each design for (a) Design MCC-3a (CB-MPL), (b) Design MCC-3b (GF-MPL), (c) Design MCC-3c (SF-MPL), and (d) Design MCC-3d (SS-MPL).

4.3. Characterization of Materials and Fuel Cell Performance

4.3.1. Experimental Test Set-up for Fuel Cell Performance and HFR

The single cell bilt-up method and the fuel cell performance characterization method were same as chapter 3 for microcoil fuel cell. The single cell was mounted on a fuel-cell test stand (Chino Co., Tokyo, Japan) equipped with mass flow controllers, an electronic loading device (Kikusui Electronics Co., Yokohama, Japan) for controlling the electric current, an AC milliohm tester (Model 3566, Tsuruga Electric Co., Osaka, Japan) with a constant HFR of 1 kHz, and a computer for equipment monitoring and data collection as shown in Fig. 3-4.

Gas flows for the anode and cathode were held constant to measure the polarization curves; 0.47 L min^{-1} of pure hydrogen was supplied to the anode (stoichiometry ratio α_{H2}: 9.0 at 1.5 A cm^{-2}), and 1.1 L min^{-1} of air was supplied to the cathode (stoichiometry ratio α_{air}: 9.0 at 1.5 A cm^{-2}). The reactants were supplied with a counter flow as well. All reaction gases were humidified to 100% relative humidity (RH) with temperature-controlled water bubbling tanks. The fuel-cell temperature was maintained at 80 ºC with a heater, and thermocouples were inserted into the cathode bipolar plate. As for the orientation of those fuel cells, the membrane-electrode assemblies (MEAs) were located vertically and the flow channels were set horizontally; consequently, gravity did not assist in the removal of liquid water from the channel.

All power-generation processes were conducted under atmospheric conditions. All fuel-cell evaluations were conducted after 10 h of aging at a current density of 1.0 A cm^{-2}, temperature of 80 ºC, anode feed gas flow of 0.5 L min^{-1} with 100% humidified hydrogen, and cathode feed gas flow of 0.5 L min^{-1} with 100% humidified air.

The present work focuses on electrode flooding; thus, a high air flow rate of 1.1 L min^{-1} and equivalent stoichiometry of 9.0 at 1.5 A cm^{-2} was used for the cathode to minimize the channel flooding effects on voltage loss as same as described in chapter 3. A stoichiometry of 9.0 for a conventional parallel flow channel is generally sufficient to avoid substantial effects attributed to channel flooding. However, for the corrugated-mesh flow channel, the effects of channel flooding and electrode flooding were not separated because of differences in the wettability of the carbon flow field and gold-plated stainless-steel corrugated-mesh, the air average velocity of each flow field, and the electrode interface and gas flow in the conventional flow field with the GDL and in the corrugated-mesh with the MPL. Thus, the equations described above could not be applied in this regard to estimate the effects of channel flooding owing to their limitations in describing geometry and materials. Nonetheless, the same operation condition was used for the corrugated-mesh flow field as for the conventional channel to compare these polarization curves to assess its advantages and disadvantages.

4.3.2. Measurement of Electrical Conductivities of MPLs

For the present fuel cells, the electron-conducting pathway from the catalyst layer to the bipolar plate is thought to be different from conventional fuel cells, and thus is expected to provide different HFRs. For example, an electron in Design CNV is transferred from the catalyst layer through the MPL vertically to the GDL because the GDL uniformly covers the entire active area. In Designs CRM 1-3 without GDLs, electrons in the catalyst layer are first transferred vertically to the MPL and then move horizontally within the MPL to the contact point of the corrugated mesh. To characterize this, the electronic conductivity of MPL in the in-plane and through-plane directions was measured.

Fig. 4-8 shows the images for the measurement of the in-plane and through-plane resistivity. The measurement of the in-plane resistivity was conducted at 25 C following ASTM standard C611, using four-point detectors in a direct current [5]. 0.5 cm x 4.0 cm sample strips of the MPL and GDL were used. Resistances obtained with a resistance meter (1750 LCR Dig-Bridge with Kelvin clip leads, Quad Tech Inc., Maynard, USA) were converted to resistivity using the sample geometries. The measurement of the through-plane resistivity was conducted at 25 C in accordance with the method described in Ref. [6]. A 20 mm round sample was placed on a load cell (ElectroPuls^{TM} E1000, Instron, Massachusetts, USA) between two gold-plated pedestals, and the sample was subjected to a compression pressure of 1 MPa. The same resistance meter as above was used to obtain the resistance of the sample. After the compression stress stabilized (30-60 min), the resistance was measured and converted to resistivity using the sample geometry.

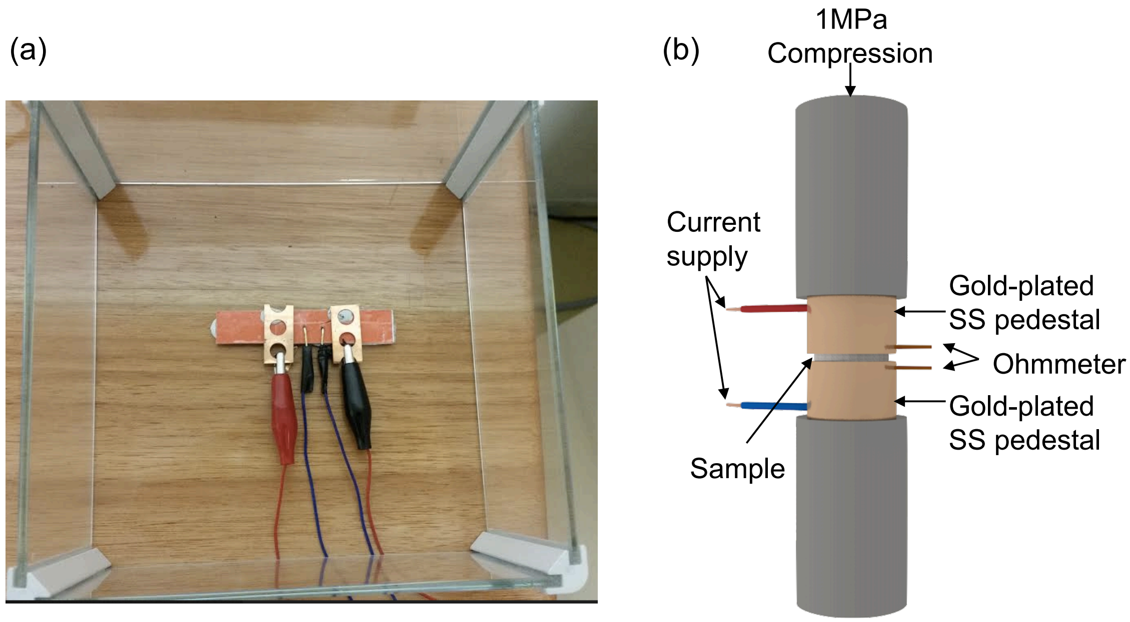

Fig. 4-8. Images for resistivity measurement, (a) in-plane resistivity and (b) through-plane resistivity.

4.4. Results and Discussion

4.4.1. Polarization Curve

Fig. 4-9 shows the polarization curves for Design CNV (conventional flow field), Design CRM-1 (straight corrugated mesh on cathode), Design CRM-2 (straight corrugated mesh on anode and cathode) and Design CRM-3 (wavy corrugated mesh on anode and straight corrugated mesh on cathode) as described in Table 4-1 and Fig. 4-6. Fig. 4-10 shows the HFR for all Designs at 1 kHz, and Fig. 4-11 shows the IR-corrected polarization curves for all four Designs. The IR corrections were performed to compensate for the ohmic loss for each design using HFR; Fig. 4-11 shows both the activation loss and mass-transfer loss (flooding) [7].

As seen in Fig. 4-11, all four IR-corrected polarization curves are nearly the same for the lowest current density up to 0.3 A cm^{-2}. This observation indicates that the activation loss for each design is the same, that the gas is equally supplied to the catalyst in each design, and that the CCMs and MPLs have similar properties. In addition, the HFR may represent the ohmic resistance even though the electron pathways are different for Design CNV and Design CRM-1, CRM-2, CRM-3 as indicated by the similar IR-corrected polarization curves. For Design CNV, the cell voltage gradually decreases due to flooding as the current density exceeds 0.5 A cm^{-2} (Fig. 4-11) with a rapid voltage drop down to 0.3 V at 1.7 A cm^{-2}. In contrast, Design CRM-1, CRM-2, CRM-3 utilizing corrugated mesh `exhibits performances without significant voltage drops caused by electrode flooding.

I.S. Hussaini and C.Y. Wang have recently characterized water and air permeabilities of GDLs [8], showing that the air relative permeability decreases rapidly with increasing water saturation. The gas can travel through the GDL through a capillary fingering network of liquid water [9]. Presently, it is not certain whether water saturation occurred during the operation of all Designs, but according to the rough estimation of temperature in the GDL described in a previous section 5.1.4, the temperatures of the GDL and MPL could be estimated as 82–83 °C against an operation temperature of 80 °C. Thus, these temperatures indicate that liquid water might be present in the GDL and MPL. Designs CRM-1, CRM-2, and CRM-3 exhibit performances with both reduced flooding and voltage drops, even in the presence of liquid water. These performances have been discussed in the previous section 5.1.1; it is suggested that microcoils provide a uniform gas supply onto the catalyst layer, even in the presence of liquid water, and that flooding occurs only for a specific combination of land/channel structure and GDL, where the liquid water accumulates under the land regions of the cathode. In Designs CRM-1, CRM-2, and CRM-3, the corrugated mesh appears to supply the gas uniformly to the active area in a similar fashion as the microcoils.

In addition to providing a uniform gas supply with the corrugated mesh, the GDL-less design efficiently supplies gas to the catalyst layer. Specifically, the water on the top surface of the MPL can be easily removed by dynamic gas flow through the corrugated mesh and thus, the amount of liquid water in the MPL is kept at a sufficiently low saturation level to allow wider gas diffusion. Furthermore, because the diffusion length in the MPL is smaller than in the GDL and MPL, the gas diffuses noticeably faster in the GDL-less designs than the conventional design with GDL. In addition, a comparison of Designs CRM-2 and CRM-3 reveals that only the cathode flow field exhibits an effect on electrode flooding, as the three designs with corrugated mesh on the cathode display similar behaviors (Fig. 4-11), regardless of the conventional flow field or corrugated mesh flow channel utilized on the anode.

Fortunately, the high stoichiometry used ($\alpha_c = 9.0$) could minimize the effect of channel flooding, even with the hydrophilic and rough surface of the corrugated mesh flow channels. As reported by Lu et al., channel surface wettability can strongly affect channel flooding [10]. The researchers observed two-phase flows in a flow channel of 0.7 mm width and 0.4 mm depth on uncoated, hydrophilic-, and hydrophobic-coated Lexan plates. They found that at a high liquid-water flow, which is equivalent to a current density of 1.0 A cm^{-2}, the hydrophilic channel shows a greater flow fluctuation than that of the uncoated and hydrophobic channels; this is thought to be because water can wick into the channel corners and is removed through continuous film flow at a higher rate than that driven by the air flow. In addition, water tends to adhere to the channel wall with high surface tension instead of being removed by air shearing. Furthermore, they also found that the flow fluctuation decreases as air velocity increases, and that flow fluctuation becomes less than 50% at a flow velocity of 5 m s^{-1} in their case. In the present case utilizing the corrugated mesh flow channel, the metal mesh is most likely hydrophilic and rough, and the cross-section dimension of the corrugated mesh is 0.3 mm wide and 0.3 mm deep. The water probably tends to be present as a continuous film on the corrugated mesh surface. However, the average gas velocity at this flow rate is observed to be 6.7 m s^{-1}, which seems to be a high enough value for uniform distribution in the corrugated mesh channel of the cathode (Fig. 4-11). Therefore, channel flooding might not have a strong effect on the performances of Designs CRM-1, CRM-2, and CRM-3.

The through-plane water transport from the electrode to the channel can also be strongly influenced by surface wettability of the channels. The metal mesh can be hydrophilic while the GDL is hydrophobic; thus, the behavior of the liquid water from the MPL to the corrugated mesh and GDL should be different with different surface wettability. Consequently, this may alter the liquid water behavior, which can impact current density. A. Turhan et al. investigated the effects of channel-wall wettability of gold-plated and PTFE-coated flow channels using neutron radiography to detect the liquid water in the channel, GDL, MPL, and catalyst layer in the fuel cell [11]. They suggested that the hydrophilic interface enhances capillary suction from the GDL, as does the hydrophilic wall in the form of film flow, and results in less water storage in the GDL and MPL. Another study by Wang describes fuel-cell performance as a function of wettability of an entirely hydrophilic GDL and super-hydrophobic/hydrophilic/super-hydrophobic GDL sandwich [12]. The hydrophilic GDL lowers the performance because the liquid water could quickly distribute in the GDL; however, the droplet resists being detached from the GDL surface by air shearing due to the high surface tension, resulting in a reduced gas permeability as a consequence of this thin water film.

These two cases indicate that the hydrophilic wall of flow channel or the hydrophilic GDL can pull the liquid water from the next layer by capillary force and that the liquid water tends to form a thin film on the air-flow interface of the flow channel and the GDL. If the airflow velocity is not sufficiently high to remove the liquid water on the hydrophilic surface, the water can flood the channel or GDL surface. In the present case, the hydrophilic metal mesh channel on the MPL may enhance liquid-water transport from the MPL to the channel, allowing a water film to be formed on the metal mesh. With respect to channel flooding, a high stoichiometry could help to remove the water as described in a previous paragraph in this section. Furthermore, unlike the case of the hydrophilic GDL, the present system utilizes a hydrophobic MPL at the air interface; thus, a water film could not form on the hydrophobic MPL surface, and gas could likely be supplied into the MPL without liquid water blocking the process. Further studies are required for this fuel cell in terms of complete characterization and investigation of the effects of corrugated mesh on the MPL and operation conditions, as well for more detailed and accurate mechanistic studies of water transport.

Although Designs CRM-1, CRM-2, and CRM-3 exhibit less flooding, their performances are slightly different because of the different HFR values for these designs along with varying flow channel patterns on the anode and cathode; HFR performances are discussed in the next section (Section 4.3.2).

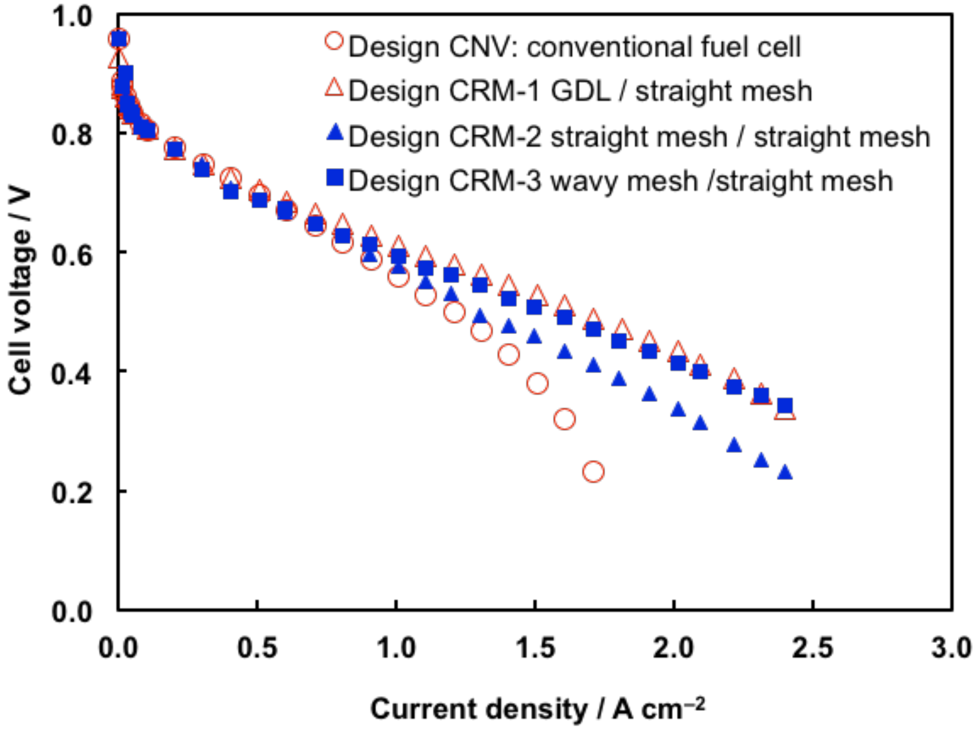

Fig. 4-9. Polarization curves for (a) Design CNV: conventional fuel cell with GDL, (b) Design CRM-1 (straight corrugated-mesh flow field for cathode), (c) Design CRM-2 (straight corrugated mesh flow field for anode and cathode), and (d) Design CRM-3 (wavy corrugated mesh flow field for anode and straight corrugated mesh for cathode), obtained under RH_{anode} =100%, $RH_{cathode}$ = 100%, ambient pressure at the outlets, cell temperature = 70 °C, and hydrogen and air supplied in a stoichiometric ratio of 9.0 at 1.5 A cm^{-2}.

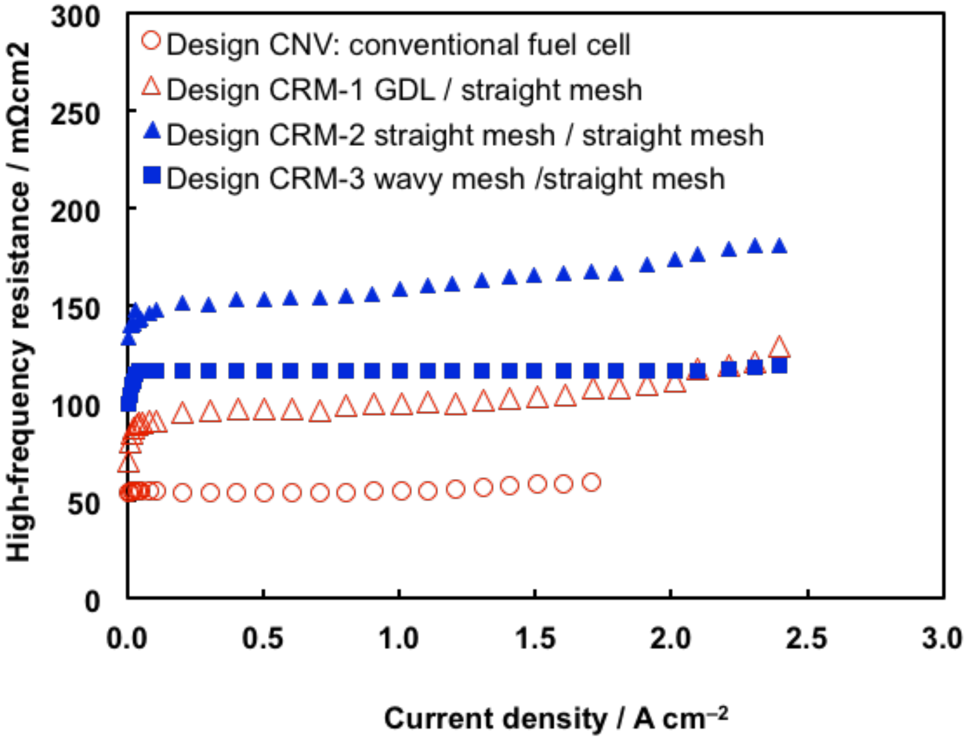

Fig. 4-10. High-frequency resistance (HFR) for Designs CNV, CRM-1–3.

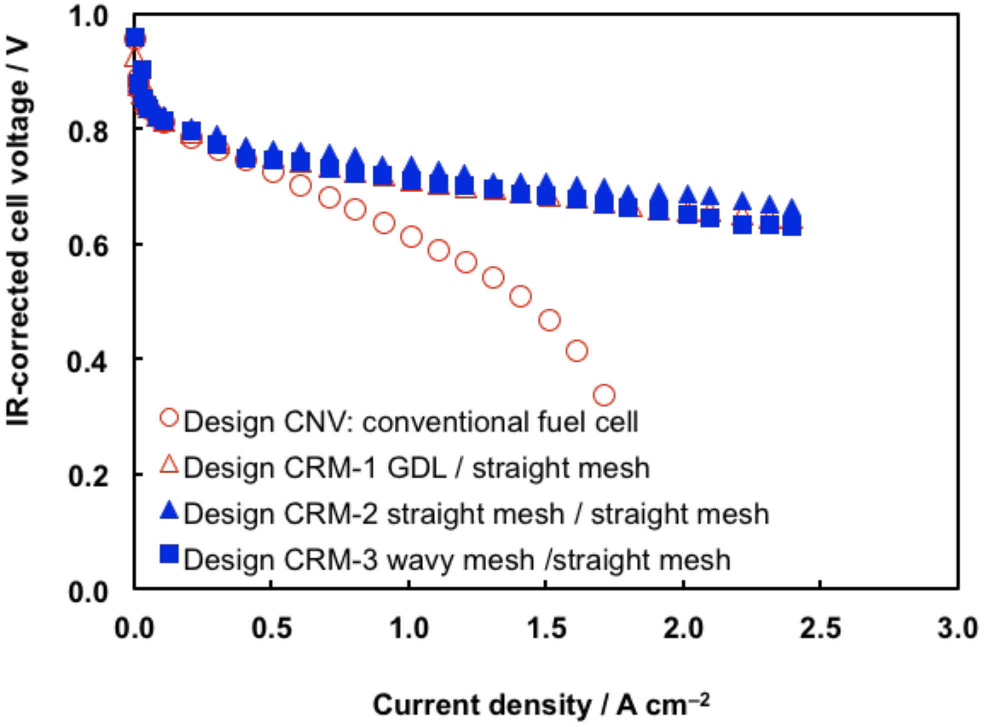

Fig. 4-11. IR-corrected polarization curves for Designs CNV, CRM-1–3.

4.4.2 Effect of Flow-Channel Pattern

Fig. 4-10 shows the HFR for all Designs. Design CNV utilizes the conventional flow field, and GDLs on both the anode and cathode exhibit an HFR of 55–60 mΩ cm^2, in agreement with the values published in the literature (50–70 mΩ cm^2) [13–15]. Design CRM-1, which uses a corrugated mesh directly on the MPL on the cathode, has an HFR of 90 mΩ cm^2, and Designs CRM-2 and CRM-3, which use corrugated mesh at both the anode and cathode, have HFR values of 150 mΩ cm^2 and 120 mΩ cm^2 respectively. These GDL-less designs (Designs CRM-1, CRM-2 and CRM-3) exhibit a relatively higher HFR than that of conventional Design CNV. As discussed in a previous section 5.1.3, these results indicate that the electron pathways for these designs are different. In Design CNV, the pathway could be vertical from the MPL/catalyst layer to the GDL because the GDL makes surface-to-surface contact with the entire MPL. However, in Designs CRM-1, CRM-2, and CRM-3, the pathway could be the combination of both vertical and horizontal directions: vertical from the catalyst layer to the MPL and horizontal from the MPL to the contact point of the corrugated mesh as shown in Fig. 4-12(a)–(b). This is because the corrugated mesh does not cover the entire active area and can make line-to-surface contact with the MPL.

Note that the corrugated mesh has contacts on the MPL at intervals in the corrugation cycle, meaning that the corrugated mesh has fewer contact points with the MPL, and furthermore, the corrugation peak line is made of a number of twill-woven fibers, and the contact line is the aggregate of contact points. In this paper, the term “line” is used for the aggregate contact points of the fibers.

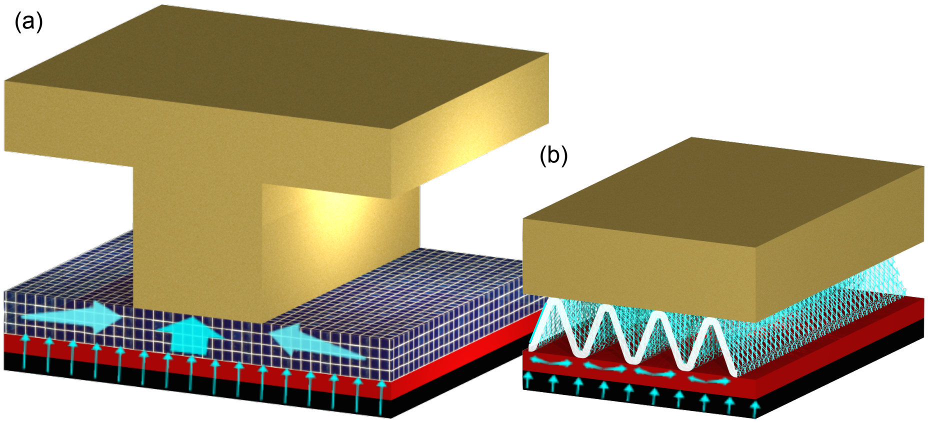

Fig. 4-12. Electron pathway from catalyst layer to bipolar-plate for (a) Design CNV and (b) Design CRM-1 ~ Design CRM-3.

.

Let the resistance of CCM be R_{CCM}, the resistance of GDL/MPL be R_{GDL}, and the resistance of corrugated mesh/MPL be R_{mesh}. The overall resistance for Design CNV is described as follows:

$$R_{\mathrm{GDL}} + R_{\mathrm{CCM}} + R_{\mathrm{GDL}} = 55\ \mathrm{m\Omega\ cm^2} \tag{4-1}$$

The overall resistance for Design CRM-1 is described as:

$$R_{\mathrm{GDL}} + R_{\mathrm{CCM}} + R_{\mathrm{mesh}} = 90\ \mathrm{m\Omega\ cm^2} \tag{4-2}$$

These overall resistances contain the material and contact resistance in the designs along with the electron pathway. From Eqs. (1) and (2), the overall resistance for Design CRM-

2 should be:

$$R_{\text{mesh}} + R_{\text{CCM}} + R_{\text{mesh}} = 125\ \text{m}\Omega\ \text{cm}^2 \tag{4-3}$$

However, Fig. 4-10 shows that the HFR for Design CRM-2 is 150 mΩ cm^2, which is bigger than the estimated value of 125 mΩ cm^2 as determined from (4-3). This indicates that another factor might affect the experimental resistance, creating a higher HFR than expected.

Design CRM-3 utilizes the straight pattern as the flow channel on corrugated meshes (straight corrugated mesh) for the anode and cathode as shown in Fig. 4-6 (c). In this case, the corrugation line of the straight pattern on both sides of the MPL/CCM/MPL might not meet at the same contact line because of engineering and alignment tolerances. These unaligned line-to-line sandwiches should reduce the vertical compressive contact pressure and increase the shear stress between the MPL and corrugated mesh. In Design CRM-2, this low-contact pressure increases the contact resistance between the interfaces and HFR. On the other hand, the corrugated mesh and GDL in Design CRM-1 could make line-to-surface sandwiches, and the contact point could experience a vertical contact pressure, resulting in a better contact between the MPL and corrugated mesh even with these tolerances.

A wavy pattern as a flow channel was fabricated on corrugated meshes with the same triangular cross-section (wavy corrugated mesh) as described in Section 4.2.1. The wavy corrugated mesh was laid on the anode and the straight corrugated mesh was laid on the cathode (Design CRM-3) as shown in Fig. 4-6 (d). Utilizing the wavy flow channel at the anode is a reasonable arrangement because the anode needs a low flow rate and hydrogen has a low viscosity; accordingly, the pressure drop at the anode should be even lower with a tortuous flow channel. However, these pressure-drop requirements are dependent on the application for which the fuel cell is fabricated.

In Design CRM-3, the straight corrugation line at the anode and the wavy corrugation line at the cathode must meet to make crossline sandwiches through the MPL/CCM/MPL. As seen in Fig. 4-10, Design CRM-3 has a lower HFR than Design CRM-2, indicating that the crossline-to-crossline sandwiches could make better contacts with increased compressive pressure on the MPL. The HFR value of 120 mΩ cm^2 for Design CRM-3 roughly agrees with the estimated value of 125 mΩ cm^2 as determined by Eq. (4-3).

Although Eq. (4-3) could be generated from Eqs. (4-1) and (4-2), Eq. (4-1) is based on the surface-to-surface sandwich of Design CNV, while Eq. (4-2) is based on the surface-to-line sandwich. Therefore, Eq. (4-3) should not be able to explain the crossline sandwich precisely. The overall resistances R_{mesh}, R_{GDL}, and R_{CCM} in Eqs. (4-1)–(4-3) contain contact resistance, but the contact resistance should differ in the sandwich configurations. To estimate the HFR for each design, including the effects of contact pressure and contact resistance as well as conductivities of the materials, current efforts in our lab are being dedicated to simulating the resistance via a 3D finite element model (FEM) and will be reported elsewhere.

Even with the superior contact in Design CRM-3, the HFR is still higher than in

Design CNV. As described previously, the higher HFR should be derived from the longer electron-pathway running horizontally through the MPL. Therefore, several MPLs with different conductivities in Design CRM-3 were evaluated.

4.4.3 Effect of MPL Conductivity for Polarization Curve

Using Design CRM-3, the effect of MPL conductivity on the HFR was evaluated utilizing the wavy corrugated mesh at the anode and the straight corrugated mesh at the cathode. Design CRM-3 utilizes CB-MPL and will be denoted as Design CRM-3a, GF-MPL as Design CRM-3b, SF-MPL as Design CRM-3c, and SS-MPL as Design CRM-3d as shown in Fig. 4-7. Table 4-2 also shows the MPL material for each design and the in-plane and through-plane volume resistivity (conductivity^{-1}) for each MPL. There was some concern that silver might not be durable enough for extended use in the fuel cell; a silver-flake MPL was used in evaluations on the basis of the results described by Ge et al., who used a silver mesh as the cathode GDL for cathode catalyst layer observations in their work [16]. Their results did not seem to suffer from silver corrosion in the short-term evaluation. It should be noted that silver is not the final material, and another durable and conductive material must be identified for use in MPLs in the future.

Fig. 4-13 shows the polarization curves for Designs CRM-3a–d. Fig. 4-14 and Fig. 4-15 show the HFR and IR-corrected polarization curves, respectively, for Designs CRM-3a–3d. As seen in Fig. 4-15, all four IR-corrected polarization curves are nearly the same for the lowest current density up to 0.3 A cm^{-2}; these observations indicate that the activation loss for each design is the same, that the gas is equally supplied to the catalyst in each design, and that the CCMs and MPLs have similar properties.

As shown in Fig. 4-13, Designs CRM-3b and CRM-3c have a similar behavior up to a current density of 3.0 A cm^{-2} without significant flooding, even when utilizing different MPL materials and shapes. Although the MPLs in Designs CRM-3b and CRM-3c were made with flake powders in a layered structure, these flake-powder MPLs are shown to supply enough gas, even with a diffusion pathway differing from that for the carbon black MPL in Design CRM-3a, at least under a high stoichiometry (9.0) at 1.5 A cm^{-2} with a fully humidified anode and cathode gas supply. Certainly the performances for Designs CRM-3a and CRM-3c show less flooding, but such a high stoichiometry is not practical to assess the advantages of each MPL prepared with different materials and possessing different pore structures, especially for flooding evaluations.

To the best of our knowledge, no research paper has been published describing the effects of flake-shaped MPL particles on fuel-cell performances. Many papers, however, have reported that gas diffusivity in the MPL is based on porosity, pore-size, and tortuosity; furthermore, connectivity, hydrophobicity, and thermal/electrical conductivity in combination with the above three properties can result in differing liquid-water saturation, distribution, and morphology formed by capillary and temperature-driven flows in the GDL and MPL. Moreover, changes in liquid-water surface film formation, which can reduce gas diffusivity and cause cathodic flooding, can also result from changes in these material characteristics [17–20]. Finally, these MPL properties may also affect the net water transport across the membrane, which can cause membrane dry-out or GDL flooding [21–22]. Specifically, as reported by Morgan et al. [22], the particle size (5, 17, and 55 μm) of MPLs can affect fuel-cell performance; the researchers found the performance of a 17 μm particle to be superior among the three particles tested in terms of balancing membrane dry-out and GDL flooding under dry and wet conditions. This result suggests that a particle size in the micron range should be carefully considered with respect to fuel-cell performance, especially for limitations in current density mainly determined by flooding behaviors. In the present case, the flow-field structure without a GDL is quite different, and the flake-shaped MPL particle can form different layered pore structures. Thus, the conclusions of Morgan et al. cannot simply be applied for the present case. The GF particle has a diameter of 9 μm and thickness of 1 μm, and SF has a diameter of 9 μm and thickness of 1 μm; these materials are therefore likely to form similar pore structure in the MPL. In addition, both of the MPLs have the same PTFE content, suggesting that the hydrophobicity of these MPLs is probably similar. Therefore, water transport by the capillary-driven flow through GF-MPL and SF-MPL in the present fuel-cell operation is thought to be similar and the flooding behavior in the fuel cell utilizing those MPLs in Fig. 4-7 is also thought to be similar so that the differences in these performances might derive dominantly from the electron resistance of the MPLs, as will be discussed later in this section.

It is important to note that even if the capillary-driven water flow in these MPLs may be similar, their thermal and electric conductivities, overall heat transfer, and ohmic heat generation are different; thus, these properties can generate different temperature distributions and provide different temperature-driven water flows, which can give rise to different flooding behaviors in the fuel cells. The advantages of flooding control in the flake-shaped and nano-sized particles in the MPLs were not assessed because of the lack of mass-transport properties of the flake-shaped particle; further studies are therefore required for the characterization and investigation of structural and material effects of the MPL components. In addition, an examination of varying operating conditions on these fuel cells is required, especially for those with moderate air stoichiometry.

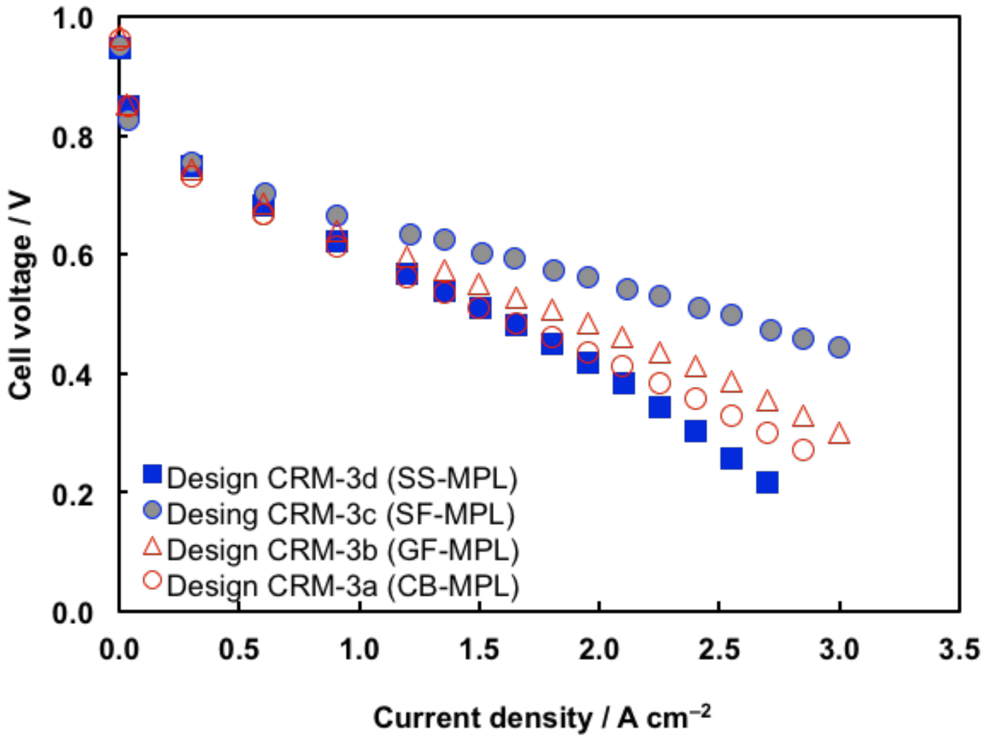

Fig. 4-13. Polarization curves for Design CRM-3 with four different MPL; Design CRM-3a (CB-MPL same as CRM-3 in Fig. 4-9), CRM-3b (GF-MPL), CRM-3c (SF-MPL), and CRM-3d (SS-MPL), obtained under RH_{anode} =100%, $RH_{cathode}$ = 100%, ambient pressure at the outlets, cell temperature = 70 °C, and hydrogen and air supplied in a stoichiometric ratio of 9.0 at 1.5 A cm^{-2}.

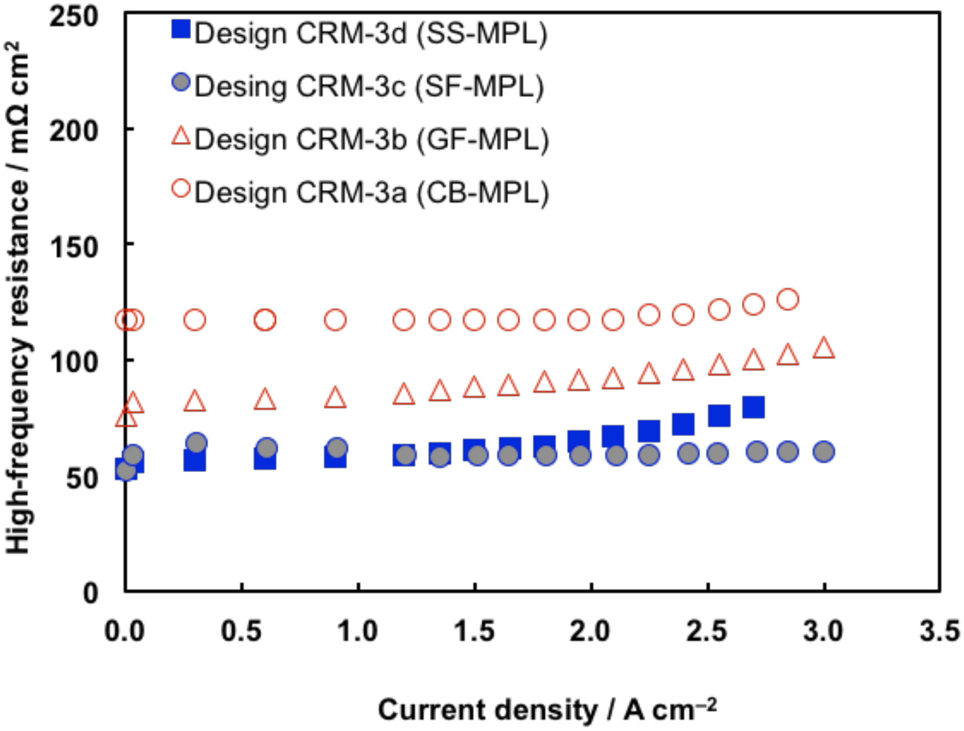

Fig. 4-14. High-frequency resistance (HFR) for Designs CRM-3a–3d.

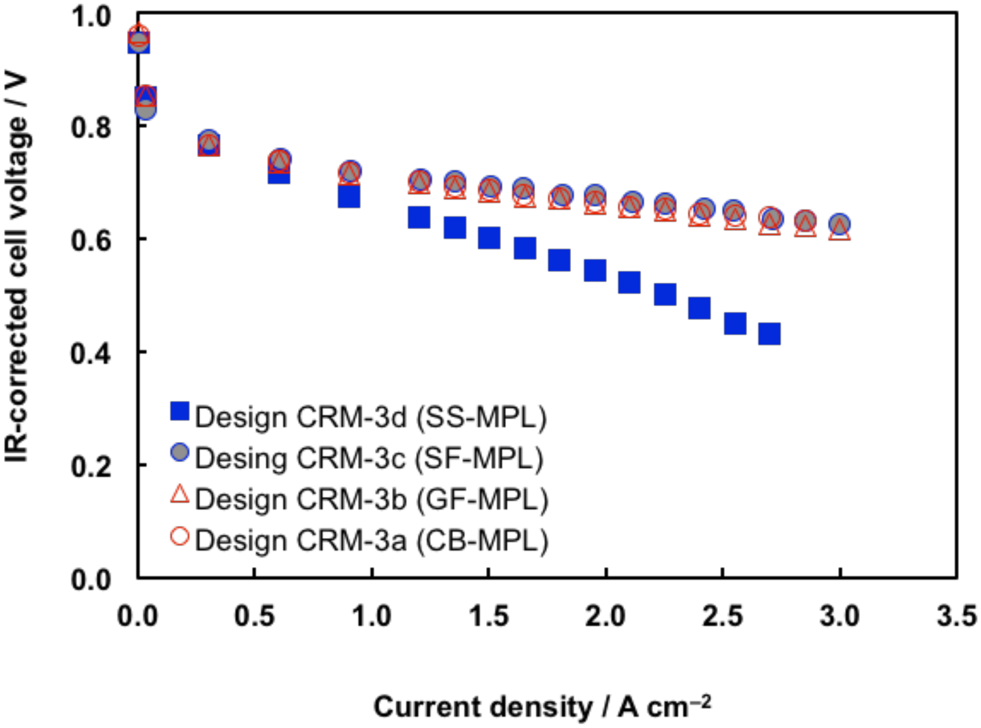

Fig. 4-15. IR-corrected polarization curves for Designs CRM-3a–3d.

4.4.4 Effect of MPL Conductivity for HFR

As shown in Fig. 4-14, the HFR for Designs CRM-3a–3d are 120, 85, 65, and 57 mΩ cm^2, respectively. The HFR order of Design CRM-3d < Design CRM-3c < Design CRM-3b < Design CRM-3a mimics the conductivity of the MPL where SS < SF < GF < CB. Therefore, the MPL conductivity appears to have an effect on the HFR for each design. A frequency of 1 kHz was applied with an AC milliohm tester in the HFR measurement, which could detect the ohmic resistance of the electrolyte membrane, catalyst layer, MPL, and external parts (corrugated mesh, end plate, current collector, and wire/connector) as well as the contact resistance between each layer interface [23–25]. The resistance of these external parts can be neglected because they are made of gold-plated metal. Furthermore, the resistance of the electrolyte membrane and catalyst layer should be the same for each design, especially at the lower current density, because each design utilizes the same membrane and catalyst layers and operates under fully humidified conditions [26]. Therefore, the HFR difference between each design is derived from the conductivity differences of the MPLs.

An equivalent electrical circuit model was created to calculate the MPL resistance contribution of the HFR for each design. In Fig. 4-16, the two-dimensional model with in-plane and through-plane resistance represents the electron resistance in the MPL from the catalyst layer to the contact point of the corrugated mesh on the MPL. The combined resistance is calculated in this circuit model under the following assumptions:

(1) The MPLs at the anode and cathode have the same resistance. One side is considered

in the model and the resistance is doubled for both sides.

(2) The half pitch of the contact point of the corrugated mesh is considered symmetrical.

(3) The catalyst layer has the same potential throughout the layer.

(4) The MPL has anisotropic conductivity for the in-plane and through-plane directions.

(5) The contact resistance between the catalyst layer and MPL and between the MPL and corrugated mesh can be ignored.

(6) The in-plane electron conduction in the catalyst layer is also ignored.

As shown in Fig. 4-16(b), the model is divided into *N* units (Units 1–*N*) and each unit has in-plane resistance R_0 and through-plane resistance R_1. In Unit 1, the combined resistance Rc_1 is described as follows:

$$Rc_1 = \frac{1}{\frac{1}{R_0 + R_1} + \frac{1}{R_0}} \tag{4-4}$$

Then, in Units 1 and 2, the combined resistance Rc_2 is described with Rc_1 as follows:

$$Rc_2 = \frac{1}{\frac{1}{Rc_1 + R_1} + \frac{1}{R_0}} \tag{4-5}$$

Finally, in all Units 1–*N*, the combined resistance Rc_N is described with Rc_1 as follows:

$$Rc_N = \frac{1}{\frac{1}{Rc_{N-1} + R_1} + \frac{1}{R_0}} \tag{4-6}$$

The conductivity of each MPL shown in Table 4-2 is used for the calculations with Eqs. (4)–(6), and the dimensional information (MPL thickness, contact-point interval, and active area) is also used to normalize the resistance to area resistivity (resistance per unit active area). Fig. 4-17 shows the plot of the estimated area resistivity of MPL for Designs CRM-3a–3d against the experimental HFR at 0.1 A cm^{-2} in the fuel-cell evaluation. The estimated MPL area resistivity and HFR appear to have a good correlation, where the MPL area resistivity linearly contributes to the total HFR in the fuel cell. Designs CRM-3c (SF-MPL) and 3d (SS-MPL) have similar conductivities of 6.4×10^{-4} and 1.1×10^{-4} Ω cm, respectively, and similar estimated resistances of 6.0×10^{-4} and 2.2×10^{-4} mΩ cm^2, respectively. Each design has different HFRs (62 mΩ cm^2 and 55 mΩ cm^2, respectively) than would be expected from similar conductivities and estimated area resistivities.

As described in assumption (5) above, the contact resistance between the MPL and catalyst layer is ignored in this model, but SF-MPL and SS-MPL might have quite different contact resistances between the catalyst layer and MPL. The contact resistance is strongly dependent on the contact pressure [27]. In the present design, compression pressure is added onto the MPL from the corrugation line on the corrugated mesh, and the compression pressure is distributed via the MPL onto the catalyst layer. Generally, the uniformity of pressure distribution depends on the rigidity of the substrate [28]. SS-MPL, which is made of stainless-steel foil, is more rigid than SF-MPL, which is made of silver-flake powder bonded with PTFE. Thus, SS-MPL distributes the stacking pressure onto the catalyst layer more uniformly than SF-MPL, and SS-MPL makes better contact with the catalyst layer. Therefore, Design CRM-3d utilizing SS-MPL has a lower contact resistance between the catalyst layer and MPL than Design CRM-3c with SF-MPL. This might be the reason why Design CRM-3c and 4d show different HFRs even with the similar conductivities of their respective MPLs as shown in Fig. 4-18.

The contact resistance between the catalyst layer and MPL is also dependent on the material, contact area of contact point, and surface properties [29–30] as well as contact pressure distribution. Therefore, the contact resistance between the corrugated mesh and MPL depends on the number of contact points and spot areas of single contact points, especially in point-to-surface contacts [31] in addition to the electron pathway distance. As described in Section 3.3.3, the contact between the MPL and corrugated mesh is formed not by the actual line contact but by the aggregate of contact points in the corrugation line, which might need to be considered in the point-to-surface contact case.

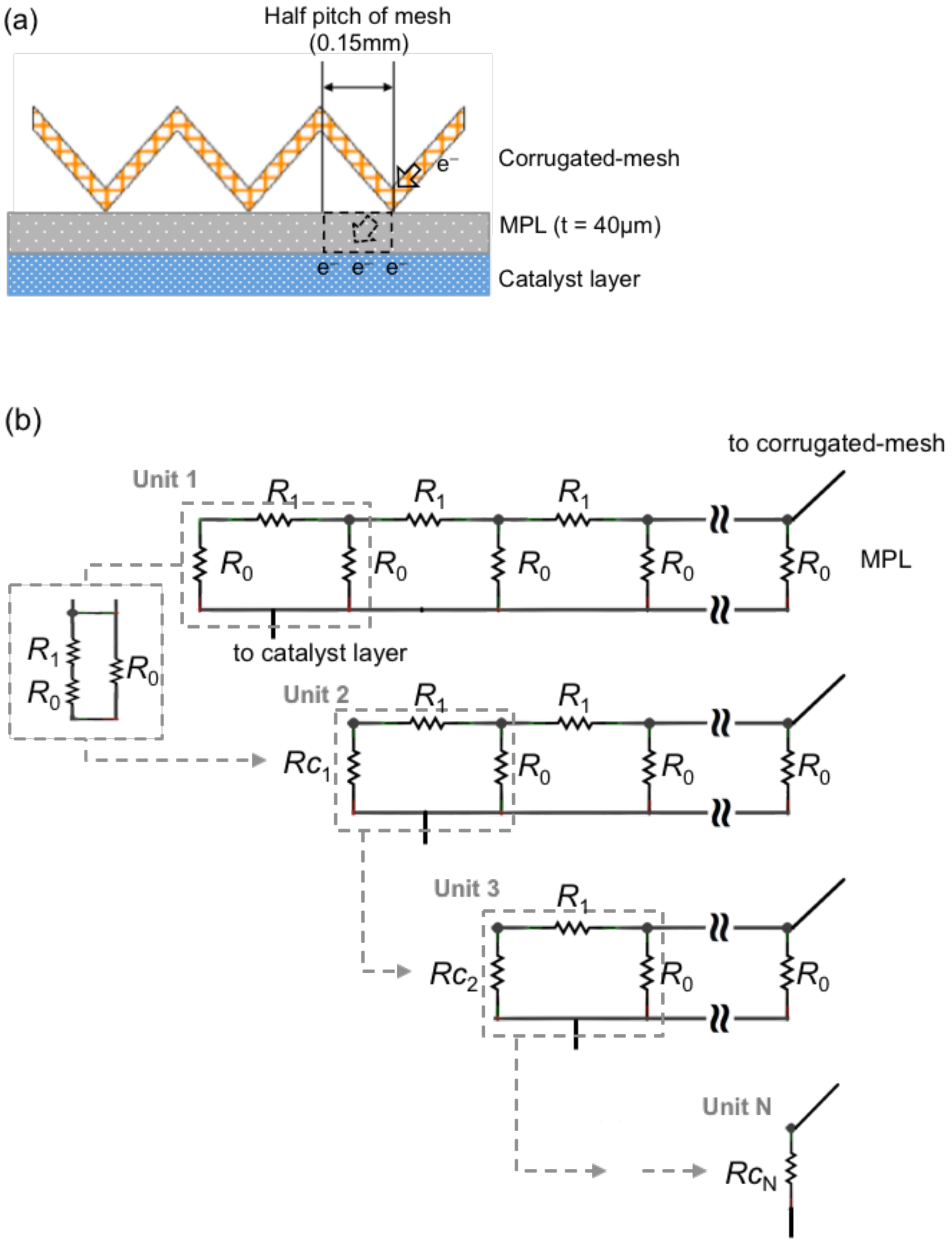

Fig. 4-16. Scheme of the catalyst layer, MPL, and corrugated mesh for electron conduction. (a) The sketch of the MPL, used for the construction of the continuous model. (b) The one-dimensional transmission line equivalent circuit for the MPL, where the elementary unit with through-plane electron resistivity R_0 and in-plane electron resistivity R_1.

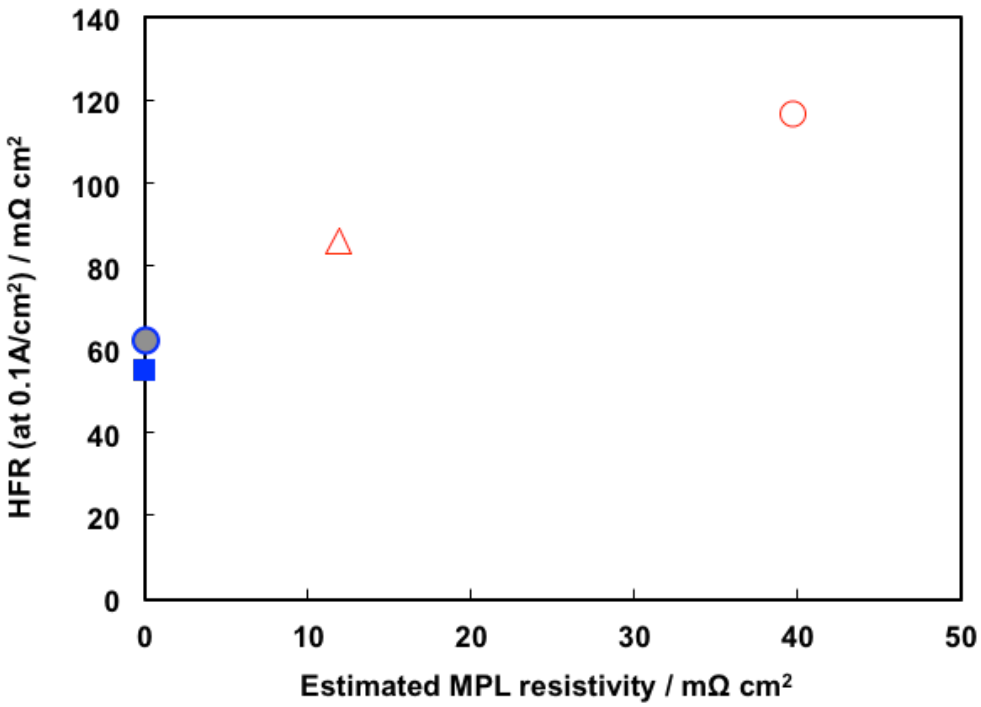

Fig. 4-17. A plot of the estimated area resistivity of MPL for Designs CRM-3a–3c against the experimental HFR at 0.1 A cm^{-2}.

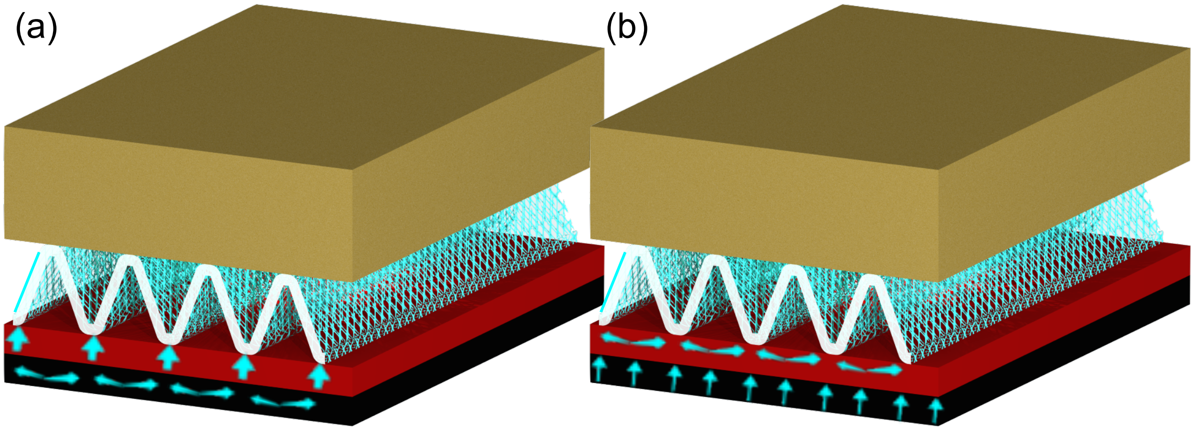

Fig. 4-18. Schematic image for electron pathway for (a) SF-MPL an (b) SS-MPL. Black layer is catalyst layer, red layer is MPL, and top layer is bipolar-plate, respectively.

4.4.5 Supplementary Performance at Low Stoichiometry

Fig. 4-19 shows a polarization curve and HFR for a lower stoichiometry of 3 for Design CRM-3c using SF-MPL as an examination of performance under practical operation conditions. Constant flow rates of 0.16 and 0.37 L min^{-1} were employed at the anode and cathode, respectively, during the operation, which is equivalent to a stoichiometry of 3.0 at 1.5 A cm^{-2}. Other operation conditions were set the same as that indicated in Fig. 4-13. As shown in Fig. 4-19, the HFR is similar as that for a stoichiometry of 9.0 (Fig. 4-13). The performance begins to drop at a current density of about 2.0 A cm^{-2}, suggesting that flooding could affect mass transfer somewhere in the fuel cell; however, it is unclear from the one polarization curve exactly where the flooding occurs. It is suggested that the lower average air velocity in the cathode channel (2.3 m s^{-1}) might not be able to remove water from the surface of the corrugated mesh or the MPL, which would cause channel flooding. Further study is also required for a better understanding of the effects of stoichiometry dependency. In contrast to Design CRM-3c, Design CRM-3d shows flooding. This might be caused by the decreased diffusivity of the SS-MPL, where the reactant gas could not diffuse in the in-plane direction, but instead might diffuse in the catalyst layer from the through-holes. In addition, the flooding performance might be caused by the facile accumulation of water on the hydrophilic surface of the gold-plated layer on the SS-MPL [4].

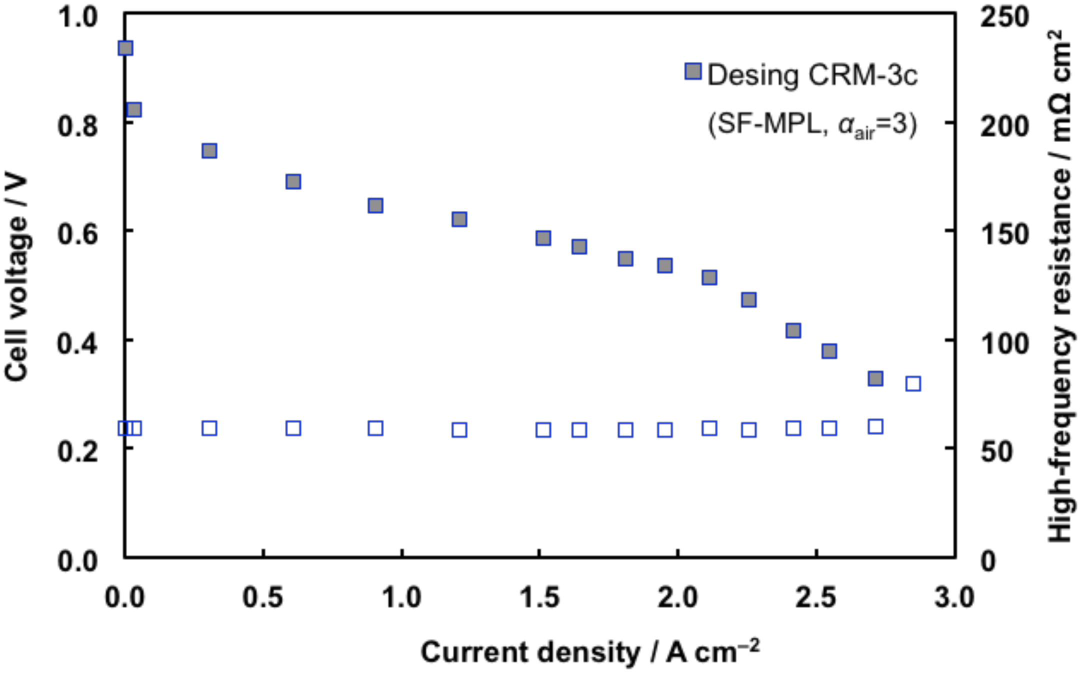

Fig. 4-19. Polarization curve and HFR for Design CRM-3c under a stoichiometry of 3.0.

4.5. Conclusion for Corrugated-mesh Fuel Cell

Here, the performance and HFR for corrugated mesh fuel cells were characterized, and it is found that the flow field utilizing a corrugated mesh significantly reduces the effects of electrode flooding on their performances demonstrate that. Flow-channel patterns affect the HFR of CCMs and MPLs having sandwich configurations. The conductivities of MPLs are a key factor in the present fuel-cell design to enhance their performances. It is also clarified that MPL rigidity is an important factor in facilitating better contact between the catalyst layer and MPL in the corrugated mesh fuel cells. Finally, the performance reached to 0.45 V at 3 A cm^{-2} and an HFR of 62 mΩ cm^{-2} using the combination of a wavy flow pattern and silver-flake MPL. Future studies will involve the calculation of pressure distributions for each MPL under the compression pressure via 3D-FEM as well as calculations of the resistance in these designs, which involve the experimental measurement of contact resistance and Young's modulus. In addition, since the catalyst layer effect on in-plane conduction in the circuit model (assumption (6)) has not been addressed, further investigations of catalyst layer effects on electron transport pathways are planned for the next study.

Furthermore the corrugated-mesh fuel cell with corrugated-mesh flow channel shows larger high-frequency resistance (HFR) than conventional flow fields with GDL. Due to fewer contact points between the corrugated-mesh and the MPL, the electron has to conduct in the in-plane direction of the MPL and CL. This can cause the larger HFR because MPL and CL have lower conductivity and thinner than GDL and electron travel pathways in this case are longer than that of conventional fuel cell. Furthermore, two different MPLs composed of carbon black (CB-MPL) and silver flake (SF-MPL) were tested in the GDL-less fuel cell, and SF-MPL, which has 3 orders of magnitude higher conductivity than CB-MPL, shows similar HFR as CB-MPL and both of them shows higher HFR than that of conventional fuel cell. It indicates that only the effect of the conductivity of MPL cannot account for the HFR difference in these fuel cells, and hence not only the conductivity but also contact resistance of corrugated-mesh|MPL and MPL|CL may have a strong affect on the total HFR under severely non-uniform compression pressure distribution. Although the contact resistance heavily depends on the contact pressure and the contact pressure distribution is determined by the elasticity modulus and thickness of the MPL [32], stainless steel MPL (SS-MPL) was used in stead of SF-MPL to investigate the effect of the modulus of MPL, and SS-MPL showed lower HFR than that of SF-MPL. This indicates that stiffer MPL can distribute the compression pressure and can reduce the contact resistance of MPL|CL. However, there is not theoretical model accounting for the electrical resistance issues in the GDL-less fuel cell, and we realize that stress-electrical-electrochemistry simulation should be required for the better understanding on the effect of electrical conductivity and contact resistance.

In the next chapter 5, we report mechanical and electrical properties of corrugated mesh, MPLs and CL as well as GDL. We also report a three-dimensional model with mechanical-electrical-electrochemical coupling for the corrugated-mesh fuel cell with unity gas, single phase and isothermal condition, and validate the model against the experimental performance for conventional and corrugated-mesh fuel cell to see this model can be available for these fuel cell. In addition we also check the contribution of material conductivities and contact resistance to the performance in each fuel cell.

Bibliography for Chapter 4

[1] A. Turhan, K. Heller, J.S. Brenizer, M.M. Mench, J. Power Sources 180 (2008) 773–783.

[2] A. Higier, H. Liu, J. Power Sources 193 (2009) 639–648.

[3] M. Mathias, J. Roth, J. Fleming, W. Lehnert, W. Vielstich, H. Gasteiger, A. Lamm (Eds.), Handbook of Fuel Cells: Fundamentals, Technology and Applications, John Wiley & Sons, New York, 2003, vol. 3.

[4] F.Y. Zhang, S.G. Advani, A.K. Prasad, J. Power Sources 176 (2008) 293–298.

[5] ASTM Standard C611, Standard Test Method for Electrical Resistivity of Manufactured Carbon and Graphite Articles at Room Temperature (2010), ASTM International, West Conshohocken, PA, 2003.

[6] N. Cunningham, M. Lefèvre, G. Lebrun, J.P. Dodelet, J. Power Sources 143 (2005) 93–102.

[7] M.V. Williams, H.R. Kunz, J.M. Fenton, J. Electrochem. Soc. 152 (2005) A635–A644.

[8] I.S. Hussaini, C.Y. Wang, J. Power Sources 195 (2010) 3830–3840.

[9] E. Aker, K.J Måløy, A. Hansen, G.G. Batrouni, Transp. Porous Media 32 (1998) 163–186.

[10] Z. Lu, C. Rath, G. Zhang, S.G. Kandlikar, Int. J. Hydrogen Energy 36 (2011) 9864–9875.

[11] A. Turhan, S. Kim, M. Hatzell, M.M. Mench, Electrochim. Acta 55 (2010) 2734–2745.

[12] Y. Wang, S. Al Shakhshir, X. Li, Appl. Energy 88 (2011) 2168–2175.

[13] J.P. Owejan, T.A. Trabold, D.L. Jacobson, D.R. Baker, D.S. Hussey, M. Arif, Int. J. Heat Mass Transfer 49 (2006) 4721–4731.

[14] S.J.C. Cleghorn, D.K. Mayfield, D.A. Moore, J.C. Moore, G. Rusch, T.W. Sherman, N.T. Sisofo, U. Beuscher, J. Power Sources 158 (2006) 446–454.

[15] J.P. Owejan, J.J. Gagliardo, J.M. Sergi, S.G. Kandlikar, T.A. Trabold, Int. J. Hydrogen Energy 34 (2009) 3436–3444.

[16] S. Ge, C.Y. Wang, Electrochem. Solid State Lett. 9 (2006) A499–A503.

[17] M.L. Perry, T.F. Fuller, J. Electrochem. Soc. 149 (2002) S59–S67.

[18] E. Antolini, R.R Passos, E.A Ticianelli, J. Power Sources 109 (2002) 477–482.

[19] P.G. Stampino, L. Omati, C. Cristiani, G. Dotelli, Fuel Cells 10 (2010) 270–277.

[20] S. Kim, M.M. Mench, J. Electrochem. Soc. 156 (2009) B353–B362.

[21] U. Pasaogullari, C.Y. Wang, K.S. Chen, J. Electrochem. Soc. 152 (2005) A1574–A1582.

[22] J.M. Morgan, R. Datta, J. Power Sources 251 (2014) 269–278.

[23] K.R. Cooper, M. Smith, J. Power Sources 160 (2006) 1088–1095.

[24] M. Ciureanu, R. Roberge, J. Phys. Chem. B 105 (2001) 3531–3539.

[25] S. Asghari, A. Mokmeli, M. Samavati, Int. J. Hydrogen Energy 35 (2010) 9283–9290.

[26] S.J.C. Cleghorn, C.R. Derouin, M.S. Wilson, S. Gottesfeld, J. Appl. Electrochem. 28 (1998) 663–672.

[27] T. Swamy, E.C. Kumbur, M.M. Mench, J. Electrochem. Soc. 157 (2010) B77–B85.

[28] I.N. Sneddon, Int. J. Eng. Sci. 3 (1965) 47–57.

[29] I.V. Zenyuk, E.C. Kumbur, S. Litster, J. Power Sources 241 (2013) 379–387.

[30] T. Swamy, F.E. Hizir, M. Khandelwal, E.C. Kumbur, M.M. Mench, ECS Trans. 25 (2009) 15–27.

[31] R. Holm, Electric Contacts, 4th ed., Springer, New York, 1967.

[32] J. Kleemann, F. Finsterwalder, W. Tillmetz, J. Power Sources 190 (2009) 92–102.

Chapter 5. Numerical Modeling Study for Corrugated-mesh Fuel Cell

5.1 Introduction for Numerical Modeling

In a previous chapter 4, the corrugated-mesh fuel cell shows a cell voltage of 0.45 V at 3.0 A cm^{-2}, without experiencing a significant voltage drop even at a relatively high current density of over 1 A cm^{-2}, by utilizing a corrugated-mesh in the flow channel located directly on the microporous layer (MPL), without using a GDL. It was concluded that the corrugated-mesh flow channel could supply the reactant gases uniformly to the CL, with no significant indication of flooding up to 3.0 A cm^{-2} in the polarization curve. On the other hand, the GDL-less fuel cell with a corrugated-mesh flow channel shows a larger high-frequency resistance (HFR) compared to the cells having conventional flow fields with a GDL. Owing to the fewer contact points between the corrugated-mesh and the MPL, the electron has to be conducted in the in-plane direction of the MPL and CL, which can cause a larger HFR, since the MPL and the CL have lower conductivity and are thinner than the GDL. In addition, the electron travel pathway in this case is longer than that in conventional fuel cells. Furthermore, four different MPLs; carbon black MPL (CB-MPL), graphite flake MPL (GF-MPL), silver flake MPL (SF-MPL) and stainless steel MPL (SS-MPL) were tested in the GDL-less fuel cell. The HFRs for these fuel cells utilizing these MPLs showed same HFR order as these MPL conductivities. However, the 2 dimensional electrical circuit model with the conductivity of the MPLs cannot account for the HFR difference between these fuel cells, and hence not only the conductivity, but also the contact resistance of the corrugated-mesh|MPL and the MPL|CL interfaces may have a strong effect on the total HFR under highly non-uniform compression pressure distribution conditions. The contact resistance heavily depends on the contact pressure and the contact pressure distribution is determined by the elasticity modulus and the thickness of the MPL [1]. However, there is no theoretical model accounting for the electrical resistance in the GDL-less fuel cells, and we realized that stress-electrical-electrochemical simulations would be required to gain a better understanding of the effect of electrical conductivity and contact resistance on the cell performance.

In this chapter, the mechanical and electrical properties of corrugated-mesh, MPLs, CL, and the GDL were measured, and, a three-dimensional coupled model was developed, incorporating mechanical, electrical, and electrochemical considerations under uniform gas concentration, single phase, and isothermal conditions without any fluid and thermal modeling, and validated the model with the fuel cell performance results obtained in Chapter 4, understand the influence of material conductivities and contact resistance on the performance of each fuel cell. We assumed that the gas was supplied uniformly and therefore, did not model gas and liquid water transport in this study.

5.2 Characterizations

5.2.1 Electrical Conductivities

The electron travel path between the CL and BPP in GDL-less fuel cells is thought to be different from that in the conventional fuel cells and this difference is expected to lead to different internal electrical resistances. For example, electrons in Design CNV travel between the CL and the MPL vertically to the GDL because the GDL covers the entire active area relatively uniformly [2]. In Designs CRM-3a–3c, which do not have GDLs, the electrons travel vertically in the MPL and the CL and are concentrated at the contact point of the corrugated-mesh and the MPL. In order to characterize these effects, the electrical resistances and the contact resistances were measured for the BPP, GDL, corrugated-mesh, MPL, and CL as a function of the compression pressure used in the numerical model. It may be noted that the GDL, MPL, and CL are porous materials and hence the conductivity of these materials are thought to vary with a change in porosity when they are subjected to a compressive pressure [3].

Fig. 5-1(a)–(b) shows the set up for the measurement of the through-plane electrical resistance conducted at 80 ºC, according to the method described in the literature, [4] for electrical conductivity and contact resistance data. As shown in Fig. 3-7(a), a circular sample with a diameter of 20 mm was placed on a load cell (ElectroPuls™ E1000, Instron, Massachusetts, USA) between two stainless steel (SS) pedestals that were plated with 1 μm thick gold coatings, and the sample was subjected to a compression pressure of 0.025–2.5 MPa. A resistance meter (1750 LCR Dig-Bridge with Kelvin clip leads, Quad Tech Inc., Maynard, USA) was used to obtain the overall resistance of the sample and the contact resistance between the sample and the SS pedestals. The material resistances of the SS pedestals and the cables are negligible since they are made of metals. After the compressive stress stabilized (30–60 min), the resistance was measured and converted to an overall area resistance value, by accounting for the sample geometry.

Generally, the total resistance value contains contributions from the sample resistance and the contact resistance between the sample and the plates. Samples of various thicknesses were measured to deconvolute the two resistances, by considering the fact that the contact resistances are the same in samples of different thicknesses made of the same material, whereas the material resistances for samples of different thicknesses are proportional to the thickness value [5]. Therefore, a plot of the total resistance against thickness should be linear, and an estimate of its intercept (at zero thickness) yields the contact resistance, whereas the slope (Δtotal resistance/Δthickness) provides the material resistance value. In this study, we measured the total resistances of samples with different thicknesses for each sample type (CL samples were 1.5 μm, 10 μm, 19 μm, and 28 μm thick, CB-MPL samples were 40 μm, 75 μm, and 100 μm thick, SF-MPL samples were 40 μm, 80 μm, and 160 μm thick, and GDL samples were 118 μm, 202 μm, 318 μm, and 412 μm thick) and the overall resistances for each sample type were plotted against the corresponding thicknesses. The intercepts and slopes of the plots were calculated for estimating the samples|SS pedestal contact resistances and the material conductivity, respectively. In addition, flat-graphite and gold plated flat-mesh were measured in the same manner to calculate the flat-graphite|SS pedestal and the flat-mesh|SS pedestal contact resistances. These contact resistance values are used later in the calculation of the contact resistance between two samples. The electrical conductivities for flat-graphite and flat-mesh are known and therefore samples with different thicknesses were not measured for these materials. The electrical conductivities of graphite and SS for the corrugated-mesh were collected from the literature [6–7] and the porosity of the mesh was 30.7% [8]. Based on the porosity value, the electrical conductivity of the mesh was assumed to have a 30.7% contribution from SS [9] in the corrugated-mesh sample. The conductivity values are listed in in Table 5-1.

5.2.2 Electrical Contact Resistances

Furthermore, the resistances of several interfaces were measured for conventional fuel cell (Design CNV), namely flat-graphite|GDL, GDL|CB-MPL, and CB-MPL|CL. Similarly, for corrugated-mesh fuel cell (designs CRM 1–3), the resistances of the flat-graphite|flat-mesh, flat-mesh|MPL, and MPL|CL interfaces were measured. For these measurements, the desired combination of samples was set between two SS pedestals and the overall resistances were obtained in the same manner described above. Fig. 5-1(b) shows a schematic illustration of the method for the measurement of the contact resistance between two samples (sample1|sample2). The total resistance was composed of the contact resistances of SS|sample1, sample1|sample2, and sample2|SS, in addition to the material resistances of SS, sample1, and sample2. In order to calculate the contact resistance of sample1|sample2, the material resistances for each layer and the contact resistances of SS|sample1 and sample2|SS were subtracted from the overall resistance [10].

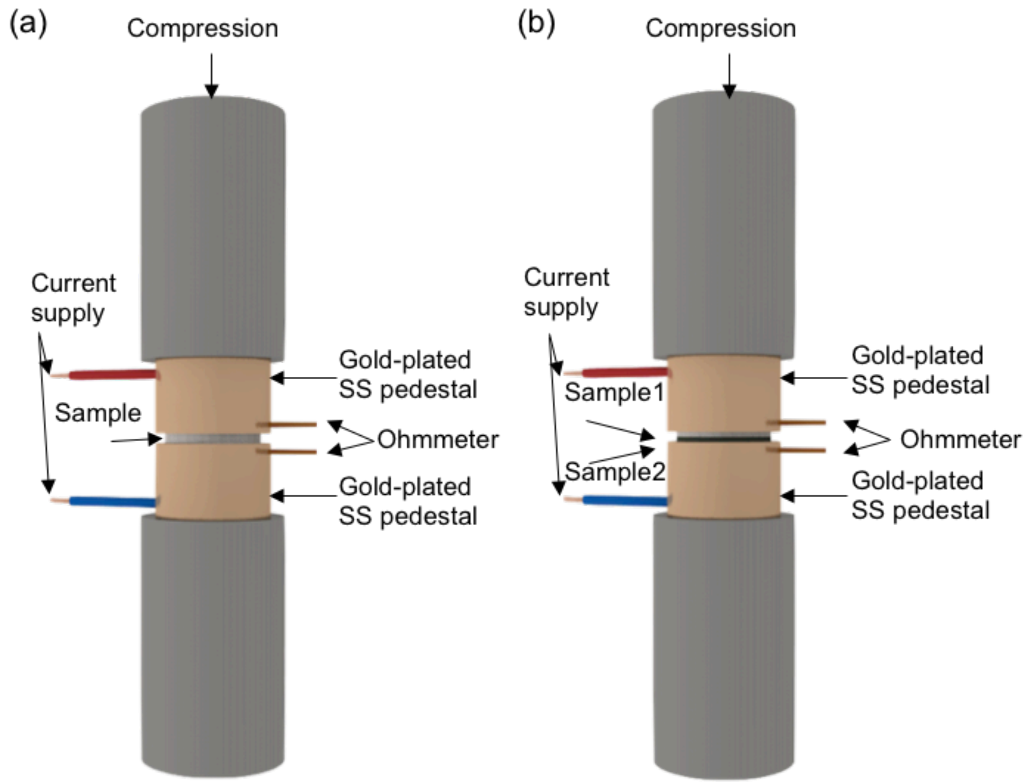

Fig. 5-1. Schematic image of (a) conductivity measurement under compression pressure using different thicknesses, (b) contact resistance measurement under compression pressure using two sheets with different materials.

5.2.3 Mechanical properties

As described at the introduction section in this chapter, the contact resistance depends heavily on the contact pressure. In the fuel cell, the contact pressure and its distribution are determined by the compression force, component thicknesses, and the compressive elasticity modulus of each element. The compressive elasticity modulus for the CL, MPL, GDL, and the straight and waved corrugated-mesh were measured at 80 ºC using the same load cell and the conditions described in the section 5.2.1 according to the procedure described in the literature [11]. The values of the Poisson’ ratio of each material were collected from literature [12–13] and the elasticity moduli of graphite and SS for the BPP and SS-MPL, respectively, as well as the membrane were collected from the literature [7, 14].

5.3 Measurement results and numerical model

5.3.1 Mechanical stress analysis

The finite element method (FEM) is widely used for analyzing the mechanical stress in fuel cells [2, 12, 14–15]. A three-dimensional finite element model was developed. STAR-CCM+ (CD-adapco, N.Y.) was used as the simulation software. We chose Design CNV (conventional fuel cell) and Design CRM-3 series for the investigation of the internal electrical, namely Design CRM-3a (CB-MPL), Design CRM-3c (SF-MPL) and Design CRM-3d (SS-MPL) and these geometry models are shown in Fig. 5-2(a)–(d). The modeld active area size is 2 mm x 2 mm for Design CNV and 0.6 mm x 2 mm for Design CRM-3a–CRM 3d respectively. The fuel cell model was fixed in the through-plane direction at the bottom of the anode BPP and all the layer interfaces were bonded to prevent them from slipping. Compression loads of 0.5 MPa and 0.2 MPa were applied for the conventional and corrugated fuel cells, respectively, to maintain a contact pressure of 1 MPa at the land|GDL interface in the conventional fuel cell and at the corrugated-mesh|MPL interface in the corrugated-mesh fuel cell. This value is the same as the compression pressure measured with the pressure sensitive paper (Precale film, FUJIFILM), as described in the section 4.2.3 for corrugated-mesh fuel cell preparation.

In order to conduct the analysis, the geometrical models for conventional and corrugated-mesh fuel cells were constructed using the geometrical data and properties listed in Table 5-1. Some simplifying assumptions such as isothermal, isotropic, and linear elastic body conditions were used in the construction of the model.

For the simplification of the corrugated-mesh, firstly, the mesh was modeled as solid region and then shaped for straight and waved corrugated-mesh, because the mesh was composed of 50-µm-diameter stainless steel fiber and it is difficult to model each fibers in the mesh with a current computer capability for the number of volume cells in FEM analysis. Secondary, the bulk elastic moduli for straight and waved corrugated-mesh obtained in the mechanical property measurement described in 5.2.3 were used as a local elastic modulus for each corrugated-mesh in the simulation model. Strictly speaking, the bulk elastic modulus for the flat-mesh should be used for the local elastic modulus, but it is difficult to measure the mechanical properties of the flat-mesh due to its flexibility and anisotropy derived from its nature of woven-fiber, and it is also difficult to adapt the properties to the model because of its anisotropy and its work-hardening in the corrugation. These modeling method is tricky and a proper method should be developed in the future.

Table 5-1. Mechanical and electrical properties.

Properties	Material	Value	Unit	Reference
Flow field geometry	Rib/channel width (BPP)	1.0/1.0	mm	This work
	Channel depth (BPP)	1.0	mm	This work
	Corrugation height	0.3	mm	This work
	Corrugation width	0.3	mm	This work
	Thickness of mesh	0.1	mm	This work
Thickness	GDL	200	μm	This work
	MPL	40	μm	This work
	CL	10	μm	This work
	Membrane	25	μm	This work
Porosity	Stainless steel mesh	30.7	%	[8]
Electrical conductivity	Graphite	1.28×10^{5}	S m^{-1}	[6]
	Stainless steel	1.39×10^{6}	S m^{-1}	[7]
	Corrugated-mesh	4.27×10^{5}	S m^{-1}	This work
Modulus of elasticity	Graphite	13.7	GPa	[7]
	Stainless steel	195	GPa	[7]
	Straight corrugated-mesh	15.9	MPa	This work
	Waved corrugated-mesh	18.6	MPa	This work
	GDL	22.1	MPa	This work
	CB-MPL	2.5	MPa	This work
	SF-MPL	2.3	MPa	This work
	CL	2.0	MPa	This work
	Membrane	54.7	MPa	[14]
Poisson's ratio	Graphite	0.21	-	[12]
	Stainless steel	0.3	-	[12]
	GDL	0.13	-	[13]
	CB-MPL	0.25	-	This work
	SF-MPL	0.25	-	This work
	CL	0.25	-	[13]
	Membrane	0.40	-	[13]

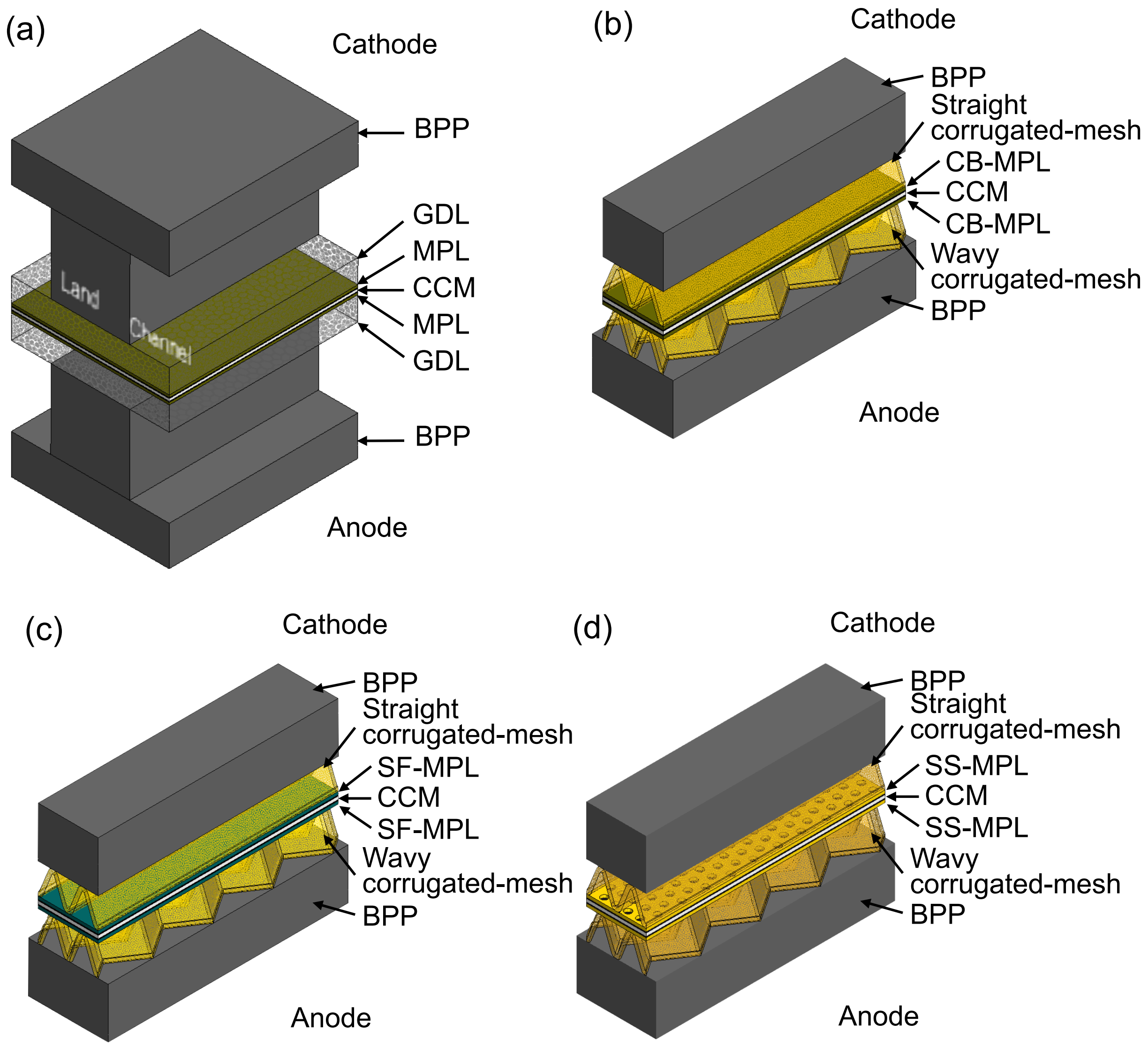

Fig. 5-2. Geometric model of (a) Design CNV (conventional fuel cell), (b) Design CRM-3a (corrugated-mesh fuel cell with CB-MPL), (c) Design CRM-3c: corrugated-mesh fuel cell with SF-MPL, (d) Design CRM-3d (corrugated-mesh fuel cell with SS-MPL).

5.3.2 Electrical conductivity and contact resistance analysis

Fig. 5-3(a)–(d) plots the overall through-plane resistance as a function of the compression pressure for GDL, CB-MPL, SF-MPL, and CL samples with different thicknesses, between two gold-plated SS pedestals. As typically reported in the literature [2, 16], the overall resistance decreased with an increase in the compression pressure. In order to deconvolute the values of the contact resistance and the material resistance, the overall resistance was plotted against the thickness of the samples. An example of such a plot for the case of the CL is shown in Fig. 5-4. The overall resistance R_{overall} is described by equation (5-1).

$$R_{\mathrm{overall}} = 2R_{\mathrm{C.SS|sample}} + R_{\mathrm{M.sample}}\, h_{\mathrm{sample}} \tag{5-1}$$

where $R_{\mathrm{C\cdot SS|sample}}$ is the contact resistance of the SS|sample interface, $R_{\mathrm{M.sample}}$ is the area resistivity of the sample, and h_{sample} is the thickness of the sample. In Fig. 5-4, the slopes of the plots represent $R_{\mathrm{M.sample}}$, whereas the intercepts of the plots represent 2 x $R_{\mathrm{C.SS|sample}}$. Fig. 5-3 shows the conductivities of the samples (i.e., inverse of $R_{\mathrm{M.sample}}$), as a function of the compression pressure, and Fig. 5-5 shows the contact resistances of the samples|SS interfaces. As shown in Fig. 5-3, the conductivities of CL, CB-MPL, SF-MPL, and GDL increased slightly with an increase in the compression pressure. These are porous materials composed of powders, flakes and fibers, and under compressive pressure, the total void space between the particles is reduced and the contact area with neighboring particles increases, which can lead to an increase in the electrical conductivity, as described in the literature [3]. As shown in Fig. 5-6, the contact resistance decreased significantly as the compression pressure increased. As discussed by B.M. Vogler et al [10], the asperities on the surface of the samples are reduced under compressive pressure, which enhances the contact between the samples.

Fig. 5-7 shows the experimental results for the overall resistances of two samples sandwiched between gold-plated SS pedestals, as a function of the compression pressure. In order to determine the contact resistance between two samples (sample1|sample2), the overall resistance Roverall may be expressed as shown in equation (5-2).

$$R_{\mathrm{overall}} = R_{\mathrm{C.SS|sample1}} + R_{\mathrm{M.sample1}}\, h_{\mathrm{sample1}} + R_{\mathrm{C.sample1|sample2}} + R_{\mathrm{M.sample2}}\, h_{\mathrm{sample2}} + R_{\mathrm{C.SS|sample2}} \tag{5-2}$$

where $R_{\mathrm{C.SS|sample1}}$ is the contact resistance of the SS|sample1 interface, $R_{\mathrm{M.sampe1}}$ is the area resistivity of sample1, h_{sample1} is the thickness of sample1, $R_{\mathrm{M.sample2}}$ is the area resistivity of sample2, h_{sample2} is the thickness of sample2, $R_{\mathrm{C.sample1|sample2}}$ is the contact resistance of the sample1|sample2 interface, and $R_{\mathrm{C.SS|sample2}}$ is the contact resistance of the SS|sample2 interface. To calculate the value of $R_{\mathrm{C.sample1|sample2}}$, the values of $R_{\mathrm{C.SS|sample}}$, $R_{\mathrm{M.sample}}$, and h_{sample}, which were determined from Fig. 5-5 and Fig. 5-6, were subtracted from R_{overall}. Fig. 5-8(a)–(d) shows the result for contact resistance of sample1|sample2 for Design CNV (flat-graphite|GDL, GDL|CB-MPL, and CB-MPL|CL), and Design CRM 3a, 3c, and 3d (flat-graphite|flat-mesh, flat-mesh|MPL, and MPL|CL).

The conductivity for these materials and the contact resistances of various combinations of materials were then incorporated into the mechanical stress analysis model described in previous section 5.3.1, to calculate the conductivity and contact resistance distribution in the fuel cells. The conductivity is set as isotropic for in-plane and through-plane direction under each compression pressure.

The number of each experiment was only one time, and the experimental error is uncertain in this work. The measurement results under less compression than 0.025 MPa were omitted because of the unstable data obtained during the measurement. Furthermore to reduce the experimental error, the compressive stress was add on each sample for 30–60 min to remove the effect of the initial creep strain and to become more flat and more parallel between the stainless steel pedestals in the load cell.

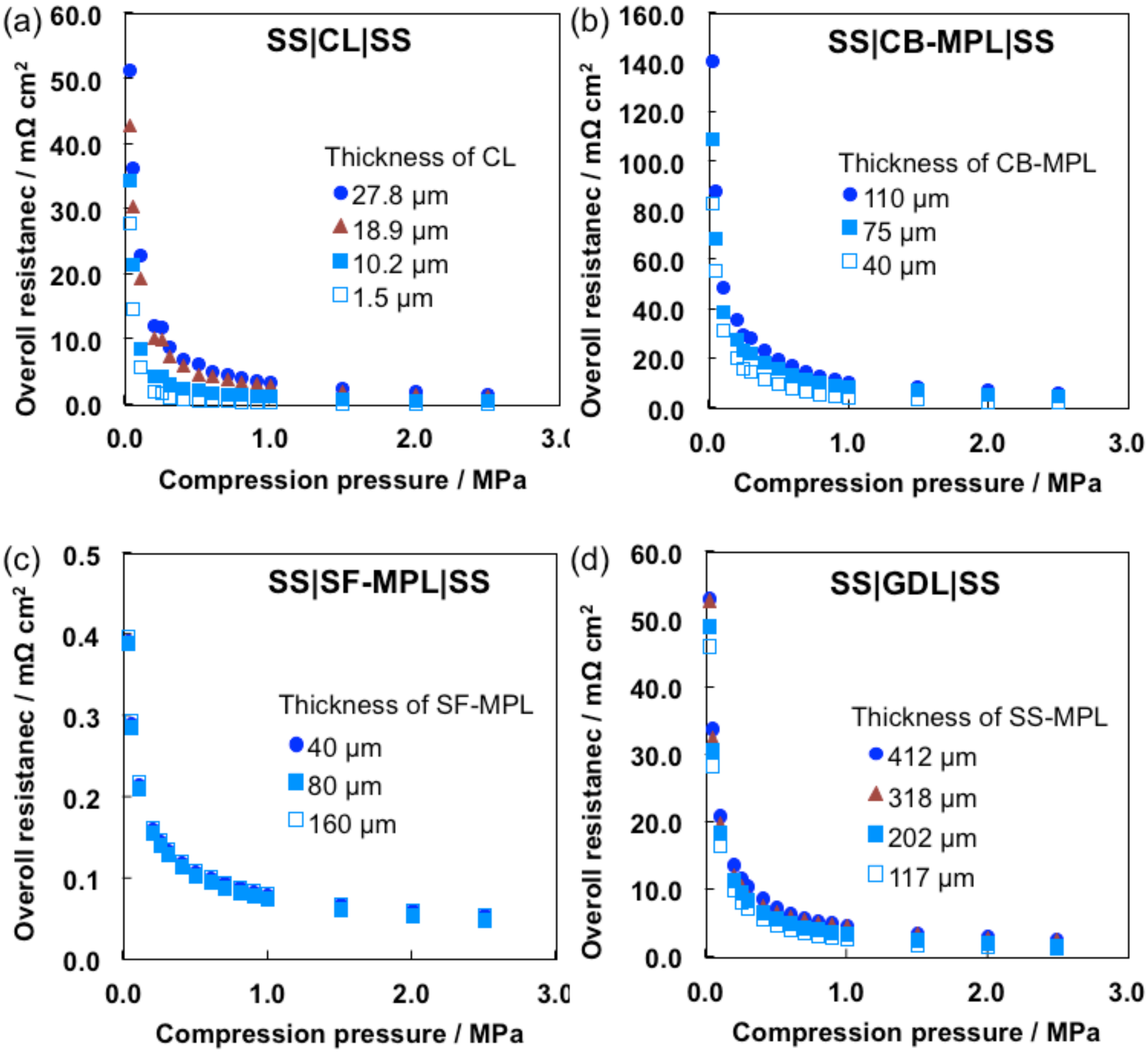

Fig. 5-3. Overall through-plane resistance as a function of the compression pressure for different thickness sample of (a) GDL, (b) CB-MPL, (c) SF-MPL, (d) CL.

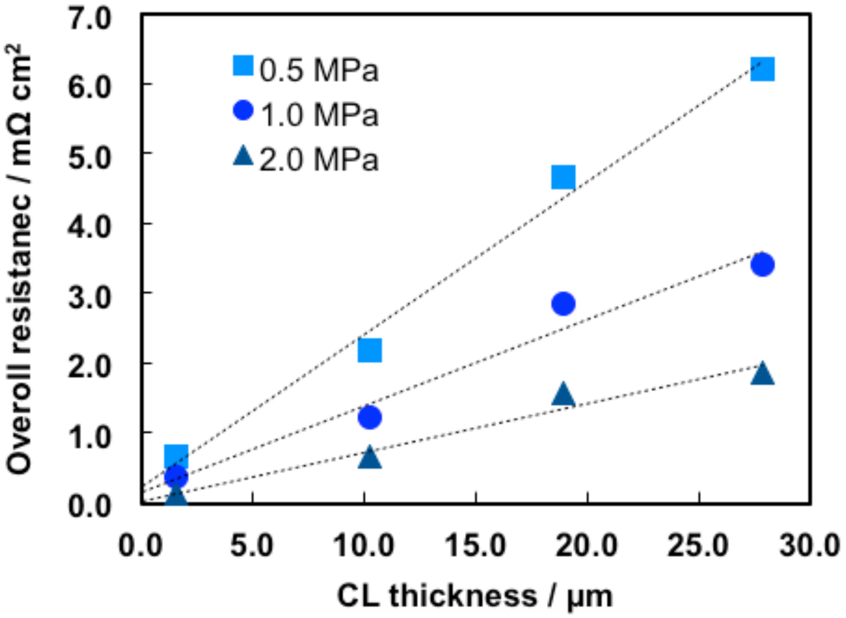

Fig. 5-4. Overall resistance plotted against the thickness for CL.

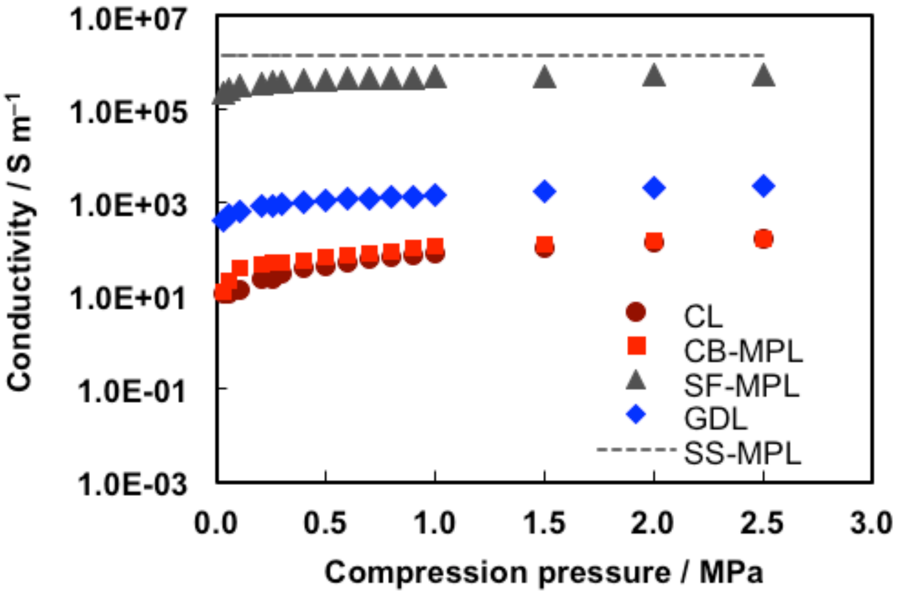

Fig. 5-5. Conductivities of samples as a function of the compression pressure.

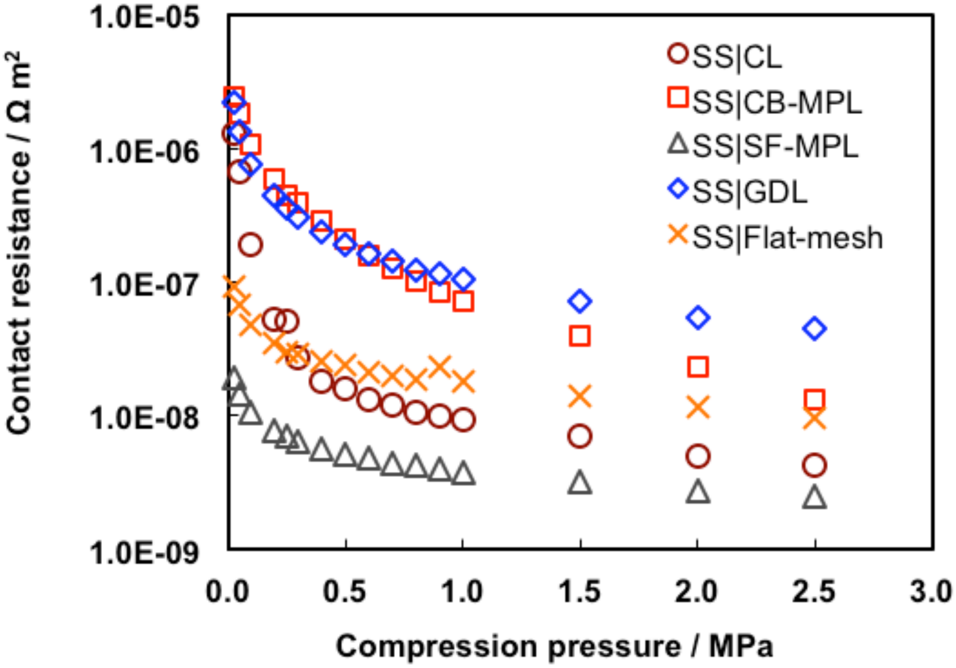

Fig. 5-6. Contact resistance of these samples|SS as a function of the compression pressure.

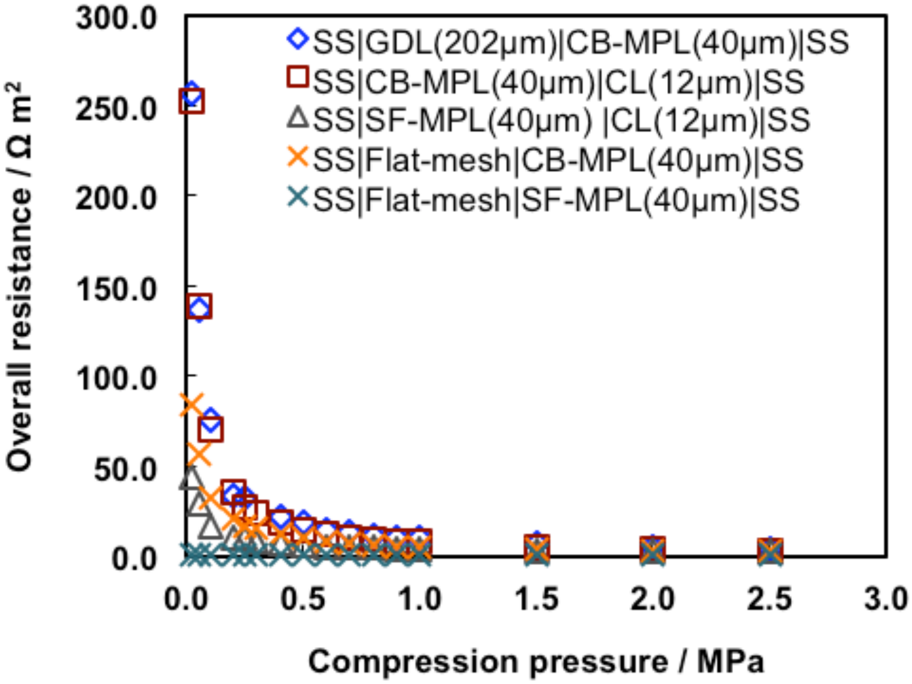

Fig. 5-7, Overall resistance of two different samples as a function of the compression pressure.

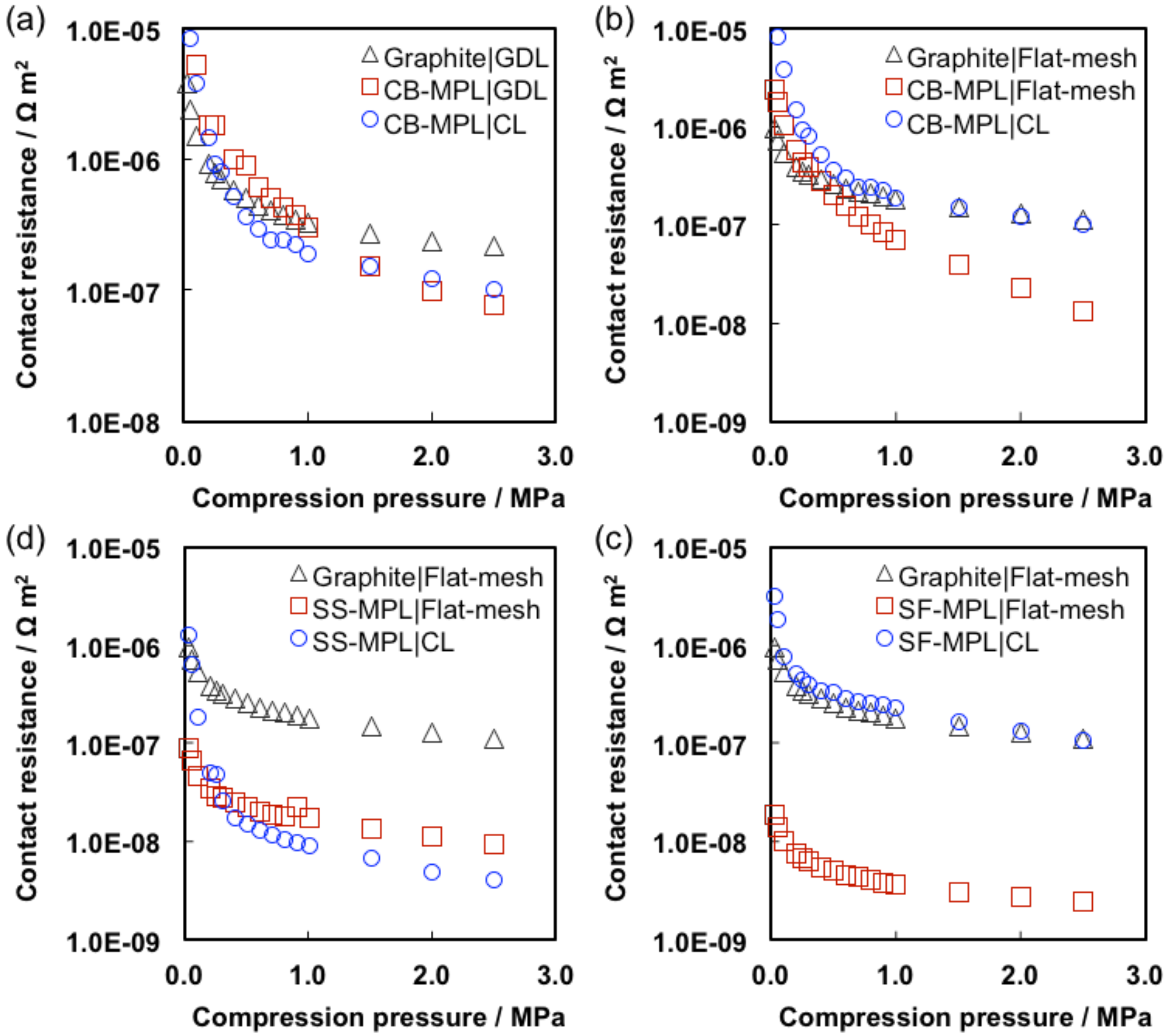

Fig. 5-8. Contact resistance of sample1|sample2 as a function of the compression pressure of (a) Design CNV (conventional fuel cell), (b) Design CRM-3a (corrugated-mesh fuel cell with CB-MPL), (c) Design CRM-3c (corrugated-mesh fuel cell with SF-MPL), and (d) Design CRM-3d (corrugated-mesh fuel cell with SS-MPL).

5.3.3 Electrochemistry Model

The dependence of the potential of the fuel cell on the polarization effects [17] for a single cell is given by equation (5-3).

$$V_{\mathrm{cell}} = V_0 - \eta_{\mathrm{act.a}} - \eta_{\mathrm{act.c}} - \eta_{\mathrm{ohm.mem}} - \eta_{\mathrm{ohm.solid}} \tag{5-3}$$

where V_0 is the open circuit potential, $\eta_{\mathrm{act.a}}$ and $\eta_{\mathrm{act.c}}$ are the activation overpotentials for the anode and the cathode, respectively, $\eta_{\mathrm{ohm.mem}}$ is the ohmic overpotential resulting from the transport of the ions through the membrane, and $\eta_{\mathrm{ohm.solid}}$ is the ohmic overpotential resulting from the electron transport. V_0 has been provided in the literature [18] and is shown in equations (5-4) and (5-5) for the anode and the cathode, respectively.

$$V_0 = 0 \text{ (anode)} \tag{5-4}$$

$$V_0 = 0.025T - 0.2329 \text{ (cathode)} \tag{5-5}$$

Where T is the fuel cell temperature in Kelvin. In the PEMFCs, while the electrons are generated in the anode CL and are transferred to the external current collector through the solid elements (CL, MPL, GDL, corrugated-mesh, and BPP) on the anodic side, the electrons return to the cathode CL through the solid elements on the cathodic side. On the other hand, the protons travel through the membrane and the ionomers in the CL travel from the anode to the cathode. In general, the Butler-Volmer (B–V) equation is used to describe the electron and proton source terms in the CL. The following approximations were applied to the B–V equation for the anode and the cathode. In this study, the gas concentration was assumed to be uniform and hence the gas concentration terms in the B–V equation were set to unity. In the anode CL, the kinetics of the hydrogen oxidation reaction (HOR) are fast and hence the overpotential for HOR is small. Therefore, the local current density on the anode side can be expressed by a linearized B–V equation [19], as shown in equation (5-6).

$$j = i_{0.\mathrm{a}} \left(\frac{\alpha_\mathrm{a} + \alpha_\mathrm{c}}{RT} F \eta_{\mathrm{act.a}} \right) \tag{5-6}$$

where j is the volumetric current density, $i_{0.\mathrm{a}}$ is the anode exchange current density, α_a and α_c are the anodic and cathodic charge transfer coefficients for the HOR, respectively, R is the universal gas constant, T is the temperature in Kelvin, and F is the Faraday's constant. On the other hand, at the cathode, the oxygen reduction reaction (ORR) has slow kinetics, and hence the overpotential is high. Therefore, the B–V equation for the ORR is approximated by neglecting the anodic reaction term in the Tafel equation as shown in equation (5-7) [19].

$$j = - i_{0.\mathrm{c}} \exp \left(- \frac{\alpha_\mathrm{c}}{RT} F \eta_{\mathrm{act.c}} \right) \tag{5-7}$$

where $i_{0.\mathrm{c}}$ is the cathode exchange current density and α_c is the cathodic charge transfer coefficient for the ORR. The values of the electrochemical parameters were obtained from the literature [20]. The variation in the exchange current density as a function of temperature was computed using the empirical relationship proposed by Parthasarathy et al. [21]. In this study, the proton conductivity of the membrane was assumed to be uniform in all the regions without considering the water transfer and water conductivity in the membrane [22–23]. Therefore, η_{mem} was constant and was calculated as shown in equation (5-8).

$$\eta_{\mathrm{mem}} = j\left(\frac{h_{\mathrm{mem}}}{\sigma_{\mathrm{mem}}}\right) \tag{5-8}$$

In the above equation, σ_{mem} is the proton conductivity in the membrane, which was obtained from the literature [24] and h_{mem} is the membrane thickness. The ohmic overpotential for electrons (η_{solid}) consists of the overpotentials arising from electron transport through the BPP, GDL, corrugated-mesh, MPL, and CL with contact resistances between each set of layers. All the parameters and properties are listed in Table 5-2.

The simulations for the polarization curves for Design CNV and Designs CRM-3a–3d were conducted with this electrochemical model and the electrical conductivity and contact resistance values determined under mechanical compression pressure. All the simulations were done by assuming isothermal, single-phase, and uniform gas concentration conditions. In addition, to estimate the effect of conductivity and contact resistance, three cases were simulated, namely by considering (a) material conductivity and contact resistance, (b) only material conductivity, and (c) not considering any electrical resistances (theoretical polarization).

Table 5-2. Electrochemistry modeling parameters.

Symbol	Parameter	Value	Unit	Reference
h_{mem}	Membrane thickness	25×10^{-6}	m	This work
$i_{0,\mathrm{a}}$	Exchange current density (anode)	10^{9}	A m^{-3}	[20]
$i_{0,\mathrm{c}}$	Exchange current density (cathode)	10^{4}	A m^{-3}	[20]
F	Faraday constant	96,487	C mol^{-1}	-
R	Universal gas constant	8.314	J mol^{-1} K^{-1}	-
α_{a}	Anodic transfer coefficient for HOR	1	-	[20]
α_{c}	Cathodic transfer coefficient for HOR	1	-	[20]
α_{c}	Cathodic transfer coefficient for ORR	1	-	[20]
σ_{mem}	Proton conductivity in membrane	0.1	S m^{-1}	[24]
T	Temperature	343	K	This work
V_0	Open circuit potential at 70 ºC	1.12	V	[18]

5.4 Results and Discussion

5.4.1 Compression Pressure Distribution Analysis

Fig. 5-9(a)–(d) shows the results of the stress analysis under compression pressure for designs. All the case shows the pressure of 1 MPa at the interface of GDL|land in Design CNV and at the interface of corrugated-mesh|MPL, as same as pressure sensitive film descried in previous section 3.2.1. To achieve this pressure in a specific area, 0.5 MPa and 0.2 MPa compressive pressures were applied at the end of the BPP for Design CNV (conventional fuel cell) and Designs CRM 3a–3d, respectively.

In Fig. 5-9(a), which shows the results of the stress analysis for design CNV, the GDL distributes the pressure relatively uniformly on the MPL and the CL from the under-land area to the under-channel area. The distribution depends on the modulus and thickness of the GDL and the widths of the land and the channel [5]. On the other hand, in Fig. 5-9(b)–(c) which shows the results for designs CRM-3a and CRM-3c, although the corrugated-mesh is directly compressing the MPL, the pressure distributions are uneven and concentrated under the peak area of corrugation on the MPL as well as the CL. The contact area of the corrugation-peak|MPL interface is tiny with line-contact and the MPL also has a lower modulus and thickness than the GDL. Therefore, the MPL cannot distribute the compression load widely onto the CL through the MPL, unlike the GDL in design CNV. Noticeably, a larger area of the MPL|CL interface is under a small contact pressure of 0-0.1 MPa in Designs CRM-3a and CRM-3c, compared to Design CNV. In Fig. 5-9(d), which shows the results for design for Design CRM-3d, the pressure is intensively applied on the SS-MPL and is distributed evenly on the CL through the SS-MPL. The SS-MPL is stiff enough to allow the pressure to be applied onto the CL area. In addition, the contact resistance distribution of the SS-MPL|CL interface is higher on average compared to designs CRM-3a and CRM-3c. However, the CL under the through-holes of the SS-MPL is not covered with any layer.

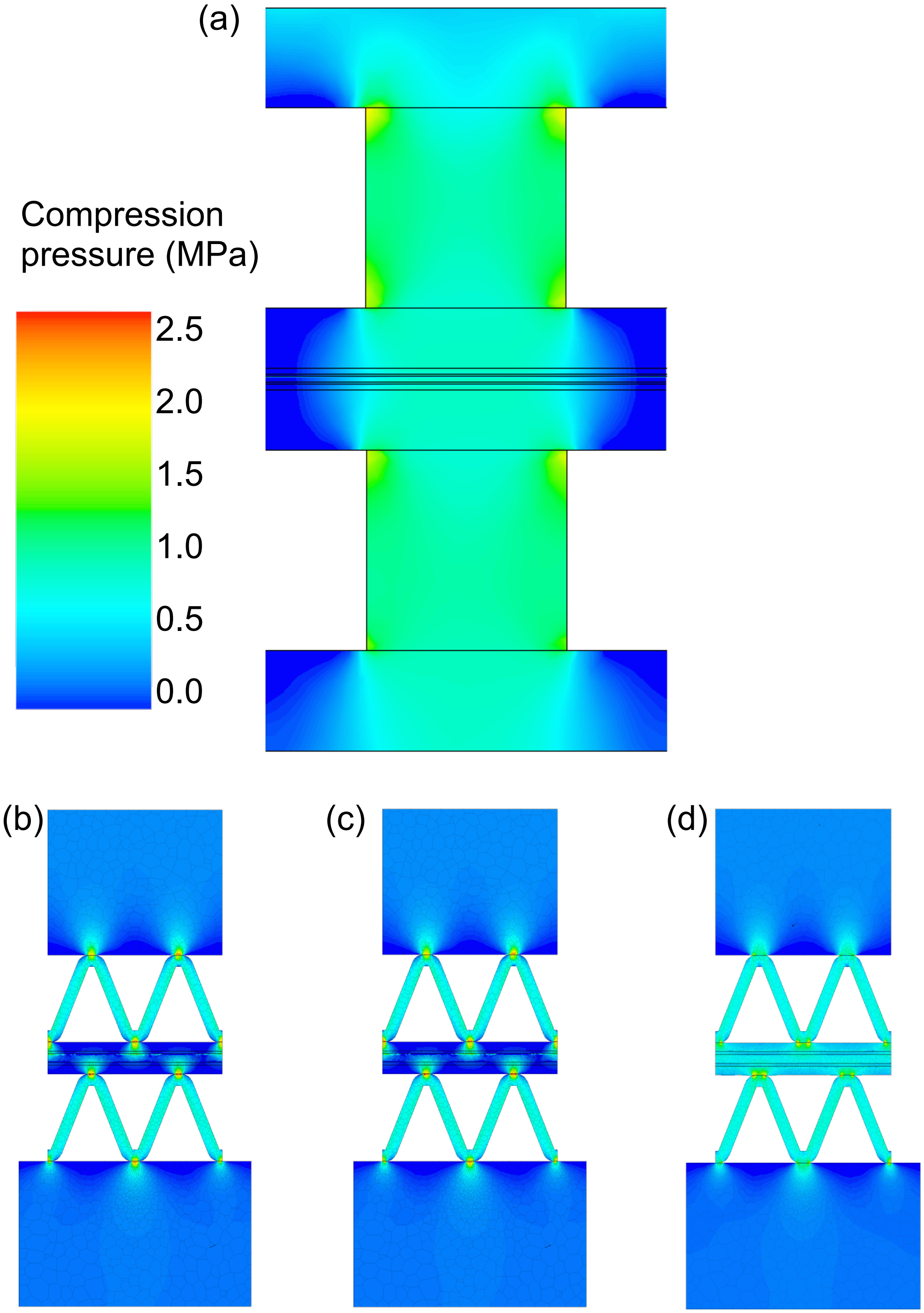

Fig. 5-9. Stress analysis results under compression pressure of (a) Design CNV (conventional fuel cell), (b) Design CRM-3a (corrugated-mesh fuel cell with CB-MPL), (c) Design CRM-3c (corrugated-mesh fuel cell with SF-MPL), and (d) Design CRM-3d (corrugated-mesh fuel cell with SS-MPL).

5.4.2 Electrical Conductivity and Contact Resistance Distribution Analysis

Fig. 5-10(a)–(d) shows the results of the electrical analysis under compression pressure for designs CNV, CRM-3a–3d. The effect of electrical conductivity and contact pressure were simulated in these fuel cells under the compression pressures obtained in section 5.3.2, using the measured conductivity and contact resistance data in Table 5-1, Fig. 5-5 and Fig. 5-8.

In Fig. 5-10(a), which shows the results for Design CNV, the conductivity and contact resistance is relatively uniform, since the compression pressure distribution is uniform as explained in section 5.4.1 in Fig. 5-9(a). Strictly speaking, the conductivity of the GDL is expected to be anisotropic because of the anisotropic nature of the GDL structures [25]. However as per the report of T. Zhou et al., the fuel cell powers obtained with an isotropic conductivity of 300 S m^{-1} show a difference of less than 2.5 % than those obtained with isotropic conductivities of 17200 S m^{-1} and 1250 S m^{-1}, for in-plane and through-plane measurements, respectively [26]. In our present study, the conductivity of the GDL was around 500–1600 S m^{-1} depending on the compression pressure and these values are thought to provide power within a 2.5 % variation, from the anisotropic conductivity case. In Fig. 5-10(b)–(c) shows the conductivity and contact resistance for designs CRM-3a and CRM-3c. In both the cases, the contact resistances of the MPL|CL interfaces are uneven. Low contact resistances are seen only under the areas of the corrugation–peak, whereas high contact resistance is seen in the remaining areas, because of the uneven compression pressure from the corrugated–mesh and the soft nature of the MPLs. While the conductivity distributions are high for both deigns CRM-3a as well as

CRM-3c, but the SF-MPL in CRM-3c has a higher conductivity than the CB-MPL in CRM-3a, owing to the conductivity difference between CB–MPL and SF–MPL. On the other hand, in Fig. 5-10(d) which shows the results for Design CRM-3d, the contact resistance of the SS–MPL|CL interface is more uniformly distributed and the conductivity of SS–MPL is maintained high and constant against the compression pressure distribution. Comparing the Designs CRM-3a and CRM-3c for the MPL conductivity and the contact resistance of MPL|CL, Design CRM-3a has high contact resistance and low conductivity, Design CRM-3c has high contact resistance and high conductivity, whereas Design CRM-3d has a low contact resistance and high conductivity. The effects of the contact resistance and the conductivity on the performance of the fuel cells are investigated in the next section (section 5.4.3).

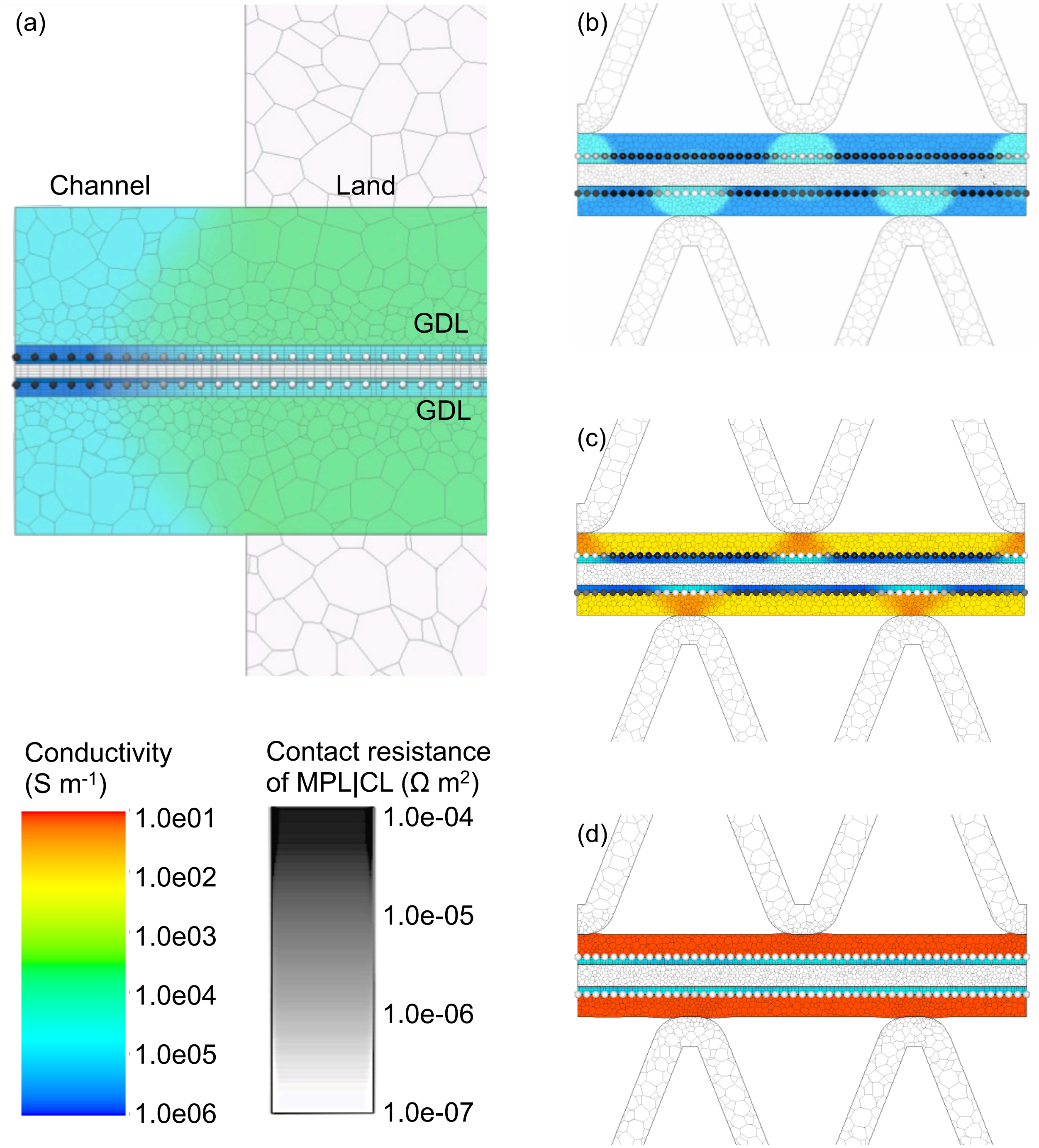

Fig. 5-10. Electrical resistance analysis results under compression pressure of (a) Design CNV (conventional fuel cell), (b) Design CRM-3a (corrugated-mesh fuel cell with CB-MPL), (c) Design CRM-3c (corrugated-mesh fuel cell with SF-MPL), and (d) Design CRM-3d (corrugated-mesh fuel cell with SS-MPL).

5.4.3 Polarization curve

Fig. 5-11 shows the experimentally measured polarization curves for Design CNV (conventional flow field with GDL and CB-MPL; Fig. 5-11(a)), Design CRM-3a (corrugated-mesh with CB-MPL; Fig. 5-11(b)), Design CRM-3c (corrugated-mesh with SF-MPL; Fig. 5-11(c)), and Design CRM-3d (corrugated-mesh with SS-MPL; Fig 5-11 (d)). As discussed in previous introduction session 5.1, the experimental polarization curves for Design CNV shows gradual voltage decreases as the current density exceeds 0.5 A cm^{-2} and rapid voltage drop down at the current density 1.7 A cm^{-2}, due to air and liquid water management issues. In contrast, Designs CRM-3a and CRM-3c, which utilize the corrugated-mesh, do not exhibit significant voltage drops. It is suggested that the corrugated-mesh flow field can provide a uniform gas supply to the CL, even in the presence of liquid water that flooding occurs only for a specific combination of land and channel structures and the GDL, where the liquid water accumulates under the land regions of the cathode [27]. In addition, the GDL-less design efficiently supplies gas to the CL. Specifically, the water on the top surface of the MPL can be easily removed by dynamic gas flow through the corrugated-mesh and therefore, the amount of liquid water in the MPL is kept at a sufficiently low saturation level to allow wider gas diffusion. Furthermore, since the diffusion length in the MPL is smaller than that in the combination of GDL and MPL, the gas diffusion occurs noticeably faster in the GDL-less designs compared to the conventional design with the GDL. Even at such high stoichiometry of the electrode, the electrode can be flooded as reported by H. Yamada et al., based on their experimental and simulation studies [28]. They showed that electrode flooding starts at a current density of 0.4 A cm^{-2}, and that voltage drops significantly around 1.2 A cm^{-2}. Their simulations also showed that the liquid water saturation in the GDL reaches a value greater than 0.8, especially the region under the flow-field land. This suggests that the gas supply is not fast enough, especially in the GDL under the land region to keep up with a current density increase beyond 0.4 A cm^{-2}. The experimental data in the present study shows that Design CRM-3d exhibits a voltage drop at a current density of 0.6 A cm^{-2}, which might be caused by the decreased diffusivity of the SS-MPL, where the reactant gas is unable to diffuse in the in-plane direction of the SS-MPL, diffusing instead in the CL from the through-holes. In addition, the poor performance might be caused by the facile accumulation of water on the hydrophilic surface of the gold-plated layer on the SS-MPL [29]. The present work focuses on electrical resistance. Therefore, a high air flow rate of 1.1 L min^{-1} and an equivalent stoichiometric ratio of 9.0 at a current density of 1.5 A cm^{-2} were used for the cathode, to minimize the channel and electrode flooding effects as well as air management issues that may lead to voltage loss. While a stoichiometric ratio of 9.0 for a conventional parallel flow channel is generally sufficient to avoid substantial effects attributed to channel flooding [30], the electrode flooding effects and air management issues still remain. T. Berning et al. found that a higher stoichiometric flow ratio results in a more uniform distribution of the air in the GDL especially under the land area in conventional fuel cells, by comparing stoichiometric ratios of 1.5 to 4.0 [31]. Further, they estimated the limiting current density at a stoichiometric ratio 4.0 to be 1.5 A cm^{-2}, when the oxygen concentration at the CL reaches zero, without considering any liquid water management issues. Q. Yan measured the static and dynamic behavior under various air stoichiometries of 2.0 to 10.0 for conventional fuel cells [32] and found that even a high stoichiometry of 10.0 shows a performance decrease at high current densities, owing to poor air management through the GDL and the CL on the cathode side. These two studies suggest that while in the conventional fuel cell, the stoichiometry is likely to affect the distribution of the oxygen in the CL, the air management issues cannot be resolved by tailoring the stoichiometry alone because of the flow field structure and diffusion transport in the GDL as well as liquid water management issues. This is likely to be a part of the intrinsic nature of the conventional fuel cells. The results of the performances of Designs CRM-3a and CRM-3c indicate that the corrugated-mesh structure can solve these issues even at a high stoichiometric ratio of 9.0, which is an advantage of the corrugated-mesh structure.

Other than the air management and liquid water management issues, the performances for designs CNV, and CRM-3a–3d are however slightly different because of the different HFR in utilizing the GDL or the various conductivities of the MPLs. The HFR for designs 1, 2, 3, and 4 are 53 mΩ cm^2, 120 mΩ cm^2, 65 mΩ cm^2, and 57 mΩ cm^2, respectively. In the previous study, we found that such HFR values for GDL-less fuel cells followed the order Design CRM-3d < Design CRM-3c < Design CRM-3a, which mimics the MPL conductivity under no-compression condition where SS < SF < CB. However, the conductivity alone does not show a good correlation with HFR in the previous section 5.2.3. This is because the contact resistance of the MPL|CL interface is ignored. Generally, the contact resistance depends on the material, the contact area of the contact point, the surface properties, and the rigidity of the underlying layer [33–35].

The simulation results from our model are shown next, to estimate the internal electrical resistance for each design, by considering the effects of contact pressure and contact resistance. Fig. 3-9(a)–(d) also shows the simulation results of the polarization curves for designs CNV, CRM-3a–3d for three cases, namely, with no-resistance, with only material conductivity, with material conductivity and contact resistance. In Fig. 3-9(a), which shows the simulation results for Design CNV, the modeling performances show big disparities with the experimental performances, especially beyond the current density of 0.4 A cm^{-2}, owing to the slow air supply in the GDL, as discussed previously. For the three modeling cases, the effects of conductivity and contact resistance are negligible at current densities lower than 0.4 A cm^{-2}, which agrees with the results reported by T. Zhou et al. [36]. At intermediate and high current densities of over 0.4 A cm^{-2}, both conductivity and contact resistance effects become more noticeable, since the ohmic loss is proportional to the current density. Although the performance is impacted by the combined effect of gas diffusion and electrical resistance in the GDL [36–38], out model with unity gas and single-phase condition in current study cannot correctly follow the polarization curve. However the aim of this study is for the effect of electrical resistances in the corrugated-mesh fuel cells, and as seen in this section corrugated-mesh fuel cells shows small effect of air and liquid water management issues, therefore applying this model on the conventional fuel cell is just for the reference in the comparison with the corrugated-mesh fuel call cases later in this section.

In Fig. 5-11(b), which shows the results for Design CRM-3a, the conductivity and contact resistance model shows good agreement with the experimental performance, at least for current densities below 2.0 A cm^{-2}. This suggests that the gas is likely to be uniformly supplied to the CL in the corrugated-mesh fuel cell and the performance should be simulated well with our current model. At a current density of over 2.0 A cm^{-2}, the simulated performance slightly diverges from the experimental performance, owing to the gradual increase in the HFR at high current densities. The membrane dries out as a result of the temperature increase from the heat generation at high current densities [22–23], which our model assuming isothermal conditions and constant proton conductivity conditions cannot resolve. The HFR increase reduces the voltage in the high current density range.

Fig. 5-11(c) also shows three simulation results for Design CRM-3c. The modeling results show good agreement with the experimental performance. The divergence between the experimental and simulated results even at high current densities is quite small, in this case. Unlike Design CRM-3a, the HFR increases only slightly beyond the current density of 2.5 A cm^{-2}, because the SF-MPL has good thermal conductivity and there is little increase in the temperature of the membrane as discuss in the section 4.4.3 for HFR in different MPL in corrugated-mesh fuel cell. Comparing Design CRM-3a and Design CRM-3c, the contribution of the conductivity to the total resistance in the case of design 3 is smaller than the case for Design CRM-3c. In this case, the contact resistance is not considered and hence, the electrons can travel through the interface of the MPL and CL. The IR drop through the MPL and the CL in the in-plane direction was determined by the conductivity of the MPL and the CL. The conductivity of the SF-MPL is four orders of magnitude than that of the CB-MPL, as shown in Fig. 5-5, which can be a reason for the difference in the polarization curves. On the other hand, the effect of contact resistance is still significant for both designs CRM-3a and CRM-3c. When the contact resistance is taken into consideration, the electron pathway can be changed and the electrons cannot easily travel through the SF-MPL|CL interface because of the high contact resistance and more electrons conduct through the CL in the in-plane direction. Unfortunately, the conductivity and the thickness of the CL are low and as a result, the electron conduction through the CL can cause a large IR drop. This may be the reason for the significant effect of contact resistance observed for both designs CRM-3a and CRM-3c. While this effect does not originate directly from the contact resistances of the MPL|CL and corrugated-mesh|MPL interfaces, it originates primarily from the pathway change to the in-plane CL.

Fig. 5-11(d) also shows three simulation results for Design CRM-3d. As described above, poor air management through the CL in the in-plane direction causes a voltage drop at the current density of 0.6 A cm^{-2}. Our model is unable to predict this drop owing to the lack of gas transport capability in our current version of the model. Comparing the three resistance cases, the effect of conductivity is high, whereas that of contact resistance is small, showing a result that is opposite to that obtained with Design CRM-3c. The conductivities of SS-MPL and SF-MPL are in a similar range, as shown in Fig. 5-5. Therefore, the conductivity of the MPL is not the reason for the opposite behaviors. Firstly, the SS-MPL can cover the CL only under the solid area and cannot cover the CL under the through-holes area. In the area under the through-holes, the electron conducts through the CL in the in-plane direction, which is thin and low in conductivity and the electron conduction through the in-plane CL can cause a large IR drop. This can explain the large effect of conductivity observed for design Design CRM-3d, and the effect does not originate directly from the conductivity of the SS-MPL. On the other hand, the contact resistance of the SS-MPL|CL interface is low under the solid area of the SS-MPL, as shown in Fig. 5-11(d) and the contact resistance in this area does not make a big difference in the fuel cell performance. This can explain the small contribution of the contact resistance on the cell performance. In addition, either with or without the contact resistance, the electron pathway is not significantly changed and this can also be a reason for the small effect of the contact resistance in Design CRM-3d.

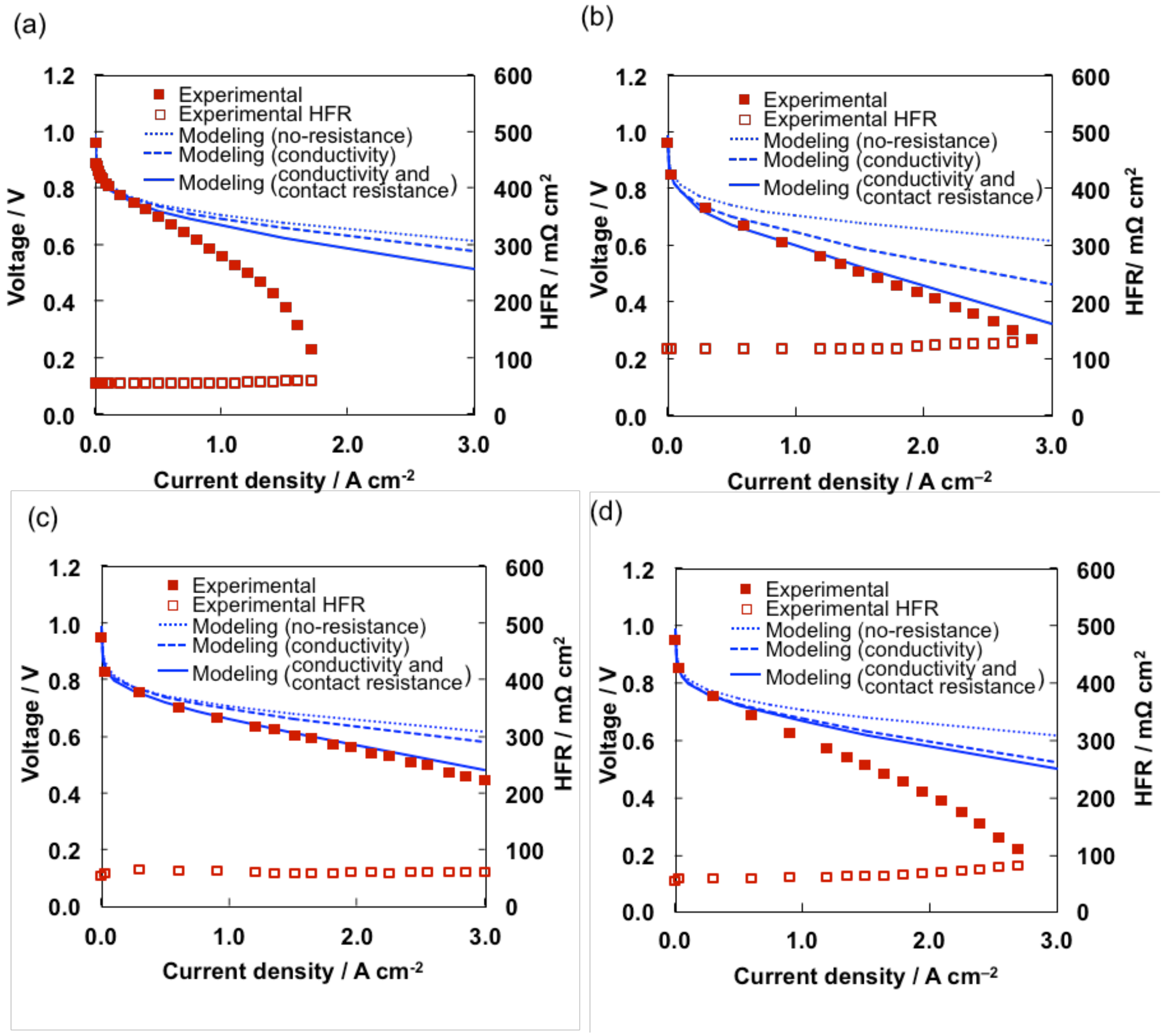

Fig. 5-11. Experimental and simulated polarization curves (a) Design CNV (conventional fuel cell), (b) Design CRM-3a (corrugated-mesh fuel cell with CB-MPL), (c) Design CRM-3c (corrugated-mesh fuel cell with SF-MPL), and (d) Design CRM-3d (corrugated-mesh fuel cell with SS-MPL), obtained under RH_{anode} =100%, $RH_{cathode}$ = 100%, ambient pressure at the outlets, cell temperature = 70 °C, and hydrogen and air supplied in a stoichiometric ratio of 9.0 at 1.5 A cm^{-2}.

5.4.4 Electron conduction pathway and voltage distribution in the fuel cell

Fig.5-12 shows the electron conduction pathway and voltage distribution in the fuel cell at the average current density of 1.0 A cm^{-2} for Design CNV, Design CRM-3, Design CRM-3c, and Design CRM-3d. As seen in Fig. 5-10(a)–(d) in the previous section 5.4.2 for the electrical resistance modeling, the current density distribution can be heavily influenced by the conductivity and the contact resistance of the fuel cells. Certainly, a combination of both contact resistance and conductivity can determine the electron pathway and their total IR drop, but as seen in section 3.3, the contact resistance appears to primarily affect the pathway of the electrons. In Fig. 5-12(a) for Design CNV, the electrons from the BPP at the cathode are distributed in the GDL horizontally to the CB-MPL relatively uniformly and travels to the CL vertically via the interface of the CB-MPL and CL, because the contact resistance of the CB-MPL|CL interface is relatively evenly distributed and low. On the other hand, in Fig. 5-12(b) and (c) on the other hand, the electrons from the corrugated-mesh cannot be distributed horizontally in the MPL because the contact resistance of the MPL|CL interface is high in the area between the corrugation-peaks. Hence, the electrons transfer from the corrugated-mesh to the MPL and the CL vertically in the contact area under the corrugation-peak, where the local contact resistance is low. The electrons then conduct in the CL in the in-plane direction. If all the contact resistances are ignored as seen in section 5.4.2, the electrons can travel through the MPL|CL interface and the electrons can conduct horizontally in both MPL and CL. This also explains the effect of conductivity and contact resistance in Fig. 5-10(b) and (c). In Fig. 5-12 (d), the electrons from the BPP are distributed horizontally in the SS-

MPL, and travel to the CL relatively uniformly via the SS-MPL|CL interface only under the solid part of the SS-MPL. However, in the area below the through-holes of the SS-MPL, the electrons conduct through the CL in the in-plane direction, which results in a non-uniform voltage distribution and also a non-uniform reaction rate according to B-V equation. Although the contact resistance in the area under the solid part of the SS-MPL is low, the gas diffuses through the CL in the in-plane direction, which causes a decrease in the voltage in the experiments with poor air management, as observed in section 5.4.3 for the polarization curves.

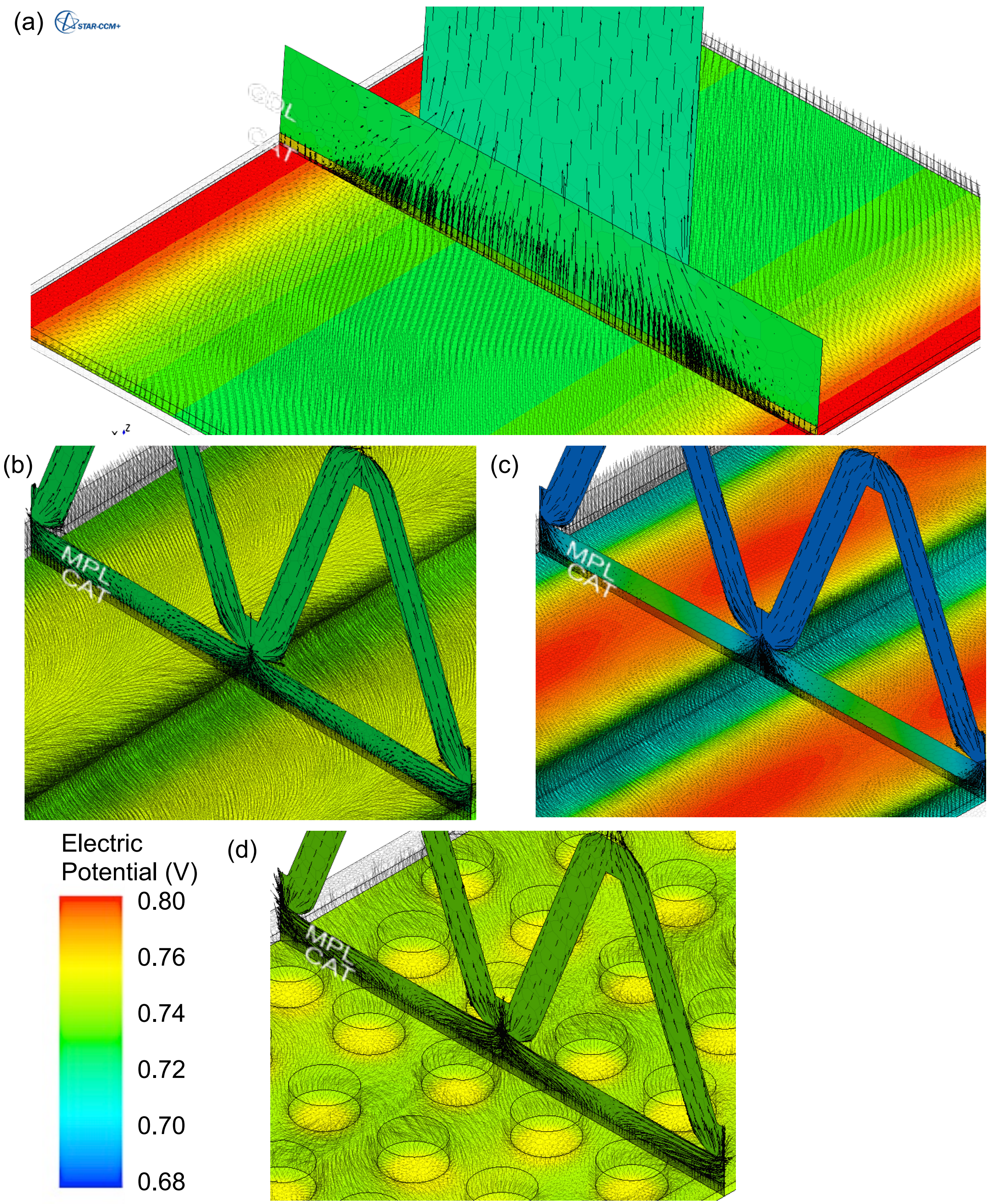

Fig. 5-12. Electron conduction pathway analysis and IR drop distribution for (a) Design CNV (conventional fuel cell), (b) Design CRM-3a (corrugated-mesh fuel cell with CB-MPL), (c) Design CRM-3c (corrugated-mesh fuel cell with SF-MPL), and (d) Design CRM-3d (corrugated-mesh fuel cell with SS-MPL).

5.5 Conclusion for Numerical Simulation Study

In this study we measured and calculated the conductivities and contact resistances are measured for each material in the both of conventional and GDL-less fuel cells as a function of mechanical compression pressures, and with using these data, we developed a coupled mechanical-electric-electrochemical numerical model to investigate the effect of the internal electrical resistance in these fuel cells. Firstly our model can simulate well for GDL-less fuel cell but cannot follow the voltage decrease in the conventional fuel cell. Secondly the effect of the electrical resistance are relatively small in the conventional fuel cell, where the GDL can make a good electrical contact on the interface of GDL|MPL and MPL|CL, and have a good electrical conductivity to distribute the electron sufficiently. In the case of GDL-less fuel cells, however the effect of electrical resistance is big. Especially the electrical contact on the interface of MPL|CL is poor without GDL. Furthermore the electron travel pathway is different between the conventional and GDL-less fuel cell. In the GDL-less fuel cell, the electron can travel mainly through the CL in the in-plane direction because of the poor electrical contact on the MPL|CL. The pathway through the CL and low conductivity of CL is thought as a reason of higher internal electrical resistance in the GDL-less fuel cell. The conductivity and rigidity of the MPL can be the key parameter to control the electrical contact on the interface of MPL|CL to change the electron travel pathway more to the conductive MPL.

Bibliography for Chapter 5

[1] J. Kleemann, F. Finsterwalder, W. Tillmetz, J. Power Sources 190 (2009) 92–102.

[2] A. Pablo, G. Salaberri, M. Vera, R. Zaera, Int. J. Hydrogen Energy 36 (2011) 11856–11870.

[3] J.S. González, A.M. García, M.F.A Franco, V.G. Serrano, Carbon 43 (2005) 741–747.

[4] N. Cunningham, M. Lefèvre, G. Lebrun, J.P. Dodelet, J. Power Sources 143 (2005) 93–102.

[5] H.H. Berger, J. Electrochem. Soc. 119 (1972) 507–514.

[6] W.W. Tyler, A.C. Wilson, Phys. Rev 89 (1953) 870–875.

[7] D.R. Lide (Ed.), Handbook of Chemistry and of Physics (75h Edition) CRC press, Boca Raton (1995).

[8] T. Li, Filtration & Separation 34 (1997) 265–273.

[9] V. Shapovolov, MRS Bulletin 19 (1994) 24–28.

[10] M. Vogler, S. Sheppard, Welding journal 72 (1993) 231–238.

[11] ASTM Standard D695, 2010, "Standard Test Method for Compressive Properties of Rigid Plastics", ASTM International, West Conshohocken, PA, 2003.

[12] I. Taymaz, M. Benli, Energy 35 (2010) 2134–2140.

[13] T. Uchiyama, H. Kumei, T. Yoshida, J. Power Source 238 (2013) 403–412.

[14] A. Kusoglu, A.M. Karlsson, M.H. Santare, S. Cleghorn, W.B. Johnson, J. Power Sources 161 (2006) 987–996.

[15] S.G. Kandlikar, Z. Lu, T.Y. Lin, D. Cooke, M. Daino, J. Power Source 194 (2009) 328–337.

[16] R.C. Hibbeler, Mechanics of Materials, 8th ed., Prentice Hall, New Jersey, 2010.

[17] R.F. Mann, J.C. Amphlett, M.A.I. Hooper, H.M. Jensen, B.A. Peppley, P.R. Roberge, J. Power Sources 86 (2000) 173–180.

[18] S. Um, C.Y. Wang, K.S. Chen, J Electrochem Soc 147 (2000) 4485–4493.

[19] R.F. Mann, J.C. Amphlett, B.A. Peppley, C.P. Thurgood, J. Power Sources 161 (2006) 775–781.

[20] H. Bajpai, M. Khandelwal, E.C. Kumbur, M.M. Mench, J. Power Sources 195 (2010) 4196–4205.

[21] A. Parthasarathy, S. Srinivasan, A.J. Appleby, C.R. Martin, J. Electrochem. Soc. 139 (1992) 2530–2537.

[22] U. Pasaogullari, C.Y. Wang, K.S. Chen, J. Electrochem. Soc. 152 (2005) A1574-A1582.

[23] J.M. Morgan, R. Datta, J. Power Sources 251 (2014) 269-278.

[24] Y. Sone, P. Ekdunge, D. Simonson, J Electrochem Soc 143 (1996) 1254–1259.

[25] F. Barbir, PEM Fuel Cells: Theory and Practice, Academic Press (2005).

[26] T. Zhou, H. Liu, J. Power Sources 161 (2006) 444–453.

[27] Wei Sun, Brant A. Peppley, K. Karan, J. Power Sources 144 (2005) 42–53.

[28] H. Yamada, T. Hatanaka, H. Murata, Y. Morimoto, J. Electrochem. Soc. 153 (2006) A1748–A1754.

[29] F.Y. Zhang, S.G. Advani, A.K. Prasad, J. Power Sources 176 (2008) 293–298.

[30] Z. Lu, C. Rath, G. Zhang, S.G. Kandlikar, Int. J. Hydrogen Energy 36 (2011) 9864–9875.

[31] T. Berning, N. Djilali, J. Power Sources 124 (2003) 440–452.

[32] Q. Yan, H. Toghiani, H. Causey, J. Power Sources 161 (2006) 492–502.

[33] I.N. Sneddon, Int. J. Eng. Sci. 3 (1965) 47-57.

[34] I.V. Zenyuka, E.C. Kumbur, S. Litster, J. Power Sources 241 (2013) 379-387.

[35] T. Swamy, F.E. Hizir, M. Khandelwal, E.C. Kumbur, M.M. Mench, ECS Trans. 25 (2009) 15-27.

[36] T. Zhou, H. Liu, J. Power Sources 161 (2006) 444–453.

[37] H. Meng, C.Y. Wang, J. Electrochem. Soc. 151 (2004) A358–A367.

[38] P.C. Sui, N. Djilali, J. Power Sources 161 (2006) 294–300.

Chapter 6 Conclusion and Future Works

6.1 Conclusion and Original Contribution

We developed and studied a novel GDL-less PEM fuel cell and we achieve the significant improvements on the performance reduction from liquid water flooding, oxygen distribution, and membrane dry-out. However on the contrary the electrical resistance drastically increases in the GDL-less fuel cell. We investigated the cause of the electrical resistance increase, and we found that the electron resistance is a key issue in the GDL-fuel cell and finally one of the GDL-less fuel cell shows a performance of 0.45 V at 3 A cm^{-2} and an HFR of 62 mΩ cm^{-2}. We also show a direction to reduce the electron resistance in the GDL-less fuel cell for the future study. The major accomplishments and contributions achieved in the present study can be summarized as follows;

1. Microcoils and corrugated-mesh are utilized as a flow-field in the GDL-less fuel cell instead of grooved channel and GDL in the conventional fuel cell.
2. Uniform air supply and convection flow in the GDL-less fuel cell can prevent water accumulation and reduce the flooding generally seen at the under-land area in the conventional fuel cell (liquid water flooding issue).
3. The GDL-less fuel cell can also prevent the voltage degrease with the issue of oxygen concentration distribution in the GDL especially under-land area (air-management issue).

4. The GDL-less fuel cell can prevent membrane dry-out because of the higher thermal conductivity of metallic microcoil and corrugated-mesh, which can keep the temperature relatively lower and relative humidity higher than the GDL in conventional GDL (membrane dry-out issue).
5. The internal electrical resistance in the GDL-less fuel cell, however, increases due to fewer contact points at the interface of microcoils|MPL or corrugated-mesh|MPL. Highly conductive silver-flake MPL shows a lower resistance than normal carbon black MPL compared in the GDL-less fuel cell, but still has higher resistance than GDL and carbon black MPL in the conventional fuel cell.
6. The numerical simulation study unveils that the fewer contact points on MPL also makes high contact resistance at the interface of MPL|CL because the MPL cannot distribute the compression pressure uniformly on the CL and the pressure concentrates locally under the corrugation peaks. Therefor the electrons cannot transfer the interface of MPL|CL efficiently and the electrons conduct in the in-plane direction through CL, which has low conductivity. The high resistance in the GDL-fuel cell doesn't derive only from the conductivity difference of each material but also the pathway difference; vertically from CL to GDL though MPL in the conventional fuel cell and horizontally through CL to the corrugated-mesh vertically through MPL.
7. The conductivity and rigidity of the MPL can be the key parameter to keep the compression pressure evenly and to control the electrical contact on the interface of MPL|CL.
8. Rigid stainless steel-MPL with through holes can reduce the internal resistance with

uniform compression on the interface of MPL|CL, but the gas dose not diffuse in this MPL through the solid area and gas must diffuse in the CL, which is thinner than MPL and is thought to have lower diffusivity. The stainless steel-MPL raises liquid water flooding issue and air-management issue mainly in the CL.

6.2 Future work

The gas concentration and the liquid water effect need to be considered for more accurate simulations. The rigidity and the conductivity as well as the geometric dimensions of the MPL can have a great effect on the polarization performance in GDL-less fuel cells. Therefore, an optimization study with these parameters should be done for achieving the best design for the MPL. Further, we will also test the fuel cell performance at practical stoichiometric ratios, in our future research. Finally, the current fuel cell with the corrugated-mesh flow field design exhibits a higher pressure drop because of the small channel dimensions for each gas. Therefore, we will perform an optimization study on the corrugation designs as well as the aspect ratio of the active area to determine the relationship between pressure drop, electrical resistances, and flooding effect.